

University of Windsor

Scholarship at UWindor

Electronic Theses and Dissertations

Theses, Dissertations, and Major Papers

1-1-2019

Design And Modeling Of An Electrostatic Ally Actuated Mems Micromirror For Light Detection And Ranging

Niwit Aryal
University of Windsor

Follow this and additional works at: <https://scholar.uwindsor.ca/etd>

Recommended Citation

Aryal, Niwit, "Design And Modeling Of An Electrostatic Ally Actuated Mems Micromirror For Light Detection And Ranging" (2019). *Electronic Theses and Dissertations*. 8160.
<https://scholar.uwindsor.ca/etd/8160>

This online database contains the full-text of PhD dissertations and Masters' theses of University of Windsor students from 1954 forward. These documents are made available for personal study and research purposes only, in accordance with the Canadian Copyright Act and the Creative Commons license—CC BY-NC-ND (Attribution, Non-Commercial, No Derivative Works). Under this license, works must always be attributed to the copyright holder (original author), cannot be used for any commercial purposes, and may not be altered. Any other use would require the permission of the copyright holder. Students may inquire about withdrawing their dissertation and/or thesis from this database. For additional inquiries, please contact the repository administrator via email (scholarship@uwindsor.ca) or by telephone at 519-253-3000ext. 3208.

DESIGN AND MODELING OF AN ELECTROSTATICALLY ACTUATED MEMS
MICROMIRROR FOR LIGHT DETECTION AND RANGING

by

Niwit Aryal

A Thesis

Submitted to the Faculty of Graduate Studies

through the Department of Electrical and Computer Engineering

in Partial Fulfilment of the Requirements for

the Degree of Master of Applied Science

University of Windsor

Windsor, Ontario, Canada

© 2019 Niwit Aryal

DESIGN AND MODELING OF AN ELECTROSTATICALLY ACTUATED MEMS
MICROMIRROR FOR LIGHT DETECTION AND RANGING

by

Niwit Aryal

APPROVED BY:

R. Seth

Department of Civil and Environmental Engineering

E. Abdel-Raheem

Department of Electrical and Computer Engineering

A. Emadi, Advisor

Department of Electrical and Computer Engineering

November 28, 2019

DECLARATION OF CO-AUTHORSHIP / PREVIOUS PUBLICATION

I. Co-Authorship

I hereby declare that this thesis incorporates material that is the outcome of research and publications which are/were supervised by Dr. Arezoo Emadi.

I am aware of the University of Windsor Senate Policy on Authorship and I certify that I have properly acknowledged the contribution of other researchers to my thesis, and have obtained written permission from each of the co-author(s) to include the above material(s) in my thesis. I certify that, with the above qualification, this thesis, and the research to which it refers, is the product of my own work.

II. Previous Publication

This thesis includes 1 original paper that has been previously published in peer-reviewed journals, as follows:

Thesis Chapter	Publication title/full citation	Publication status*
<i>Chapter [4]</i> <i>Chapter [5]</i>	N. Aryal and A. Emadi, "Novel method to improve stroke of electrostatically actuated MEMS micromirror," <i>ODS 2019: Industrial Optical Devices and Systems</i> , 2019.	Published

I certify that I have obtained written permission from the copyright owner(s) to include the above-published material(s) in my thesis. I certify that the above material describes work completed during my registration as a graduate student at the University of Windsor.

III. General

I declare that, to the best of my knowledge, my thesis does not infringe upon anyone's copyright nor violate any proprietary rights and that any ideas, techniques, quotations, or any other material from the work of other people included in my thesis, published or otherwise, are fully acknowledged in accordance with the standard referencing practices. Furthermore, to the extent that I have included copyrighted material that surpasses the bounds of fair dealing within the meaning of the Canada Copyright Act, I certify that I have obtained written permission from the copyright owner(s) to include such material(s) in my thesis.

I declare that this is a true copy of my thesis, including any final revisions, as approved by my thesis committee and the Graduate Studies office and that this thesis has not been submitted for a higher degree to any other university or institution.

ABSTRACT

A Light Detection and Ranging (LIDAR) system, which is one of the promising technologies for autonomous vehicles, contains many miniature micromachined devices. The micromirror is one of the key components inside the LIDAR system that contributes to the performance of LIDAR. The “stroke” level of the micromirror affects the performance of the micromirror and hence the LIDAR. Therefore, this research focuses on a new approach to increase the level of stroke of the micromirror in an effort to enhance the device properties. In this thesis, four different design configurations of micromirrors are proposed and developed. The proposed micromirrors are based on dynamically-moving capacitor concepts that are actuated using electrostatic actuation. Unlike traditional micromirrors, the developed micromirrors employ three bottom electrodes, which enforces an upward deflection and, therefore, reduces the pull-in instability effect and improves the stroke of the micromirror. Critical design parameters of the micromirror that affect the stroke are studied to develop the four proposed designs. The PolyMUMPs fabrication technique is chosen to fabricate all four proposed micromirror designs. When the micromirror is fabricated using the PolyMUMPs fabrication technique, without any modification in the fabrication steps, the maximum achievable air cavity between the parallel plates is $2.0\mu\text{m}$. However, in this thesis, in an unconventional way, the air cavity is increased from $2.0\mu\text{m}$ to $2.75\mu\text{m}$. This is achieved by combining two oxide layers in the fabrication process. In this new design, a high stroke level of $5.07\mu\text{m}$ is achieved that, in return, will further enhance the performance of the LIDAR. COMSOL Multiphysics software and the MEMS module are used to investigate and analyze the performance of the proposed micromirrors and compare them with conventional MEMS micromirrors.

DEDICATION

To the almighty God, who is the ultimate source of positive energy!

ACKNOWLEDGMENT

I would like to take this opportunity to thank everyone who has helped me along the way.

I would like to thank my family. They are my constant source of inspiration who always believed in me and always backed my decisions. Without them, this would not have been possible.

I would also like to thank, with my sincere gratitude, my Supervisor, Dr. Arezoo Emadi. She was always there to help me whenever needed. She guided me technically and always instilled positivity in me. It has truly been a pleasure working with her and the team. Dr. Emadi not only focuses on the technical aspect but also creates an amazing working environment with the team which in turn improves team spirit, leadership, and effective communication skills. She is the best boss that I ever had.

I would also like to thank my committee members: Dr. Seth and Dr. Abdel-Raheem. I would like to thank them for their time and support. Their encouragement inspired me to work harder.

Last but not least, I would like to thank Matthew Santos and all my eMinds team members who helped me with their valuable input during my research.

TABLE OF CONTENTS

DECLARATION OF CO-AUTHORSHIP / PREVIOUS PUBLICATION-----	iii
ABSTRACT -----	v
DEDICATION-----	vi
ACKNOWLEDGMENT -----	vii
LIST OF TABLES -----	x
LIST OF FIGURES -----	xi
1 CHAPTER I: BACKGROUND AND THESIS OVERVIEW -----	1
1.1 Motivation -----	1
1.2 Background-----	3
1.3 Thesis Objectives and Contribution-----	4
1.4 Thesis Outline-----	6
2 CHAPTER II: MEMS MICROMIRROR AND ACTUATION MECHANISM -----	8
2.1 Introduction-----	8
2.2 MEMS Micromirror-----	8
2.3 Actuation Mechanisms of Micromirror -----	10
2.3.1 Electrostatic Actuation -----	10
2.3.1.1 Parallel-Plate Actuator -----	12
2.3.1.2 Comb-Drive Actuator -----	17
2.3.2 Electromagnetic Actuation -----	18
2.3.3 Piezoelectric Actuation -----	19
2.4 Summary and Conclusion -----	20
3 CHAPTER III: INVESTIGATION AND ANALYSIS OF DESIGN PARAMETERS	22
3.1 Introduction-----	22
3.2 Conventional Electrostatically-Actuated MEMS Micromirror -----	23
3.3 MEMS Micromirror with an L-shaped Arm and Three Fixed Bottom Electrodes -----	24
3.3.1 Effect of Fringing Field on the Stroke -----	26
3.4 COMSOL Simulation Results of the Micromirror-----	28

3.4.1	Finite Element Analysis -----	28
3.4.2	Critical Parameters' Influence on the Stroke -----	30
3.4.2.1	Effect of Input Voltage-----	33
3.4.2.2	Effect of Width of the Arm-----	34
3.4.2.3	Effect of the Separation Gap Between Three Fixed Bottom Electrodes -----	35
3.5	Summary and Conclusion -----	36
4	CHAPTER IV: PROPOSED MICROMIRROR DESIGN SIMULATION RESULTS	
	39	
4.1	Introduction-----	39
4.2	Proposed Micromirror Designs to Enhance Stroke Level -----	40
4.3	Simulation Results and Design Evaluations -----	46
4.3.1	Tilting of Micromirror Surface -----	46
4.3.2	Effect of Air Domain on the Level of Stroke-----	47
4.3.3	Micromirror Design 1 Evaluation -----	49
4.3.4	Micromirror Design 2 Evaluation -----	51
4.3.5	Micromirror Design 3 Evaluation -----	53
4.3.6	Micromirror Design 4 Evaluation -----	55
4.4	Design Comparison and Conclusion-----	58
5	CHAPTER V: FABRICATION OF PROPOSED MICROMIRROR -----	65
5.1	Introduction-----	65
5.2	PolyMUMPs Fabrication Technique -----	65
5.3	Fabrication Steps of the Proposed Micromirrors-----	67
5.4	Summary and Conclusion -----	76
6	CHAPTER VI: CONCLUSION AND FUTURE WORK -----	79
6.1	Summary and Conclusion -----	79
6.2	Future Work -----	82
	REFERENCES -----	84
	APPENDIX A -----	92
	VITA AUCTORIS -----	93

LIST OF TABLES

Table I: Comparison of electrostatic, electromagnetic and piezoelectric actuators. -----21

Table II: Physical properties of the micromirror in Design 1 with the air cavity of 2 μ m. 42

Table III: Physical properties of the micromirror in Design 2 with the air cavity of 2 μ m.
-----42

Table IV: Physical properties of the micromirror in Design 3 with the air cavity of 2.75 μ m.
-----45

Table V: Physical properties of the micromirror in Design 4 with the air cavity of 2.75 μ m.
-----46

Table VI: Level of the stroke and micromirror downward deflection in Design 1 versus
input DC bias voltage. -----50

Table VII: Level of the stroke in Design 2 when the input DC bias voltage is applied to one
subdivided electrode as well as when it is applied to two subdivided electrodes. -----52

Table VIII: Level of the downward deflection in Design 2 when the input DC bias voltage
is applied to one subdivided electrode as well as when it is applied to two subdivide
electrodes. -----53

Table IX: Levels of stroke and downward deflection in Design 3 versus the input DC bias
voltage. -----55

Table X: Level of stroke in Design 4 when the input DC bias voltage is applied to one
subdivided electrode as well as when it is applied to two subdivided electrodes. -----56

Table XI: Level of the downward deflection in Design 4 when the input DC bias voltage
is applied to one subdivided electrode as well as when it is applied to two subdivide
electrodes. -----57

Table XII: Table illustrating maximum downward and upward deflection for all four
proposed micromirror designs and their biasing conditions. -----63

Table XIII: Microfabrication process sequence and layers' thicknesses in the PolyMUMPs
fabrication technique. -----66

Table XIV: Employed mask layers and their purposes in the PolyMUMPs fabrication
technique. -----68

LIST OF FIGURES

Figure 2.1: A simple scanning micromirror with an optical scanning angle. 9

Figure 2.2: Schematic view of electrostatic actuators: (a) parallel-plate actuator, (b) linear comb-drive actuator, (c) vertical comb-drive actuator, and (d) rotary comb-drive actuator. 11

Figure 2.3: Schematic view of a parallel-plate electrostatic actuator. 12

Figure 2.4: Schematic view of (a) simplified cross-sectional image of micromirror actuated by electrostatic force. (b) micromirror surface tilts as a response of the electrostatic force. 13

Figure 2.5: Schematic view of (a) a three-bottom-electrode parallel-plate design showing the distribution of the generated electrostatic force, and (b) the resulting electrostatic field on the upper plate. 15

Figure 2.6: COMSOL simulation results conducted in this thesis investigating a parallel-plate design with three fixed bottom electrodes, where the resulting electrostatic force pushes the upper plate upward for an input bias voltage of 50V. The arm's width and length are 8 μ m, 400 μ m, respectively. The bottom electrodes' length, width, and distance from each other are 400 μ m, 10 μ m, and 5 μ m, respectively. 15

Figure 2.7: Schematic view of an electromagnetic actuator. 18

Figure 3.1: Top view of two conventional electrostatically-actuated MEMS micromirrors. 23

Figure 3.2: Top view of the micromirror showing the L-shaped arm and three fixed bottom electrodes generated using COMSOL simulation software. 24

Figure 3.3: Schematic view of the micromirror Design 3 in MEMSPro using the PolyMUMPs fabrication technique. Details about the different proposed micromirror designs are explained in Chapter 4. 25

Figure 3.4: Cross-sectional view of the proposed micromirror Design 3 in MEMSPro using the PolyMUMPs fabrication layer sequence. Fabrication steps are described in detail in Chapter 5. 26

Figure 3.5: COMSOL electrostatic simulation results showing the fringing fields at the edge of the general circular parallel plate capacitor with a radius of 10cm and a thickness of 0.5cm. 27

Figure 3.6: Fringing field effects for the three bottom electrode configuration employed in this work. -----28

Figure 3.7: The 400 μm by 400 μm micromirrors in Designs 1 to 4 with “finer” mesh; the micromirror is divided into 2,136,622 smaller elements. -----29

Figure 3.8: COMSOL simulation results showing the stroke level versus mesh type for the parallel-plate micromirror. -----29

Figure 3.9: COMSOL simulation results showing simulation time versus mesh type for the parallel-plate micromirror. -----30

Figure 3.10: The schematic view of an arm with one fixed bottom electrode showing the downward movement of the arm. The arm’s width, length, and voltage are 8 μm , 400 μm , and 50V, respectively, whereas the width and length of the bottom electrode are 10 μm and 400 μm , respectively.-----31

Figure 3.11: The schematic view of an arm with three fixed bottom electrodes indicating the upward movement of the arm. The arm’s width, length, and applied bias voltage are 8 μm , 400 μm , and 50V, respectively, whereas the width, length, and separation gap between the bottom electrodes are 10 μm , 400 μm , and 5 μm , respectively.-----32

Figure 3.12: The schematic view of an L-shaped arm with three fixed bottom electrodes showing the upward movement of the arm. The arm’s width, length, and applied bias voltage are 8 μm , 400 μm , and 50V, respectively, whereas the width, length, and separation gap between the bottom electrodes are 10 μm , 400 μm , and 5 μm , respectively. -----32

Figure 3.13 The schematic view of the micromirror with an L-shaped arm and three fixed bottom electrodes showing the upward movement of the micromirror and its arm. The arm’s width, length, and applied bias voltage are 8 μm , 400 μm , and 50V, respectively, whereas the width, length, and separation gap between the bottom electrodes are 10 μm , 400 μm , and 5 μm , respectively. When one end of the arm goes up, the other end goes down, which tilts the micromirror surface. -----33

Figure 3.14: COMSOL simulation results illustrating deflection versus voltage for an arm, an L-shaped arm, and a micromirror with an L-shaped arm. The length and width of the L-shaped arm are 400 μm and 8 μm , respectively. The width of the bottom electrodes is 10 μm and they are separated by an equal distance of 8 μm . -----34

Figure 3.15: COMSOL simulation results illustrating deflection versus width of the arm for an arm, an L-shaped arm, and a micromirror with an L-shaped arm. The length and width of the L-shaped arm are 400 μm and 8 μm , respectively. The width of the bottom electrodes is 10 μm , which are separated by an equal distance of 8 μm . -----35

Figure 3.16: COMSOL simulation results illustrating deflection versus separation gap between fixed bottom electrodes for an arm, an L-shaped arm, and a micromirror with an L-shaped arm. The length and width of the L-shaped arm are 400 μm and 8 μm , respectively.

The width of the bottom electrodes is $10\mu\text{m}$, which are separated by an equal distance of $8\mu\text{m}$.-----36

Figure 4.1: (a) Top view of Design 1 in MEMSPro using the PolyMUMPs fabrication process, (b) a cross-sectional view of Design 1 showing an air cavity of $2.0\mu\text{m}$ in MEMSPro. 41

Figure 4.2: (a) Top view of Design 2 with subdivided bottom electrodes designed and fabricated using the PolyMUMPs fabrication process. (b) Scanning Electron Microscope (SEM) image of Design 2 that is captured using a HITACHI TM3030 plus tabletop microscope. 43

Figure 4.3: (a) Top view and (b) cross-sectional view of Design 3 in MEMSPro, fabricated using the PolyMUMPs fabrication process..... 44

Figure 4.4: Top view of Design 4 micromirror in MEMSPro, developed using the PolyMUMPs fabrication process. 45

Figure 4.5: COMSOL simulation results of Design 1 showing the tilting of the micromirror surface for an applied bias voltage where one end of the micromirror surface moves upward and the other end deflects downward with an unequal amplitude of deflection..... 47

Figure 4.6: COMSOL simulation results presenting the effect of enlarging the outer air domain on the mirror's stroke..... 49

Figure 4.7: Micromirror geometry in COMSOL simulation software with an outer air domain that extends $50\mu\text{m}$ from all of the edges of the micromirror. This air domain is large enough to contain all the electric flux lines. 49

Figure 4.8: COMSOL simulation results presenting the effect of the input voltage on the stroke of the micromirror in Design 1..... 50

Figure 4.9: COMSOL simulation results presenting the effect of the input voltage on the stroke of the micromirror in Design 2 when an input DC bias voltage is applied to one of the subdivided electrodes as well as when it is applied to two of the subdivided electrodes. 52

Figure 4.10: COMSOL simulation results presenting the effect of the input voltage on the stroke of the micromirror in Design 3..... 54

Figure 4.11: COMSOL simulation results presenting the effect of the input voltage on the stroke of the micromirror in Design 4 when an input DC bias voltage is applied to one of the subdivided electrodes as well as when it is applied to two of the subdivided electrodes. 56

Figure 4.12: COMSOL simulation results comparing the effect of the input voltage on the stroke of all four proposed micromirror designs..... 59

Figure 4.13: Top view of the surface of Design 1 with a diagonal cut line from point1(0,455) to point2(455,0). The amplitude of the deflection level along this cut-line shows the uniformity of the micromirror surface, which is illustrated in Figures 4.15 and 4.16..... 61

Figure 4.14: Schematic view of COMSOL simulation result, scaled up 25 times, showing the tilting of the micromirror surface of Design 1. When one arm is actuated at 100V, one end of the micromirror surface moves upward and the other end deflects downward, however, the amplitude of level of deflection is not equal. 61

Figure 4.15: COMSOL simulation results showing the deflection of the micromirror surface along the diagonal cut-line for (a) Design 1 at 100V (b) Design 2 at 120V (c) Design 3 at 150V (d) Design 4 at 150V. These results show that the micromirror surface is tilting and there is no bending. 62

Figure 4.16: COMSOL simulation results showing the deflection of the micromirror surface along the diagonal cut-line for all four proposed micromirror designs. This illustrates that the micromirror surface is tilting and there is no bending. The negative deflection is for downward deflection whereas the positive deflection represents upward movement..... 64

Figure 5.1: Deposition of a 0.6 μm -thick silicon nitride layer for electrical isolation using a low-pressure chemical vapor deposition (LPCVD) technique..... 67

Figure 5.2: Deposition of the first 0.5 μm -thick polysilicon layer (P0) directly on the nitride layer using a low-pressure chemical vapor deposition (LPCVD) technique..... 68

Figure 5.3: Etching away the P0 layer after patterning the photoresist in the plasma etch system. 69

Figure 5.4: (a) top view of the P0 layer of Design 1 and Design 3, (b) top view of the P0 layer of Design 2 and Design 4 in MEMSPro fabricated using the PolyMUMPs fabrication process. Designs 1 and 3 include one central bottom electrode and Designs 2 and 4 each contains four subdivided bottom electrodes. 69

Figure 5.5: Deposition of the first 2.0 μm thick oxide layer (O1) using low-pressure chemical vapor deposition (LPCVD) technique. O1 is the first sacrificial layer. 69

Figure 5.6: Deposition of the 2.0 μm thick second polysilicon layer (P1) using a low-pressure chemical vapor deposition (LPCVD) technique. P1 is then annealed at 1500 $^{\circ}\text{C}$ for an hour in an Argon chamber..... 70

Figure 5.7: Etching away the P1 layer after patterning the photoresist in the plasma etch system for (a) Design 1 and Design 2, and (b) Design 3 and Design 4. 71

Figure 5.8: (a) top view of the micromirror showing P1 as the top actuating layer in Design 1 and Design 3, and (b) top view of the micromirror showing the P1 layer is deposited only at the anchor and is etched away from all the other areas in Design 2 and Design 4 in MEMSPro using a standard PolyMUMPs fabrication layer sequence. 71

Figure 5.9: Deposition of the 0.75 μ m-thick second oxide layer (O2) for (a) Design 1 and Design 2, and (b) Design 3 and Design 4. The wafer is then annealed at 1050 $^{\circ}$ C for an hour. 72

Figure 5.10: Etching away the O2 layer after patterning the photoresist in the plasma etch system for (a) Design 1 and Design 2, and (b) Design 3 and Design 4. 72

Figure 5.11: Deposition of 1.5 μ m-thick third polysilicon layer (P2) for (a) Design 1 and Design 2, and (b) Design 3 and Design 4. The wafer is then annealed for an hour at 1050 $^{\circ}$ C. 73

Figure 5.12: Etching away the P2 layer after patterning the POLY2 in the plasma etch system for (a) Design 1 and Design 2, and (b) Design 3 and Design 4. 73

Figure 5.13: Deposition of the 0.5 μ m-thick metal layer for (a) Design 1 and Design 2, and (b) Design 3 and Design 4. First, the wafer is coated with METAL on the lithographically patterned wafer. The extra gold layer is then removed by the lift-off process in an Acetone bath. 73

Figure 5.14: The chip dipped in a 49% HF solution, which releases the structure, followed by CO2 drying to avoid stiction. Image illustrating released layer and structure of polysilicon layer for (a) Design 1 and Design 2, and (b) Design 3 and Design 4. 74

Figure 5.15: Design 1 micromirror designed in MEMSPro and developed using a standard PolyMUMPs fabrication sequence. In Design 1, the L-shaped arm is made of the P1 layer and the air cavity is 2.0 μ m. 74

Figure 5.16: Design 2 micromirror designed in MEMSPro and fabricated using a standard PolyMUMPs fabrication sequence. In Design 2, the bottom electrode beneath the micromirror surface is subdivided into four individual electrodes. The L-shaped arm is made of the P1 layer and the air cavity is 2.0 μ m. 75

Figure 5.17: Design 3 micromirror designed in MEMSPro and fabricated using a standard PolyMUMPs fabrication sequence. In Design 3, the L-shaped arm is made of the P2 layer and the air cavity is 2.75 μ m. 75

Figure 5.18: Design 4 micromirror designed in MEMSPro and developed using a standard PolyMUMPs fabrication sequence. In Design 4, the bottom electrode beneath the

micromirror surface is subdivided into four individual electrodes. The L-shaped arm is made of the P1 layer and the air cavity is $2.75\mu\text{m}$ 76

Figure 5.19: Scanning Electron Microscope (SEM) image of a Design 1 micromirror that is captured using a HITACHI TM3030 plus tabletop microscope. 77

Figure 5.20: Optical microscope image of a Design 3 micromirror that is captured using the SEMIPROBE SZMCTV1/2 microscope. 77

1 CHAPTER I: BACKGROUND AND THESIS OVERVIEW

1.1 Motivation

According to the World Health Organization's infographic report on road safety, nearly 1.25 million people die annually in road crashes across the globe [1]. That is an average of 3,287 deaths per day. Road crashes rank as the 9th leading cause of deaths, which accounts for 2.2% of all deaths globally. In 2017, more than 150,000 people were injured and 1,800 died in car crashes in Canada [2]. However, road crashes can potentially be preventable. Therefore, there have been several initiatives from government and automobile manufacturing companies to make roads and vehicles safer [3], [4].

One of the main reasons for road crashes is distracted driving and, in order to mitigate the driver's fault, automobile manufacturing companies are investing autonomous vehicles. It is suggested that autonomous vehicles are consistently safer [5]. Since one of the main reasons for road crashes is distracted or fatigued drivers, autonomous vehicles can potentially solve this problem by eliminating drivers from the safety equation. The biggest advantage of autonomous vehicles is the elimination of human error, as it is programmed to follow traffic rules without distraction [6]. Therefore, this has created a necessity and demand for autonomous vehicles. In order to meet these needs, automotive companies such as Nissan, BMW, and Google (partnering with Waymo) have already started working on fully autonomous vehicles [7], [4].

Significant progress has been made towards the research and development of technologies for autonomous driving that require various sensors in order to read the road signs and to react to the dynamic road situations. Technological solutions such as cameras, infrared cameras, Radio Detection and Ranging (RADAR), and Light Detection and

Ranging (LIDAR) are being considered to address these needs of autonomous driving. In recent years, LIDAR has been shown to be a promising candidate due to its potential solution for creating a 3D map of the target and vehicle surroundings. LIDAR, within its field of view, measures the distance between the source and the target by illuminating the target with pulsed laser light. For LIDAR, the field of view is the angle through which it can collect the reflected light source. On average, the field of view of the human eye is 114 degrees (horizontal) whereas the field of view of LIDAR is around 20-25 degrees. Therefore, 3 to 5 LIDAR sensors are needed in order to scan the view in front of a moving vehicle. This increases the overall cost of the autonomous vehicle.

A LIDAR system contains several miniature components including a micromirror, which is one of the important components contributing to the performance and field of view of the overall system [8], [9], [10]. These micromirrors can be developed using Micro Electro Mechanical System (MEMS) technology. The MEMS micromirror is a miniature electromechanical device that is used to control the direction and intensity of the reflected light to detect and identify the objects in front of the LIDAR system. This micromirror, when actuated, undergoes deflection to collect and reflect the light at various angles, carrying the object's information, such as the distance to the mirror. This deflection is also called the stroke of the micromirror. The stroke of the micromirror is the level of deflection that is defined by the distance that the micromirror surface can move within its air cavity. The air cavity for a micromirror is the space that allows the micromirror surface to move. In LIDAR, the stroke of the micromirror determines the system field of view [11], [12]. Consequently, a higher stroke of the micromirror results in a higher field of view. Therefore, through enhancing the stroke of a micromirror, the field of view of LIDAR can

be significantly improved. This, in turn, advances the system performance and safety and also reduces the number of required LIDAR systems to be used in an autonomous vehicle, which reduces the overall cost. In this thesis, four new MEMS micromirror designs are proposed, investigated, evaluated, and compared. In addition, various critical design parameters of the designed and proposed micromirrors are identified and studied in an effort to maximize the stroke of the designed micromirrors.

1.2 Background

LIDAR illuminates the target with pulsed laser light and the collected reflected light is used to determine the distance to the target [13]. Differences in return times and wavelengths can be used to make a 3D representation of the target. Autonomous vehicles use LIDAR for obstacle detection and to navigate safely through the environment. LIDAR offers several advantages including short- to long-range measurement, good angular resolution, and 3D mapping [13-16]. However, its performance falls short due to its narrow field of view, poor performance in harsh environmental conditions, and difficulty identifying targets with low reflectivity [17]. In order to overcome the environmental challenges and low reflectivity identification concerns, several techniques, such as mounting a band-pass filter on the system for harsh environmental conditions and using photomultipliers for low reflectivity targets, can be implemented [18].

Conventional LIDAR systems are bulky. They use a polygon micromirror that requires a rotating mechanism. These are generally mounted on top of the vehicle. These systems are currently being tested by Google for its autonomous vehicles. However, these LIDAR systems are very expensive. On the other hand, solid-state LIDAR systems are small and use a MEMS micromirror instead of a polygon micromirror and there is no need

for mechanical movement of the whole system [19]. These solid-state LIDAR systems are small and relatively inexpensive and can be easily mounted on a car. Key components of solid-state LIDAR systems are a laser diode, MEMS micromirror, diffuser lens, and receiver lens. The laser diode emits the laser light that strikes the MEMS micromirror. The MEMS micromirror reflects the laser light, which hits the diffuser lens. The diffuser lens then splits the single laser light ray into multiple laser light rays and is projected on the target ahead. The micromirror effects the performance of the LIDAR system. Stroke of the micromirror, which is the distance the micromirror surface deflects when it is actuated, affects the field of view of LIDAR. Increasing the level of stroke of a micromirror increases the field of view of LIDAR, consequently, enhancing the performance of the LIDAR.

1.3 Thesis Objectives and Contribution

In this thesis, a new MEMS micromirror configuration is designed, proposed and investigated to enhance the device performance and the level of stroke. Stroke, which is the distance that the micromirror surface moves, is a critical characteristic of a LIDAR system. The stroke of a micromirror determines the field of view of LIDAR. As a result, a higher stroke level of a micromirror increases the field of view of LIDAR, which will reduce the number of LIDAR being used in an autonomous vehicle. The stroke of the micromirror can be improved in several ways, which are discussed in detail in upcoming chapters.

In this thesis, micromirrors and their various actuation mechanisms are investigated. Proposed micromirror designs are based on a parallel plate capacitive design and are actuated using electrostatic actuation. Electrostatic actuation is chosen because of its advantages such as low power consumption, fast response time, high optical scan angle,

scan mode both in 1D and/or 2D, simple design structure, and ease of fabrication [20]. Since the proposed micromirror is electrostatically actuated, it undergoes pull-in instability. Pull-in instability is the phenomenon that limits the stroke of the micromirror to $1/3^{\text{rd}}$ of the air cavity. Pull-in instability occurs because the electrostatic force pulling the micromirror down becomes higher than the micromirror plate's restoring force. However, unlike a traditional MEMS micromirror, the proposed micromirror achieves large out-of-plane stroke by reducing pull-in instability. In order to reduce the effect of pull-in instability, three bottom electrodes are employed beneath the arm of the micromirror. Due to this configuration of bottom electrodes, the net electrostatic force is pointed upward, consequently, pushing the micromirror surface upward instead of the traditional downward deflection.

The proposed micromirrors have a central reflective surface of $400\mu\text{m}$ by $400\mu\text{m}$, an L-shaped arm, and three fixed bottom electrodes on each side of the micromirror. L-shaped arms are anchored on all sides of the micromirror to hold the micromirror. An L-shaped arm is chosen because it provides more flexibility for the arm to move upward. Critical design parameters such as the input voltage, width of the L-shaped arm, and the distance between the three fixed bottom electrodes are investigated and analyzed in order to maximize the performance of the proposed micromirror. COMSOL Multiphysics, which is Finite Element Analysis (FEA) software is used to investigate and analyze the effect of critical design parameters on the stroke of the micromirror. In this thesis, four different designs of micromirrors are proposed. These four designs are named Design 1, Design 2, Design 3, and Design 4. All of the micromirror designs are based on a parallel plate capacitive design with four arms and three fixed bottom electrodes beneath each arm. The

width of the L-shaped arm and the separation gap is kept constant for all four designs. The width of the L-shaped arm is $8\mu\text{m}$ and the separation gap between the fixed bottom electrodes is chosen to be $8\mu\text{m}$, based on the COMSOL simulation results. Moreover, in order to further enhance the stroke level of the micromirror, the air cavity, which is the gap between the micromirror surface and bottom electrode, as well as the bottom electrode configuration, have been optimized within the fabrication limitations. The micromirror is fabricated using the PolyMUMPs [21] fabrication technique. Without any modification to the standard PolyMUMPs fabrication technique, the maximum achievable air cavity is $2.0\mu\text{m}$. However, the proposed design utilizes the combination of two available sacrificial layers in the PolyMUMPs technique to achieve an air cavity of $2.75\mu\text{m}$. This increase in the air cavity height allows more space for the micromirror surface to deflect, consequently, increasing the stroke of the micromirror. However, the increased air cavity increases the operating voltage. For Design 1 and Design 2, the air cavity is $2.0\mu\text{m}$; whereas, for Design 3 and Design 4, the air cavity is $2.75\mu\text{m}$. For Design 1 and Design 2, the stroke level at 100V is $2.25\mu\text{m}$ and $1.42\mu\text{m}$, respectively. On the other hand, for Design 3 and Design 4, the stroke level at 150V is $4.37\mu\text{m}$ and $2.88\mu\text{m}$, respectively. Therefore, out of four different proposed designs, Design 3 has the highest stroke level, which is $4.37\mu\text{m}$ at 150V .

1.4 Thesis Outline

This thesis proposes and outlines the implementation of different MEMS micromirror designs to increase the stroke of the micromirror. Chapter 2 outlines the MEMS micromirror mechanism of operation and its actuation mechanisms. Actuation mechanisms such as electrostatic, electromagnetic, and piezoelectric are discussed in detail. Furthermore, different actuators such as parallel plates and comb-drive actuators are

investigated. A comparison between different actuation mechanisms and their principle of operation is also presented.

Chapter 3 presents conventional micromirrors as well as the proposed micromirror with the L-shaped arm and three fixed bottom electrodes. The effects of critical design parameters such as the input voltage, width of the L-shaped arm, and the separation gap between the electrodes are investigated and analyzed. COMSOL Multiphysics simulation software is used to analyze the design parameters and evaluate the designs.

In Chapter 4, four different micromirror designs that utilize the generated electrostatic field between the plates, as well as the fringing field, are proposed. In these designs, the fringing field generated in an electrostatically-actuated microstructure affects the device performance. Therefore, it is important to consider the fringing field effect on the micromirror, which is presented in Chapter 4. Then, COMSOL simulation results of the proposed micromirror designs are presented and compared.

Chapter 5 outlines the PolyMUMPs fabrication technique that is chosen to fabricate all four of the proposed micromirror designs. The PolyMUMPs fabrication technique is chosen because it is a cost-effective fabrication technique to fabricate the proposed and designed micromirrors for proofs-of-concept.

Finally, Chapter 6 summarizes the work done in this thesis along with the simulation results obtained for the proposed micromirror designs and their comparisons. Then, possible future work that would increase the stroke of the micromirror and enhance the performance of the device is presented.

2 CHAPTER II: MEMS MICROMIRROR AND ACTUATION MECHANISM

2.1 Introduction

Micro Electro Mechanical System (MEMS) refers to a technology that uses advanced micro- and nano-fabrication technology in order to fabricate miniaturized electromechanical devices and systems [22], [24]. MEMS devices incorporate the functionalities of both electrical and mechanical engineering principles [23]. MEMS technology is continuously evolving with advances in micro- and nano-fabrication techniques[22], [24]. Fabrication of these miniaturized electronic devices costs less than the fabrication of macro devices due to the possibility of the mass production that is made possible by MEMS fabrication technology [24]. One of the many electromechanical devices that have advanced along with MEMS technology is a micromirror.

A micromirror is a miniature electromechanical device that consists of a single mirror or an array of mirrors to control the direction and intensity of the reflected light from an incident light source. The first micromirror was developed in 1987 by Texas Instruments [25], and since then, it has advanced due to the market demand for portable displays as well as telecommunications. In today's era, health care and the automotive industry are further driving the development of these miniaturized micromirrors.

2.2 MEMS Micromirror

A MEMS micromirror is defined as a miniature electromechanical device that consists of a single mirror or an array of mirrors [26-28] to control the direction and intensity of reflected light from an incident light source for various optical systems such as video

projection, lighting equipment, and object detection and ranging [29]. Generally, a micromirror is composed of actuator plates and a reflective micromirror surface. Actuator plates generate a force on the micromirror surface that deflects it and creates an optical scanning angle. The optical scanning angle of a MEMS micromirror is the angle that incident light will create after getting reflected from the micromirror surface, relative to the neutral position of the micromirror. A schematic diagram of a micromirror, with its associated optical scanning angle, is illustrated in Figure 2.1.

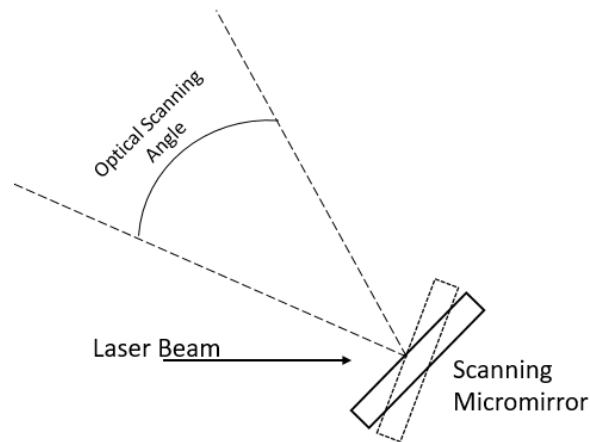


Figure 2.1: A simple scanning micromirror with an optical scanning angle.

The deflection of the micromirror surface is also interchangeably called “stroke” of the micromirror. The stroke for a micromirror is the distance that the micromirror surface can deflect within its air cavity. The air cavity of a micromirror is the space between its two parallel plates. Stroke determines the optical scanning angle of the micromirror. The stroke of a micromirror is a mechanical characteristic whereas the optical scanning angle is an optical characteristic of the micromirror. The micromirror can be actuated using various actuation mechanisms, and the design and the size of the micromirror can be different for different actuation mechanisms. This is discussed in detail in Section 2.3.

2.3 Actuation Mechanisms of Micromirror

An actuator in an electromechanical system is responsible for controlling the movement of that system [30]. Similarly, an actuator system generates movement of the micromirror surface in MEMS micromirrors. The micromirror can be actuated using various actuation mechanisms such as electrostatic, electromagnetic and piezoelectric actuation. Electrostatic and electromagnetic actuation mechanisms are the two most commonly used methods in MEMS devices. However, electromagnetic actuation is traditionally used in macro machines and devices but is rarely used in microdevices, due to the difficulty in miniaturization and microscale fabrication [30], [31]. In this chapter, common configurations of electrostatic actuation mechanisms as well as electromagnetic and piezoelectric actuators are investigated in detail.

2.3.1 Electrostatic Actuation

Electrostatic actuators generate mechanical motion when a voltage is applied to the two parallel-plate actuators. The fundamental principle behind the deflection of two parallel plates is that when an input voltage is applied to the plates, it generates an electrostatic force that attracts the plates toward each other [32], [33]. However, electrostatic actuators have a non-linear force-to-voltage relationship [34].

In a micromirror, when a potential difference is applied to the actuating plate, it generates an electrostatic force that causes the micromirror surface to move within the air cavity. The air cavity is the space between the top reflective micromirror surface and the fixed bottom electrode. As discussed earlier, this movement, or the deflection of the micromirror surface, is also called the stroke of the micromirror. Depending upon the stroke requirements and applications, micromirrors can be fabricated using various

customizable fabrication techniques such as surface micromachining or standard fabrication techniques such as the Multi-User MEMS Process (MUMPs) [35]. Fabrication of electrostatically actuated micromirror using the MUMPs technique is discussed in detail in Chapter 5, as this technique is used in the designed and fabricated micromirrors in this thesis. Electrostatic actuation has several advantages. These actuators benefit from low power consumption, fast response time, high optical scan angle, scan mode both in 1D and/or 2D, simple design structure, and ease of fabrication [20], [36]. Due to these advantages, electrostatic actuation is a preferred method to actuate many micromirrors. Depending upon the geometric design configuration of the actuating electrodes, these electrostatic actuators can be classified into four different categories of parallel-plate actuators, linear comb-drive structure, vertical comb-drive structure, and rotary comb-drive structure. These four categories of electrostatic actuators are illustrated in Figures 2.2(a) to 2.2(d), respectively.

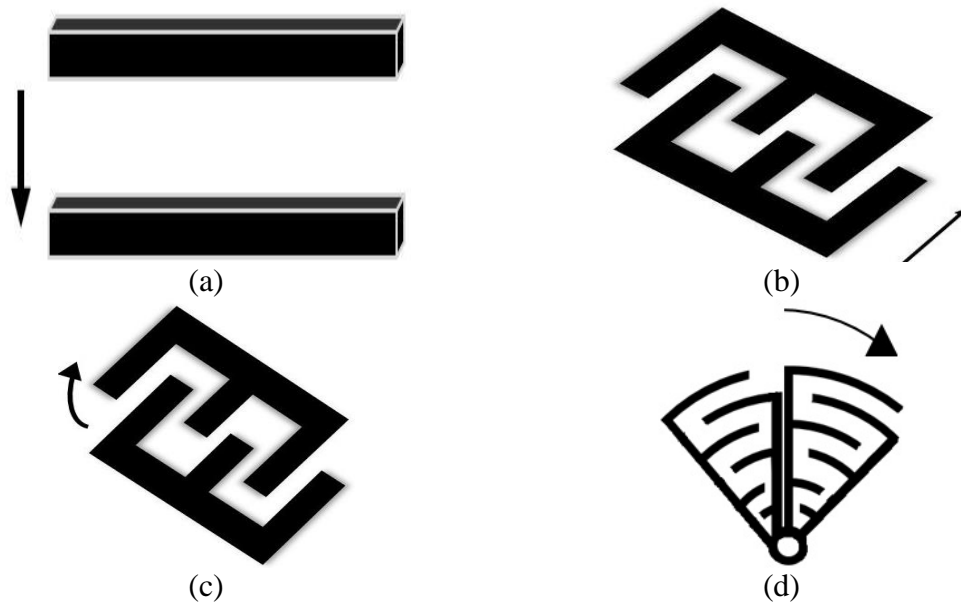


Figure 2.2: Schematic view of electrostatic actuators: (a) parallel-plate actuator, (b) linear comb-drive actuator, (c) vertical comb-drive actuator, and (d) rotary comb-drive actuator.

2.3.1.1 Parallel-Plate Actuator

Conventional electrostatically-actuated micromirrors are composed of two parallel plates that, when actuated, pull the micromirror surface downward towards the bottom plate. Figure 2.3 illustrates a schematic view of parallel-plate actuators, where L and w are the length and width of the plate, respectively, A is the micromirror effective area, V is the applied voltage, and d is the separation gap between the two parallel plates.

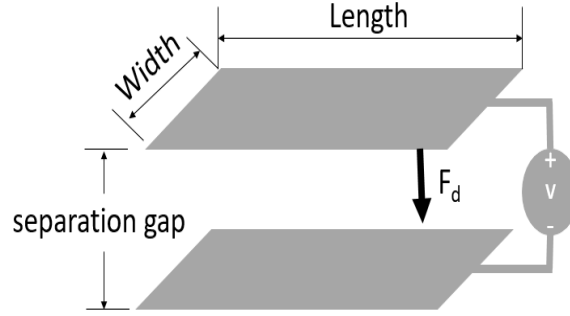


Figure 2.3: Schematic view of a parallel-plate electrostatic actuator.

Ignoring the fringing field effects, the energy stored due to the applied bias voltage between the micromirror's two parallel plates can be calculated from Equation 2.1 [37],

$$W = \frac{1}{2} CV^2 = \frac{\epsilon_0 \epsilon_r A V^2}{2d}, \quad (2.1)$$

where ϵ_0 is the dielectric constant in air and ϵ_r is the relative permittivity of the medium [37]. The generated electrostatic force (F_d) due to the applied voltage between the plates is given by [37]

$$F_d = \frac{\epsilon_0 \epsilon_r A V^2}{2d^2}. \quad (2.2)$$

From Equation 2.2, it can be implied that the electrostatic force is a non-linear function of both the voltage (V) and the gap (d). When the plate is deflected to a distance of Δd due to an input voltage (V), then Equation 2.2 can be re-written as [38]

$$F_d = \frac{\epsilon_0 \epsilon_r A V^2}{2(d+\Delta d)^2}. \quad (2.3)$$

Similarly, the spring force at equilibrium can be stated as [37]

$$F_d = -kd, \quad (2.4)$$

where k is the spring constant.

Parallel-plate actuators are commonly used due to their ease of fabrication and high yields. Traditional micromirrors include a simple parallel-plate design, with an actuator plate that attracts the micromirror surface towards it. Horenstein *et al.* [39] demonstrated a simple micromirror based on a parallel-plate design with an actuator beneath the micromirror surface. The electrostatic force acting on the micromirror surface pushes it downward. This is illustrated in Figure 2.4 (a) and (b).

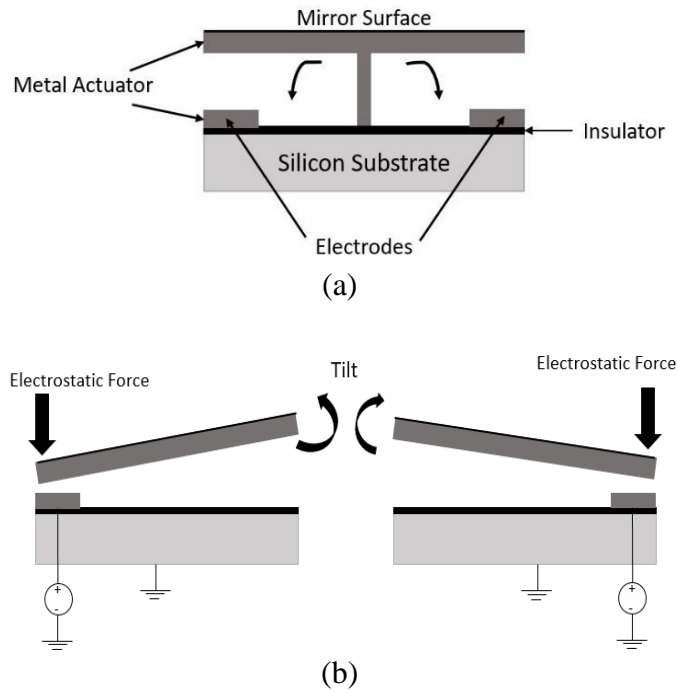


Figure 2.4: Schematic view of (a) simplified cross-sectional image of micromirror actuated by electrostatic force. (b) micromirror surface tilts as a response of the electrostatic force.

One of the main limitations of the design illustrated in Figure 2.4 is the pull-in instability that limits the stroke of the micromirror [40], [41], [42]. When the micromirror is actuated, the micromirror surface moves downward and after reaching $1/3^{\text{rd}}$ -of the air cavity, the

electrostatic force pulling the micromirror down becomes higher than the micromirror plate's restoring force. As a result, the response of the micromirror becomes unstable [41], [43]. This is defined as pull-in instability and it is one of the main factors that affect the stroke of the micromirror [43], [44]. Numerically, pull-in instability occurs when the stroke level of the micromirror reaches 1/3rd of the air cavity [42],

$$d = -\frac{d_0}{3}. \quad (2.5)$$

From Equations 2.2 to 2.5, the pull-in voltage can be calculated as [42]

$$V_{pull} = \sqrt{\frac{8 k d_0^3}{27 \epsilon_0 \epsilon_r A}}. \quad (2.6)$$

In order to overcome the pull-in instability, the separation gap can be increased; however, this increase can lead to fabrication complexity. Another way to rectify the pull-in instability is by introducing extra electrodes to the actuator design in a way that the net resulting electrostatic force is in an upward direction, which will move the micromirror surface upward. This electrostatic force is a repulsive electrostatic force [45], [46].

Hu *et al.* [37] propose an electrostatically-actuated micromirror that is based on a parallel-plate design. This micromirror is actuated by a repulsive electrostatic force that reduces the pull-in instability effect. The micromirror in this configuration is supported by an L-shaped arm that has three fixed bottom electrodes on each side. In their work, an out-of-plane stroke of 1.65 μ m is observed at 100V and the movement of the micromirror surface is upward. The lateral electrostatic forces on the upper plate (L-shaped arm) are equal in magnitude but opposite in direction, they counteract to neutralize each other. Moreover, the electrostatic force produced on the top surface is larger than on the bottom

surface. Therefore, the net electrostatic force points in the upward direction. As a result, the upper plate moves upward.

The electrostatic force acting on the actuator and the movement of the upper plate is illustrated in Figure 2.5. To validate the effect of the additional bottom electrodes and the influence of the fringing fields, COMSOL simulations are conducted on the structure presented in Figure 2.5. The result is illustrated in Figure 2.6. It can be observed that unlike a conventional MEMS cantilever structure with one bottom electrode and one suspended arm, an electrostatically actuated arm with three fixed bottom electrodes has the ability to deflect upward. This can occur when the arm width, bottom electrode separation gap, as well as the bias voltage are optimized.

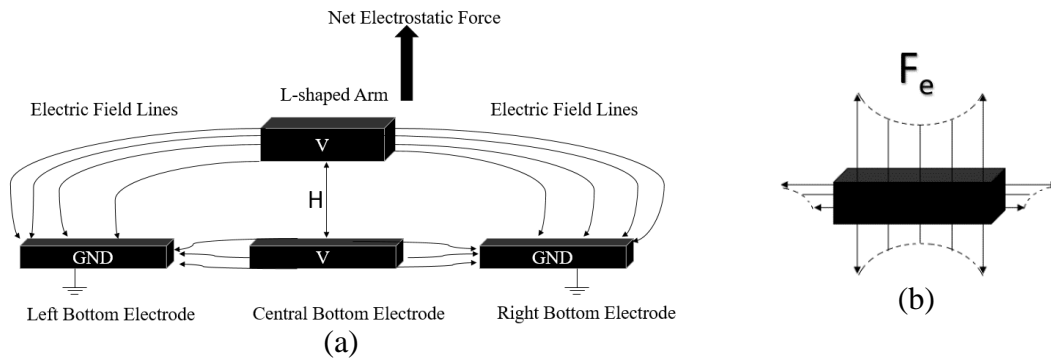


Figure 2.5: Schematic view of (a) a three-bottom-electrode parallel-plate design showing the distribution of the generated electrostatic force, and (b) the resulting electrostatic field on the upper plate.

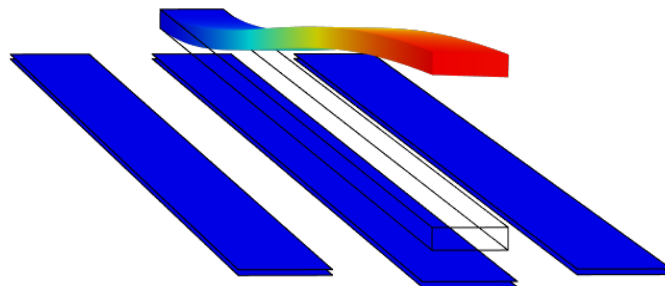


Figure 2.6: COMSOL simulation results conducted in this thesis investigating a parallel-plate design with three fixed bottom electrodes, where the resulting electrostatic force pushes the upper plate upward for an input bias voltage of 50V. The arm's width and length are $8\mu\text{m}$, $400\mu\text{m}$, respectively. The bottom electrodes' length, width, and distance from each other are $400\mu\text{m}$, $10\mu\text{m}$, and $5\mu\text{m}$, respectively.

Another electrostatically-actuated micromirror is demonstrated by Helmbrecht *et al.* [47]. They use surface micromachining techniques to fabricate the actuator array. The micromirror is hexagonal in shape, with a thickness of $20\mu\text{m}$ and sides with lengths of $350\mu\text{m}$. The actuator gap is in excess of $30\mu\text{m}$, which theoretically allows for $10\mu\text{m}$ of stroke, that is, $1/3^{\text{rd}}$ of the gap. However, in practice, it is safer to limit the stroke to $1/4^{\text{th}}$ of the gap [47]. Thus, a stroke of $7.5\mu\text{m}$ is achieved for considerable voltage bounds, which is for less than 130 DC bias voltage. Similarly, Aron *et al.* [38] propose a monolithic integration of a vertical micromirror in the center of a micro-bridge. This design is ideal for optical switching applications. It abides by the requirement of bi-stability, bi-directionality, large initial out-of-plane stroke, and low operational voltage [38]. This micromirror was fabricated and tested and an initial out-of-plane stroke of $27\mu\text{m}$ was obtained. Another example is demonstrated by Bai *et al.* [20] who present a 2-degree-of-freedom silicon-on-insulator (SOI) micromirror with sidewall (SW) electrodes. The biaxial micromirror is actuated by electrostatic actuators. The dimension of the micromirror is $1000\mu\text{m}$ by $1000\mu\text{m}$, and $35\mu\text{m}$ thick. The measured maximum mechanical scanning angle is $\pm 11^\circ$ at the static operating voltage and is $\pm 21^\circ$ at resonance frequency driving.

The mechanical scanning angle of a micromirror is the angle that the micromirror deflects and causes the incident laser beam to deflect at twice that angle. The mechanical scanning angle is half of the optical scanning angle. These designs are able to achieve a large stroke at the expense of cost and design complexity. These are arrays of micromirrors tailored for space applications or different applications with several different design considerations. In order to fabricate such variations with conventional lithographic

methods, it is necessary to produce over 200 photomasks, which drastically increases the cost and complexity of the fabrication [48].

2.3.1.2 Comb-Drive Actuator

Depending upon the geometric configuration of the actuator plate, actuators can be divided into linear comb-drive actuators, vertical comb-drive actuators, and rotary comb-drive actuators. A linear comb-drive actuator has a comb configuration that resembles the human hand being interlaced [35]. A schematic view of this actuator is illustrated in Figure 2.2(b). The actuation direction is towards the length of the comb fingers. Assuming the gap between the electrode is d , the thickness of the comb finger is t , the input voltage supply is V , and the spring constant for beam suspension is k_{eff} , then the governing principle equation of the motion of a general comb-drive actuator is given by [35]

$$F_{comb} = \partial_{comb} k_{eff} \quad . \quad (2.7)$$

Or,

$$\partial_{comb} = \frac{F_{comb}}{k_{eff}} = n \frac{\epsilon t V^2}{d} = \frac{L^3}{4 E_{spring} h b^3}, \quad (2.8)$$

where ∂_{comb} is the deflection of the actuator connected to the beam suspension, F_{comb} is the electrostatic force due to the actuator, n is the number of pairs of comb fingers, ϵ is the permittivity of the media, h and b are the height and width of the spring, respectively, L is the length of beam suspension, and E is Young's modulus of the material. He *et al.* [45] propose a circular micromirror that is actuated by a comb drive actuator. Their structure shows that the actuator achieves a static out-of-plane stroke of $86\mu\text{m}$ for a driving voltage of 200V and can also achieve 2D rotation within a mechanical rotation range of $\pm 1.5^\circ$.

Similarly, a vertical comb-drive actuator's structure may resemble a linear comb-drive structure; however, the main characteristic of a vertical comb-drive actuator is that the direction of the electrostatic force is perpendicular to the length of the finger [49]. A schematic view of this actuator is illustrated in Figure 2.2(c). Furthermore, a rotary comb-drive actuator is also similar to a linear comb actuator, but the comb fingers are located along the radius of the device [35]. The schematic of a rotary comb-drive actuator is illustrated in Figure 2(d). The main difference in design is that a rotary comb-drive actuator uses flexure hinges rather than spring suspensions [35], [50]. One of the main disadvantages of comb-drive actuators is that they are difficult to fabricate [35], [50].

2.3.2 Electromagnetic Actuation

Electromagnetic actuation commonly uses ferromagnetic material such as permalloy deposited on a micro-actuator and a coil for inductance underneath it to generate a magnetic field [51]. When driven by electromagnetic force, the magnetic field produced by the magnet and the current flowing around the coil that surrounds the micromirror generate a Lorentz force that turns the micromirror following Fleming's left-hand rule [52]. This is illustrated in Figure 2.7.

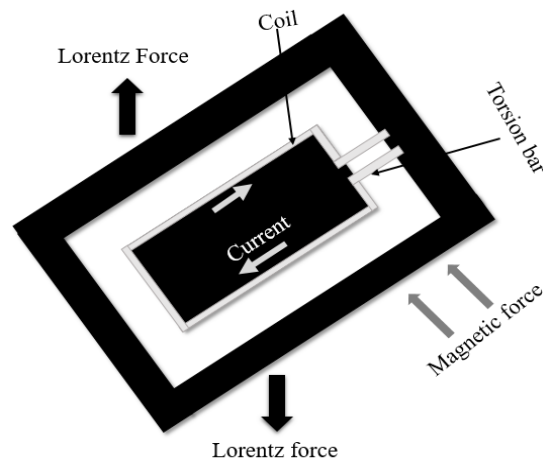


Figure 2.7: Schematic view of an electromagnetic actuator.

When a coil is subjected to a perpendicular magnetic field and a current flowing in the coil, it produces a force called a Lorentz force [52]. The magnitude of the Lorentz force is directly proportional to the strength of the current and the magnetic field. The micromirror is supported by a torsion bar, which serves as the axis for rotation. When a current flows in the coil that surrounds the mirror, it produces a torque (Lorentz force) that rotates or tilts the micromirror and the elastic force of the torsion bar is exerted in the opposite direction. The micromirror stops when these opposite forces are equal to each other. The deflection angle can be changed by varying the magnitude of the current and magnetic field.

Generally, electromagnetic actuation provides more displacement as compared to other actuation techniques [53]. For instance, Kim *et al.* [54] present a scanning micromirror device that has an optical scanning angle of $\pm 20^\circ$ in both axes, with voltages as low as 1-3V. Similarly, Iseki *et al.* [55] achieve a large displacement by implementing electromagnetic actuation, achieving a large scan angle of 8° for 0.75mA of current. The micromirror shows a linear relation to the applied current. Despite resulting in relatively more displacement, the actuation technique has disadvantages such as high power consumption and a complicated fabrication process due to the deposition of ferromagnetic materials [35], [51]. Furthermore, electromagnetic actuators require shielding and the fabrication of ferromagnetic material, which increases the overall size of the micromirror and for such micro-level devices, there is very little room for the electrically-conducting coil, which is required for electromagnetic induction [35], [51].

2.3.3 Piezoelectric Actuation

The principle of operation of piezoelectric actuation is that the stress in the materials is caused by the electric field applied to the actuators. Piezoelectric actuators can be two

different types: bimorph and unimorph [56], [57]. When two different materials with different piezoelectric properties are subjected to an electric field, they can be contracted or extended [56], [57]. This type of piezoelectric actuator is known as a bimorph actuator. On the other hand, when one material is piezoelectric and the other one is inactive, it is known as a unimorph actuator. Recent developments have used piezoelectric actuation in order to actuate scanning micromirrors due to its ability to achieve large static deflection with low power consumption [58]. However, it is difficult to control and has a slow response time [58]. As compared to other piezoelectric films, lead zirconate titanate (PZT) has emerged as a highly recognized piezoelectric material because it exhibits large actuation forces, and PZT is easily micromachinable in MEMS applications [59].

2.4 Summary and Conclusion

In this chapter, different types of actuation techniques for micromirrors are presented. Electrostatic actuation is one of the popular actuation techniques for micromirrors because of advantages such as fast response, ease of fabrication, and large stroke angle. One of the main disadvantages of electrostatic actuation is pull-in instability. Depending on the design of the actuator, electrostatic actuation can be further classified into parallel-plate and comb-drive actuators. Comb-drive actuators can be furthermore classified into linear comb-drive, vertical comb-drive, and rotary comb-drive. Some of the other actuation techniques that are available for micromirrors are electromagnetic and piezoelectric. Table I lists the advantages and disadvantages of each actuation mechanism.

Because of the advantages provided by electrostatic actuation, in this thesis, this actuation mechanism is used to drive the proposed and fabricated MEMS micromirror. Therefore, in the following chapter, the parallel-plate, electrostatically-actuated

micromirror will be discussed and investigated in detail. Its principle of operation and the design parameters that affect the stroke of the proposed micromirror will be further discussed. COMSOL Multiphysics software is used to simulate the design in order to study the effect of design parameters on the stroke of the developed micromirror.

Table I: Comparison of electrostatic, electromagnetic and piezoelectric actuators.

Actuation Mechanism	Advantages	Disadvantages
Electrostatic Actuator	<ul style="list-style-type: none"> • Low power consumption • Fast response time • Small scan angle for parallel plate and large scan angle for comb-drive structures. • Easy to integrate and implement with CMOS technology • Simple fabrication process 	<ul style="list-style-type: none"> • High voltage for actuation • Limited operation range due to the pull-in instability
Electromagnetic Actuator	<ul style="list-style-type: none"> • Low actuation voltage • Relatively large displacement 	<ul style="list-style-type: none"> • Difficult to fabricate the magnetic material with current CMOS technology • Challenge to minimize the size of devices • High power consumption
Piezoelectric Actuator	<ul style="list-style-type: none"> • Higher switching speed • Low power consumption 	<ul style="list-style-type: none"> • Small displacement range • Slow response time • High voltage for actuation • Difficult to control

3 CHAPTER III: INVESTIGATION AND ANALYSIS OF DESIGN PARAMETERS

3.1 Introduction

In an electrostatically-actuated micromirror, the electrostatic force generated between the actuator plates is responsible for the movement of the micromirror surface [32], [33], [60]. The micromirror surface deflects in response to the applied voltage that creates this electrostatic force. As discussed in Section 2.2, deflection of the micromirror surface is also known as the “stroke” of the micromirror, which is defined as the distance that the micromirror surface is able to move within the device air cavity. The air cavity in a micromirror is the space between the top reflective micromirror surface and the fixed bottom electrode. In addition to the input voltage, as shown in Equation 2.2, there are other critical design parameters, such as the area of the micromirror and air cavity, that affect the stroke of the micromirror [37]. In an effort to maximize the stroke of the proposed MEMS micromirror, an advanced parallel-plate micromirror is presented and studied in this chapter.

In this chapter, a traditional micromirror is presented. Then, the design of the proposed parallel-plate micromirror with three fixed bottom electrodes is explained in Section 3.3. An electrostatically-actuated microstructure undergoes the fringing field effect, which affects the stroke of the micromirror. Therefore, the effect of the fringing field on the stroke of the micromirror is further investigated and explained. In addition, the device's critical parameters, such as input voltage, the width of the arm, and distance between the fixed bottom electrodes are analyzed in order to find their effects on the stroke

of the proposed micromirror. In Section 3.4, COMSOL Multiphysics is employed to analyze the proposed micromirror designs and to identify the relationship between the design parameters and the micromirror's performance.

3.2 Conventional Electrostatically-Actuated MEMS Micromirror

A conventional electrostatically-actuated micromirror is composed of two parallel plates that, when actuated, pull the micromirror surface towards the bottom plate. Traditionally, the layer deposited over the top actuator plate is a reflective micromirror surface and the bottom plate is another actuator plate. When an input voltage is applied to these parallel plates, an electrostatic force is generated between the plates, and is responsible for the movement of the micromirror surface. The principle of operation and actuation mechanism of a conventional parallel-plate micromirror is discussed in Section 2.3.1. A schematic view of two conventional micromirrors is shown in Figures 3.1(a) and 3.1(b).

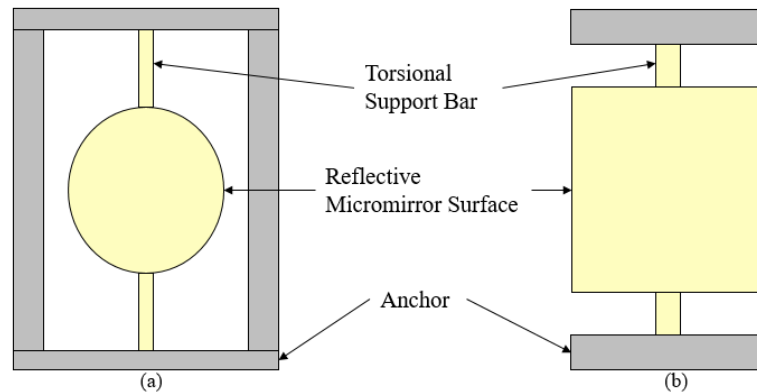


Figure 3.1: Top view of two conventional electrostatically-actuated MEMS micromirrors.

The main advantage of a conventional parallel-plate micromirror is that it is easy to fabricate. However, one of the major disadvantages is pull-in instability. As discussed in Section 2.3.1, pull-in instability will limit the stroke of the micromirror. However, in this work a three-bottom-electrode configuration is utilized that suggests a method to reduce the effect of the pull-in instability by ensuring the movement of the micromirror surface is

upward rather than downward. As illustrated in Figure 3.13, upon actuation, when one end of the micromirror surface is pushed upward, the other end goes down, therefore, tilting the micromirror surface. However, the amplitude of the deflection is not equal in both ends. The upward deflection is higher than the downward deflection. Therefore, this upward movement, rather than the traditional downward deflection of the micromirror surface, reduces the effect of pull-in instability. Details about movement and tilting of the micromirror surface are explained in Chapter 4. Micromirror with an L-shaped arm and three bottom electrodes are explained in the upcoming Section 3.3.

3.3 MEMS Micromirror with an L-shaped Arm and Three Fixed Bottom Electrodes

Unlike a conventional electrostatically-actuated micromirror, in this thesis, a parallel-plate micromirror with an L-shaped arm is presented and developed. The L-shaped arm is chosen to provide more flexibility for the arms to move upward. Figure 3.2 illustrates the proposed structure. In this configuration, the micromirror is supported by four L-shaped arms, which are anchored at the end of the arms and on all sides of the micromirror.

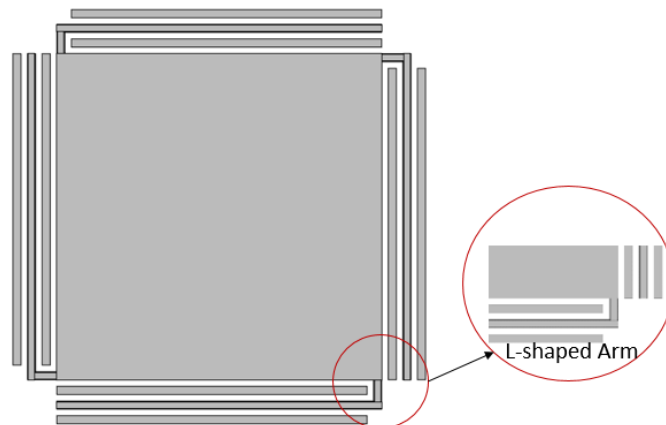


Figure 3.2: Top view of the micromirror showing the L-shaped arm and three fixed bottom electrodes generated using COMSOL simulation software.

In addition, three fixed bottom electrodes are employed beneath the L-shaped arms on all four sides of the micromirror to enforce an upward movement in the micromirror instead of the traditional downward deflection. This upward movement of the arm is explained in Chapter 2 and is also illustrated in Figures 2.5 and 2.6.

In the first step of the investigation, the three bottom electrodes are chosen to be equal in dimension and are separated by an equal distance from each other. In this design, the top layer, which is the reflective micromirror surface, is deposited over the upper actuator plate. An insulating layer is deposited over the substrate to provide electrical isolation. The layer above the insulator layer is composed of the fixed bottom electrodes. Details about the fabrication layers will be discussed in Chapter 5. A schematic view of one of the designed micromirrors in MEMSPro using the PolyMUMPs fabrication technique is illustrated in Figure 3.3 and its cross-sectional view is illustrated in Figure 3.4, showing the connections of the actuators to the main body of the micromirror. In this configuration, the design parameters of the presented micromirror, such as the area of the micromirror, input voltage, and width of the L-shaped arm, affect the stroke of the micromirror.

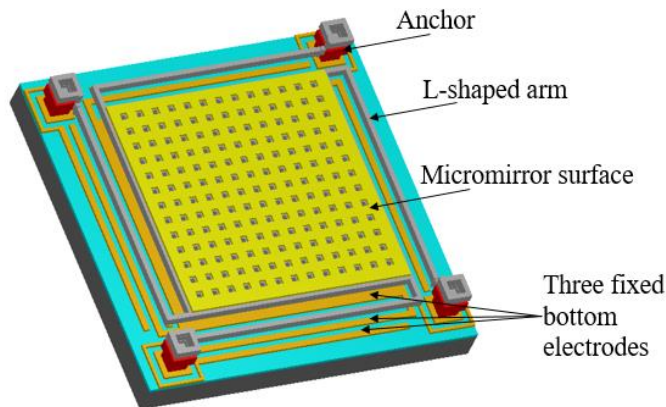


Figure 3.3: Schematic view of the micromirror Design 3 in MEMSPro using the PolyMUMPs fabrication technique. Details about the different proposed micromirror designs are explained in Chapter 4.



Figure 3.4: Cross-sectional view of the proposed micromirror Design 3 in MEMSPro using the PolyMUMPs fabrication layer sequence. Fabrication steps are described in detail in Chapter 5.

In addition, the separation gap between the fixed bottom electrodes also influences the stroke of the micromirror. Changing the separation gap between the fixed bottom electrodes changes the fringing field, which affects the stroke of the micromirror. The effect of the fringing field on the stroke of the micromirror is discussed in detail in Section 3.3.1. In this chapter, design parameters including the input voltage, width of the L-shaped arm, and the distance between the three fixed bottom electrodes are investigated and analyzed in order to maximize the performance of the proposed micromirror.

3.3.1 Effect of Fringing Field on the Stroke

An electrostatically-actuated microstructure benefits from the fringing field effect [43], [44], [61]. In a parallel-plate capacitive design, the fringing field effect is the bending of the electric flux lines at the edge of the capacitor. The fringing field effect is also known as “edge effect” or simply referred to as fringing [62]. The electric flux lines that are inside the parallel plates are straight and uniform. However, at the edges, the electric flux lines bend, as a point charge creates a spherical field [62]. COMSOL Multiphysics simulation software and the MEMS module are used to investigate this effect in the electrostatically-actuated microstructure. The bending of electric flux lines at the edge of parallel plates is simulated in COMSOL and the results are illustrated in Figure 3.5. A parallel-plate capacitor with a radius of 10cm and a thickness of 0.5cm with a gradually increasing air domain around it is investigated. The COMSOL simulation results show that the

capacitance increases with an increase of the air domain around the capacitor because the bigger air domain is able to contain all the effective electric flux lines.

Therefore, in order to contain all the electric flux lines and to eliminate the inaccuracy of the simulation, the air domain around the device should be chosen large enough to contain all the influencing electric flux lines. However, this results in an increase in the number of simulated mesh points and simulation time, as discussed in Section 3.4.1. Figure 3.5 illustrates the air domain around the capacitor, which has a radius of 33cm and is optimized to contain the electric flux lines inside the air domain. Figure 3.6 shows the direction and effect of the fringing field for three bottom electrodes employed in the proposed micromirror design. The analysis of COMSOL simulation results in order to ensure the electric flux lines are contained inside the air domain around the micromirror is explained in Chapter 4. In the three bottom electrode configuration, the positioning and the separation gap between the bottom electrodes also affect the stroke of the micromirror. Figure 3.6 illustrates the generation of the electric flux lines for a three bottom electrode structure.

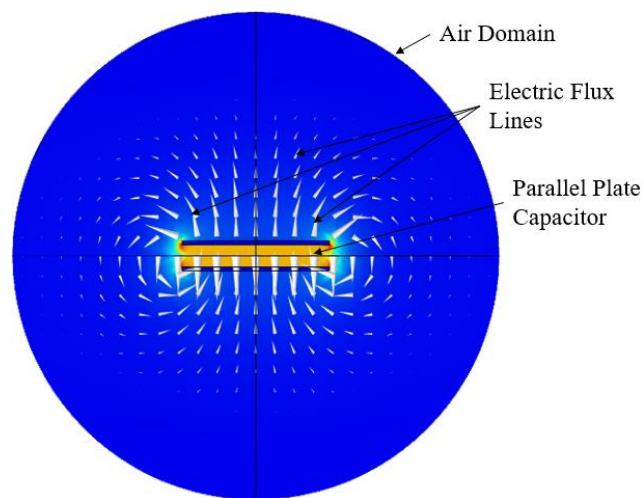


Figure 3.5: COMSOL electrostatic simulation results showing the fringing fields at the edge of the general circular parallel plate capacitor with a radius of 10cm and a thickness of 0.5cm.

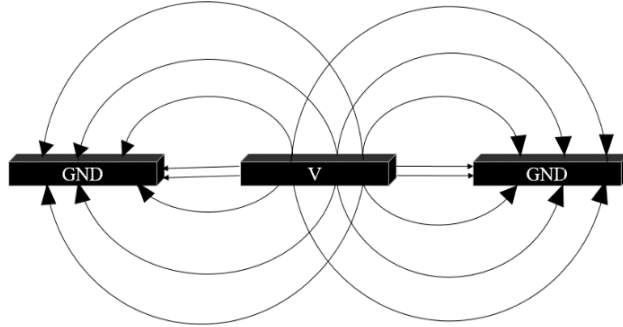


Figure 3.6: Fringing field effects for the three bottom electrode configuration employed in this work.

In this thesis, a MEMS micromirror with three fixed bottom electrodes is analyzed and developed. In this device, the positioning of the fixed bottom electrode affects the fringing field, which influences the stroke of the micromirror. In order to maximize the stroke level of the designed micromirror, the effect of the separation gap between the fixed bottom electrodes is investigated in detail in Section 3.4.2.3.

3.4 COMSOL Simulation Results of the Micromirror

3.4.1 Finite Element Analysis

Fine element analysis (FEA) is used to analyze the effect of design parameters on the proposed MEMS micromirror performance. In this thesis, COMSOL Multiphysics simulation software and the MEMS module are used to investigate the influence of the device properties. Furthermore, meshing is used to divide the micromirror into smaller elements as solved data points. In these simulations, the level of achieved stroke should be independent of the solved data points or mesh points. Mesh type in COMSOL is defined by the number of smaller elements that each domain is divided into including “coarse”, “normal”, “fine”, “finer”, “extra fine”, and “extremely fine” meshing. Figure 3.7 illustrates the micromirror with “finer” mesh; the micromirror is divided into 2,136,622 smaller elements.

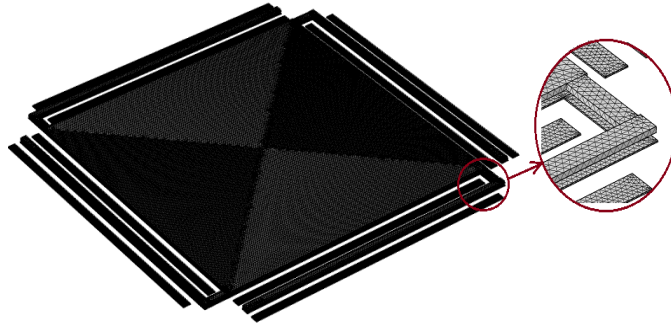


Figure 3.7: The $400\mu\text{m}$ by $400\mu\text{m}$ micromirrors in Designs 1 to 4 with “finer” mesh; the micromirror is divided into 2,136,622 smaller elements.

The micromirror presented in Figure 3.7 is $400\mu\text{m}$ by $400\mu\text{m}$ and its thickness is $2\mu\text{m}$, which is equal to the thickness of the top layer in the PolyMUMPs fabrication process. Therefore, the meshing behavior exhibited by this micromirror will be similar to the developed micromirrors, which is discussed in Chapter 4. Figure 3.8 illustrates the COMSOL simulation results showing the relation between the stroke of the micromirror and mesh type. Figure 3.9 illustrates the relationship between the stroke of the micromirror and the simulation time.

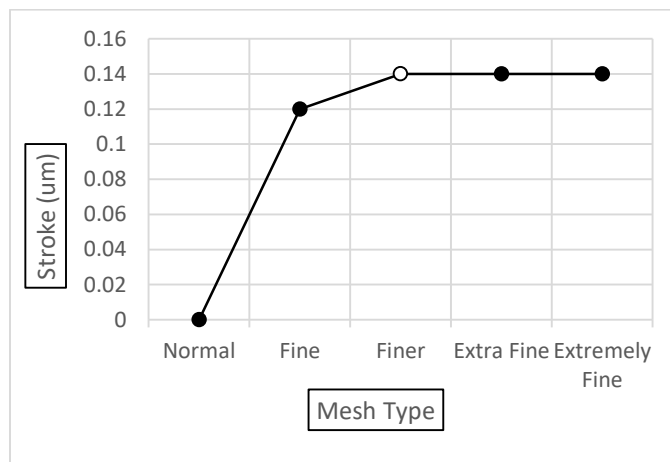


Figure 3.8: COMSOL simulation results showing the stroke level versus mesh type for the parallel-plate micromirror.

As shown in Figure 3.8 and Figure 3.9, the stroke of the micromirror increases insignificantly for meshes denser than “finer”, but the simulation time increases significantly for meshes denser than “finer”. Therefore, for the proposed micromirror

design, a “finer” mesh is chosen because the stroke becomes independent of the number of mesh elements after this point.

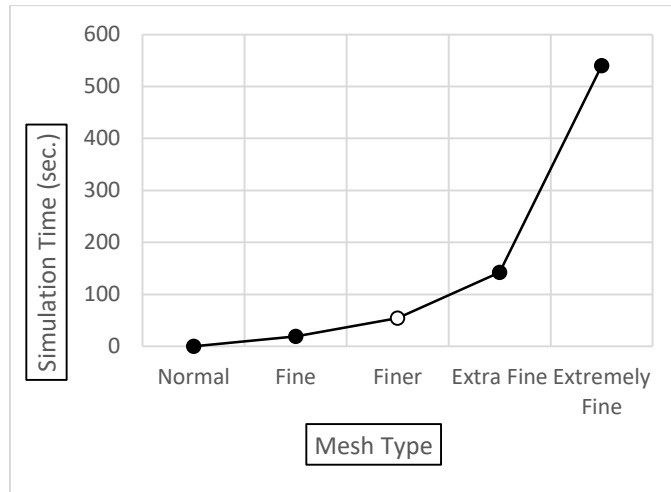


Figure 3.9: COMSOL simulation results showing simulation time versus mesh type for the parallel-plate micromirror.

3.4.2 Critical Parameters' Influence on the Stroke

In order to analyze the effect of device critical parameters on the stroke of the micromirror, the device's physical properties, as well as biasing conditions, are investigated and evaluated. This investigation allows the identification of the deflection pattern across different components and, therefore, allows the identification of the critical design parameters that will maximize the performance of the micromirror. Similar to the conventional electrostatically-actuated micromirror, first, one arm with one fixed bottom electrode beneath it is investigated. For one arm with one fixed bottom electrode, the simulation results indicate that the deflection is downward. The upper arm is attracted to the bottom plate, due to the electrostatic force generated between the actuating plates.

Figure 3.10 illustrates the simulation results for an arm with one fixed bottom electrode with a width and length of $10\mu\text{m}$ and $400\mu\text{m}$, respectively, showing the downward movement of the arm for an applied voltage of 50V. This downward deflection

of the arm is not desired because the electrostatically-actuated micromirror undergoes pull-in instability, which will limit the stroke of the micromirror. Pull-in instability is a phenomenon in which when the micromirror is actuated, the micromirror surface moves downward and after reaching $1/3^{\text{rd}}$ -of the air cavity, the electrostatic force pulling the micromirror down becomes higher than the micromirror plate's restoring force. As a result, the response of the micromirror becomes unstable [43], [41].

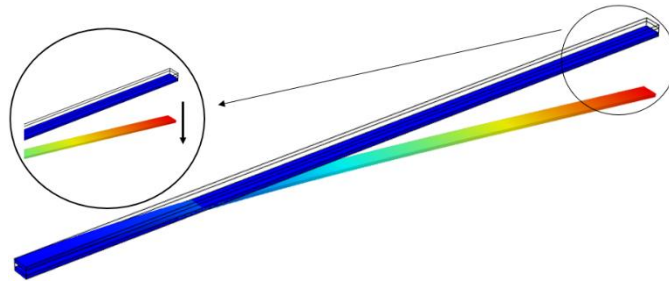


Figure 3.10: The schematic view of an arm with one fixed bottom electrode showing the downward movement of the arm. The arm's width, length, and voltage are $8\mu\text{m}$, $400\mu\text{m}$, and 50V , respectively, whereas the width and length of the bottom electrode are $10\mu\text{m}$ and $400\mu\text{m}$, respectively.

Therefore, as illustrated in Figure 2.5, in order to reduce the effect of the pull-in instability and to enforce upward movement of the arm, three fixed bottom electrodes are employed under the arm. In this configuration, the upward movement is achieved because the lateral electrostatic forces on the upper arm are equal in magnitude but opposite in direction. As a result, they counteract to neutralize each other [37]. Furthermore, the upper arm is $2\mu\text{m}$ narrower than the fixed bottom electrodes. As a result, the electrostatic force produced on the upper arm is larger than on the fixed bottom electrodes. Therefore, the net electrostatic force points in the upward direction [37].

Figure 3.11 illustrates the COMSOL simulation results of the upward movement of the arm with width, length, and applied bias voltage of $8\mu\text{m}$, $400\mu\text{m}$, and 50V , respectively, and three bottom electrodes with width, length, and separation gap of $10\mu\text{m}$, $400\mu\text{m}$, and $5\mu\text{m}$, respectively.

In this simulation, an input DC bias voltage is applied to the arm and the central fixed bottom electrode and the side bottom electrodes are grounded. The left end of the arm and three bottom electrodes are fixed. This allows the free end of the arm to move when it is actuated.

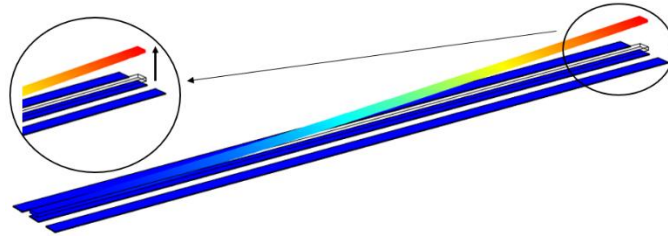


Figure 3.11: The schematic view of an arm with three fixed bottom electrodes indicating the upward movement of the arm. The arm's width, length, and applied bias voltage are $8\mu\text{m}$, $400\mu\text{m}$, and 50V , respectively, whereas the width, length, and separation gap between the bottom electrodes are $10\mu\text{m}$, $400\mu\text{m}$, and $5\mu\text{m}$, respectively.

Figures 3.12 and 3.13 illustrate the upward movement of the L-shaped arm and the L-shaped arm with a micromirror surface, respectively. In these simulations, an input DC bias voltage of 50V is applied to the arm and the central fixed bottom electrode and the side bottom electrodes are grounded.

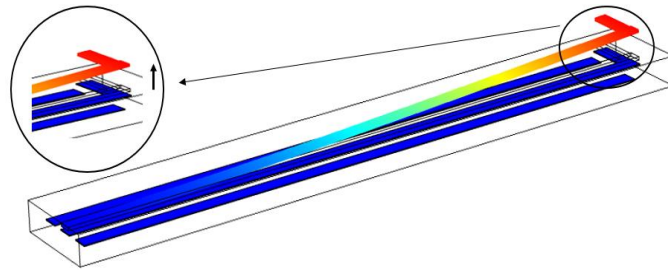


Figure 3.12: The schematic view of an L-shaped arm with three fixed bottom electrodes showing the upward movement of the arm. The arm's width, length, and applied bias voltage are $8\mu\text{m}$, $400\mu\text{m}$, and 50V , respectively, whereas the width, length, and separation gap between the bottom electrodes are $10\mu\text{m}$, $400\mu\text{m}$, and $5\mu\text{m}$, respectively.

The left end of the arm and three bottom electrodes are fixed. In these simulations, the arm width and length are $10\mu\text{m}$ and $400\mu\text{m}$, respectively, the bottom electrodes width, length, and separation gap are $10\mu\text{m}$, $400\mu\text{m}$, and $5\mu\text{m}$, respectively (similar to Figure 3.11), and the micromirror width and length are $10\mu\text{m}$ and $400\mu\text{m}$, respectively.

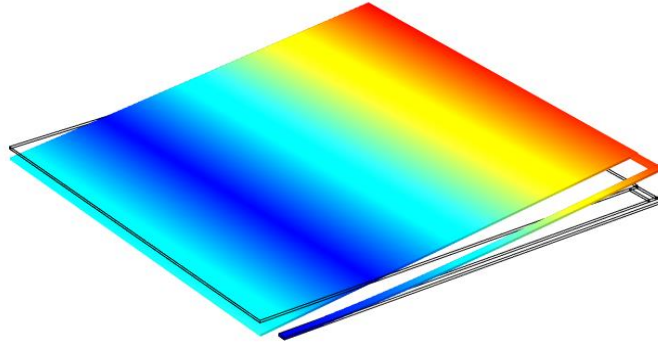


Figure 3.13 The schematic view of the micromirror with an L-shaped arm and three fixed bottom electrodes showing the upward movement of the micromirror and its arm. The arm's width, length, and applied bias voltage are $8\mu\text{m}$, $400\mu\text{m}$, and 50V , respectively, whereas the width, length, and separation gap between the bottom electrodes are $10\mu\text{m}$, $400\mu\text{m}$, and $5\mu\text{m}$, respectively. When one end of the arm goes up, the other end goes down, which tilts the micromirror surface.

Therefore, as shown in Figure 3.11 to Figure 3.13, in this micromirror with the above-mentioned dimensions, when three electrodes are employed beneath the arm, the arm and the micromirror is pushed upward. This is because the electrostatic force produced on the upper arm is larger than on the fixed bottom electrodes. Moreover, the lateral electrostatic forces on the upper arm are equal in magnitude but opposite in direction, which neutralize each other. Consequently, the arm and micromirror surface is pushed upward.

3.4.2.1 Effect of Input Voltage

As can be seen from Equation 2.2, the electrostatic force, which is responsible for the deflection of the micromirror surface, increases with increasing input voltage. However, this relation is not linear. In this work, the designed micromirror performances are investigated for an input voltage ranging from 5V to 100V . The pull-in voltage will limit the stroke of the micromirror, but this voltage range is considered an appropriate operating range for this investigation. Pull-in voltage depends upon variables such as the spring constant of the device, input bias voltage, air cavity between the parallel plates, and area of the micromirror. Therefore, the range of input DC bias voltage will be different for the different proposed designs, which is presented in Chapter 4.

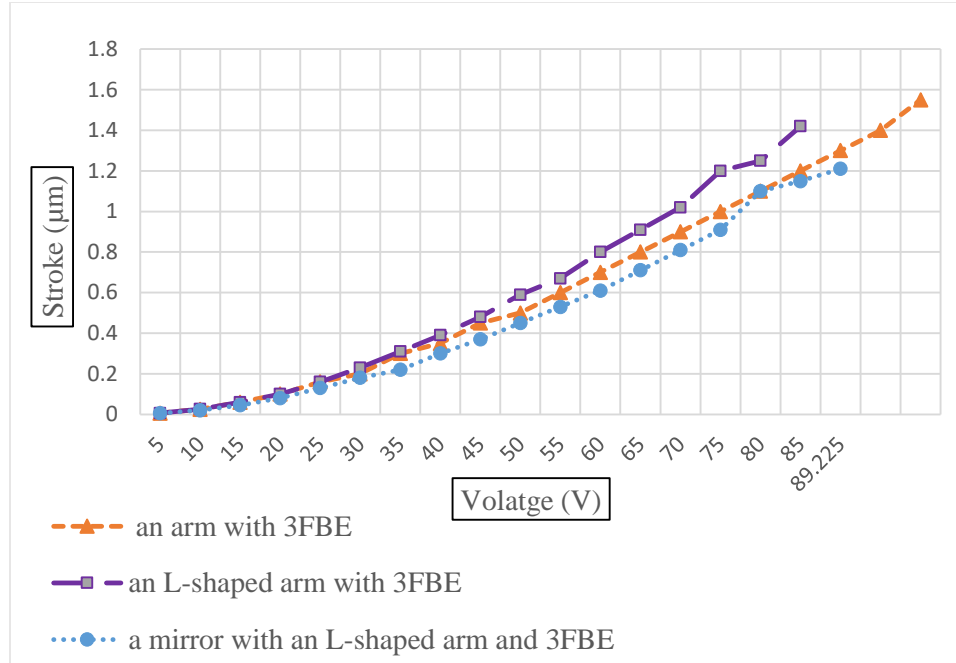


Figure 3.14: COMSOL simulation results illustrating deflection versus voltage for an arm, an L-shaped arm, and a micromirror with an L-shaped arm. The length and width of the L-shaped arm are $400\mu\text{m}$ and $8\mu\text{m}$, respectively. The width of the bottom electrodes is $10\mu\text{m}$ and they are separated by an equal distance of $8\mu\text{m}$.

3.4.2.2 Effect of Width of the Arm

In the investigated three bottom electrode configuration, the width of the arm affects the stroke of the micromirror. Due to the PolyMUMPs fabrication limitation, the arm should be at least $2\mu\text{m}$ wide. The width of the bottom electrodes is $10\mu\text{m}$ and, in order to maximize the stroke, the upper arm should be narrower than the bottom electrodes. Therefore, for this investigation, the width of the arm is gradually increased from $2\mu\text{m}$ to $10\mu\text{m}$. From Figure 3.15, it is observed that the deflection decreases with an increase in the width of the upper arm. When the width of the L-shaped arm is increased, the effect of the fringing field that creates the upward deflection is reduced. Moreover, an increase in the width of the arm will also increase the weight of the arm, thereby decreasing the stroke of the micromirror with increasing the width of the L-shaped arm. When a micromirror with an arm narrower than $8\mu\text{m}$ is actuated, COMSOL is unable to return a result.

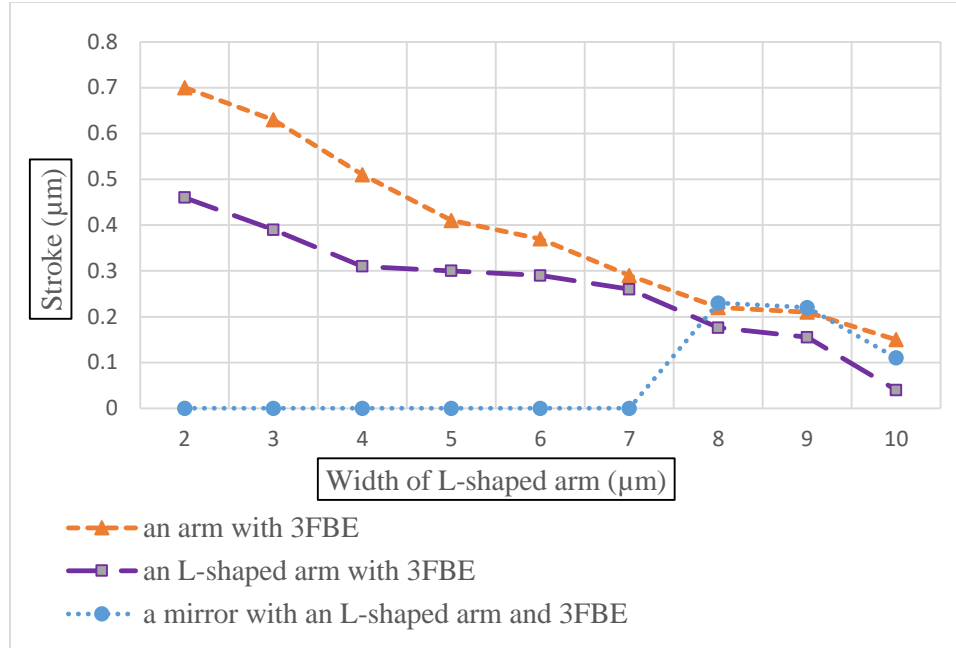


Figure 3.15: COMSOL simulation results illustrating deflection versus width of the arm for an L-shaped arm, an L-shaped arm with 3FBE, and a micromirror with an L-shaped arm and 3FBE. The length and width of the L-shaped arm are $400\mu\text{m}$ and $8\mu\text{m}$, respectively. The width of the bottom electrodes is $10\mu\text{m}$, which are separated by an equal distance of $8\mu\text{m}$.

Therefore, from Figure 3.15, it can be implied that the upper arm should be at least $8\mu\text{m}$ wide, in order to hold the micromirror while deflecting. If the width of the upper arm is less than $8\mu\text{m}$, the micromirror becomes unstable.

3.4.2.3 Effect of the Separation Gap Between Three Fixed Bottom Electrodes

When the separation gap between the fixed bottom electrodes is increased, it increases the overall area of the device. In addition, it also increases the fringing field. The placement and the separation gap between the electrodes affect the stroke of the micromirror. Therefore, in this investigation, the separation gap between the electrodes is increased from $1\mu\text{m}$ to $10\mu\text{m}$, with a $1\mu\text{m}$ step size. The separation gap is not increased beyond $10\mu\text{m}$, because increasing the separation gap between the electrodes will significantly increase the overall area of the device. Figure 3.16 illustrates the simulation results and the effect of the separation gap between the fixed bottom electrodes and the stroke of the micromirror. The

stroke increases with an increase in the separation gap between the fixed bottom electrodes. Furthermore, when the separation gap is less than or equal to $2\mu\text{m}$, the upper arm moves downward. From this, it can be implied that the minimum separation gap between the fixed bottom electrode is $2\mu\text{m}$, in order to achieve an upward deflection.

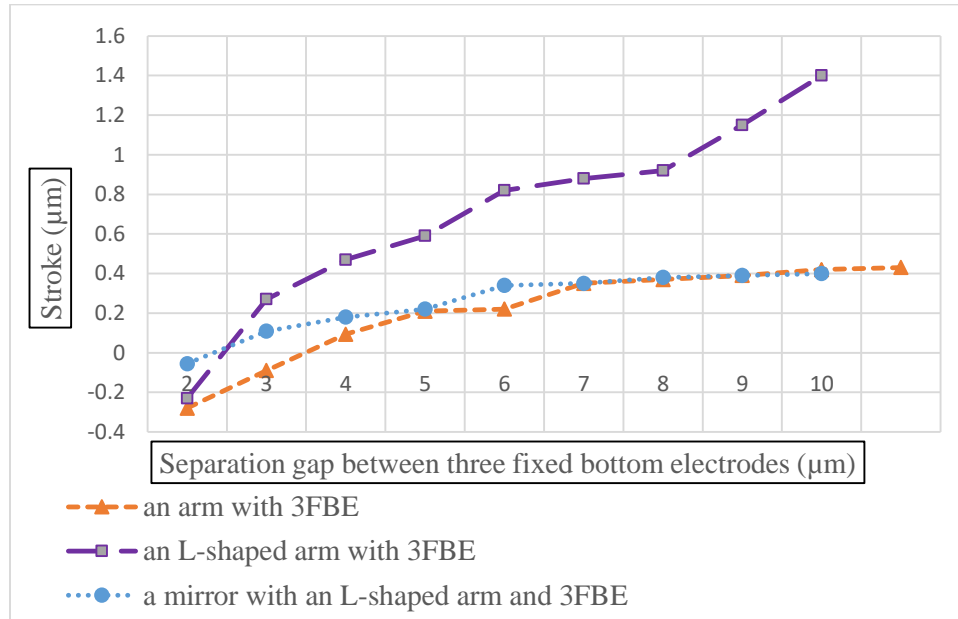


Figure 3.16: COMSOL simulation results illustrating deflection versus separation gap between fixed bottom electrodes for an arm, an L-shaped arm, and a micromirror with an L-shaped arm. The length and width of the L-shaped arm are $400\mu\text{m}$ and $8\mu\text{m}$, respectively. The width of the bottom electrodes is $10\mu\text{m}$, which are separated by an equal distance of $8\mu\text{m}$.

When the separation gap is increased beyond $8\mu\text{m}$, the increase in the deflection is not significant. Therefore, for the proposed micromirror, the separation gap between the fixed bottom electrode is $8\mu\text{m}$, due to the trade-off between fabrication limitations as well as the overall dimension of the device and their effects on the micromirror level of stroke.

3.5 Summary and Conclusion

Critical design parameters including the input voltage, width of the L-shaped arm, and separation gap between the fixed bottom electrodes are investigated to analyze their effect on the stroke of the micromirror. COMSOL Multiphysics software and the MEMS module

are used to analyze the designs. “Finer” mesh is chosen since the evaluation presented in Section 3.4.1 indicates that the “finer” mesh ensures an accurate simulation result. For meshes that are denser than “finer” mesh, such as “extra fine” and “extremely fine” mesh, there is no significant change in the deflection whereas the simulation time is considerably higher. Therefore, the “finer” mesh is used for the simulation of the proposed micromirror design in Chapter 4.

The simulation results indicate that as the input DC bias voltage increases, the deflection of the upper arm increases. However, as the width of the arms increases, the deflection decreases. Moreover, as the separation gap between the fixed bottom electrodes increases, the deflection of the upper arm increases. This investigation helps to identify the design parameters that yield the maximum stroke of the micromirror. The proposed micromirrors all have widths of $8\mu\text{m}$ for the arm that anchors the micromirror on all four sides. When the separation gap between the fixed bottom electrodes is increased from $2\mu\text{m}$ to $10\mu\text{m}$, the deflection also increases. However, when the separation gap is below $2\mu\text{m}$, the deflection is negative, which means the upper arm is deflecting downward rather than moving upward. When the separation gap is increased from $8\mu\text{m}$, the increase in the deflection is not significant. Therefore, for the proposed micromirror, the separation gap between the fixed bottom electrode is $8\mu\text{m}$. The dimension of the reflective micromirror surface of the proposed micromirror is $400\mu\text{m}$ by $400\mu\text{m}$, the width of the arm that holds the micromirror is $8\mu\text{m}$, and the separation gap between the fixed bottom electrodes is $8\mu\text{m}$. The air cavity between the parallel plates is one more design parameter that can be changed in order to increase the stroke of the micromirror. The proposed micromirrors are fabricated using the PolyMUMPs fabrication technique, which is explained in Chapter 5.

Traditionally, when MEMS devices are fabricated using the PolyMUMPs fabrication technique, the maximum air cavity between the parallel plates that can be achieved is $2\mu\text{m}$. However, in this thesis, using an unconventional approach, by combining two oxide layers, an air cavity of $2.75\mu\text{m}$ is achieved. Details about the design of the proposed micromirrors and their simulation results are explained in Chapter 4.

4 CHAPTER IV: PROPOSED MICROMIRROR DESIGN

SIMULATION RESULTS

4.1 Introduction

As discussed in Chapter 3, critical design parameters such as the input DC bias voltage, width of the L-shaped arm, and separation gap between the bottom electrodes affect the stroke of the micromirror. In this chapter, four different designs of micromirrors are proposed, investigated, and developed. These four designs are developed by altering the critical design parameters and the air cavity. The proposed micromirrors are designed based on the parallel-plate concept and have a central reflective micromirror surface of $400\mu\text{m}$ by $400\mu\text{m}$ with an L-shaped arm for micromirror actuation. The L-shaped arm is chosen to provide more flexibility for the arms to move upward. In this configuration, the micromirror is supported by four L-shaped arms, which are anchored on all sides. In addition, three fixed bottom electrodes are employed beneath the L-shaped arms on all four sides of the micromirror, to enforce an upward movement in the micromirror instead of the traditional downward deflection.

From Equation 2.2, it can be observed that the stroke of the micromirror is also affected by the height of the air cavity that is formed between the top and bottom actuating plates. This air cavity is the space in which the top micromirror surface moves between the top and bottom actuating plates. Traditionally, when a micromirror is fabricated using the PolyMUMPs fabrication technique, the maximum achievable air cavity between the parallel plates is $2\mu\text{m}$. However, in this thesis and in an unconventional approach, by combining the two oxide layers in the PolyMUMPs fabrication technique, an air cavity of

2.75 μm is achieved. Details about the fabrication technique are discussed in Chapter 5. Therefore, in this chapter, four different designs of micromirrors are presented and are developed by utilizing a variation of these critical design parameters and the air cavity. The physical properties of these designs are explained in Section 4.2. These proposed micromirror designs are then investigated and analyzed using COMSOL Multiphysics software.

4.2 Proposed Micromirror Designs to Enhance Stroke Level

The proposed micromirrors in this work are designed based on the parallel-plate concept where the reflective micromirror surface is deposited over the top actuator plate. Each of these micromirrors is supported by four L-shaped arms, which are anchored on all sides. In addition, three fixed bottom electrodes are employed beneath the L-shaped arms on all four sides of the micromirrors. In all four designs, the width of the L-shaped arm is 8 μm and the separation gap between the fixed bottom electrodes is 8 μm , based on the results obtained in Section 3.4.2.3. These designs employ a different air cavity as well as their unique shape of the bottom electrodes. These four designs are named Design 1, Design 2, Design 3 and Design 4. The physical properties of these designs are explained in Tables II, III, IV, and V, respectively.

In Design 1, the dimension of the reflective micromirror surface is 400 μm by 400 μm . The micromirror is anchored using an L-shaped arm on all four sides of the micromirror. The width and thickness of the L-shaped arm are 8 μm and 1.5 μm , respectively. These four arms are connected to four anchors on all four sides of the micromirror. Each anchor that connects to the L-shaped arm and holds the micromirror is 50 μm in length and 50 μm in width. There are three fixed bottom electrodes beneath each L-shaped arm, which are

separated by an equal distance of $8\mu\text{m}$ from each other. These three fixed bottom electrodes are equal in dimension, i.e., $10\mu\text{m}$ wide, $400\mu\text{m}$ long, and $0.5\mu\text{m}$ thick. For Design 1, the air cavity between the top and bottom electrodes is $2\mu\text{m}$. Figures 4.1(a) and (b) show a top view and a cross-sectional view of Design 1, respectively; they are designed in MEMSPro using the standard PolyMUMPs fabrication layer sequence. Table II illustrates the physical properties of Design 1.

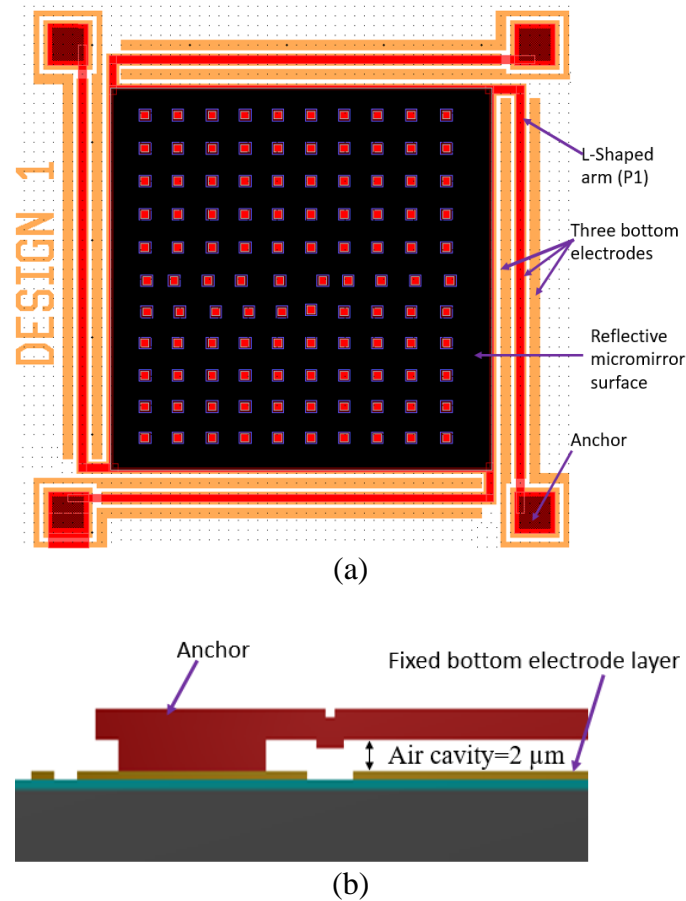


Figure 4.1: (a) Top view of Design 1 in MEMSPro using the PolyMUMPs fabrication process, (b) a cross-sectional view of Design 1 showing an air cavity of $2.0\mu\text{m}$ in MEMSPro.

As discussed earlier in Section 3.2.1, the positioning of the electrode affects the stroke of the micromirror. Therefore, in Design 2, the bottom electrode plate, which is beneath the reflective micromirror surface, is subdivided into four individual electrodes.

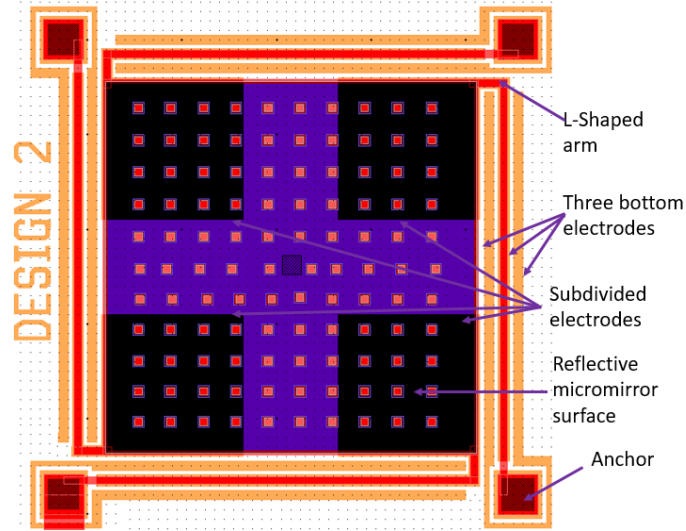
Table II: Physical properties of the micromirror in Design 1 with the air cavity of 2 μ m.

Layer	Length	Width	Height	Separation gap
Micromirror Reflective Surface	400 μ m	400 μ m	0.5 μ m	
Fixed Bottom Electrode	400 μ m	10 μ m	0.5 μ m	8 μ m
L-shaped Arm	400 μ m	8 μ m	2.0 μ m	
Anchor	50 μ m	50 μ m	2.5 μ m	
Air Cavity			2.0 μ m	

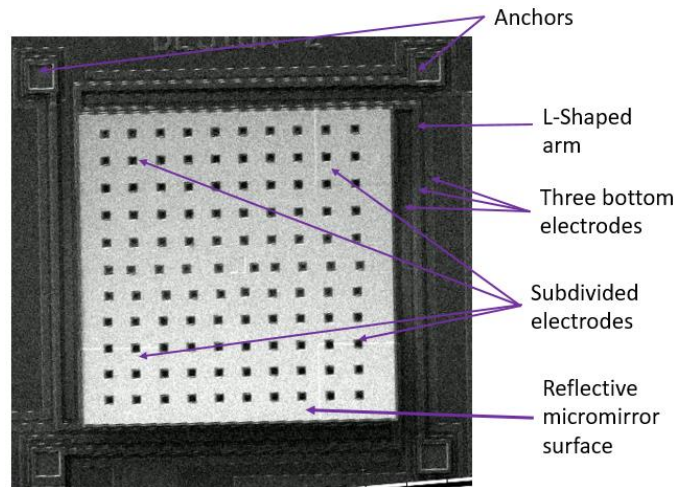
This unique configuration of subdivided electrodes in Design 2 allows the ability to selectively actuate individual subdivided electrodes as this configuration allows the bottom electrode to be biased in different ways. This selective actuation will then allow controlling the movement of different corners of the micromirror. Similar to Design 1, the air cavity for Design 2 is 2 μ m. Evaluation of the COMSOL simulation result of Design 2 is presented in Section 4.3.4 in detail. Table III illustrates the physical properties of Design 2. Figure 4.2(a) illustrates a top view of Design 2 designed in MEMSPro using the standard PolyMUMPs fabrication layer sequence. Figure 4.2(b) shows the Scanning Electron Microscope (SEM) image of Design 2 that is captured using a HITACHI TM3030 plus tabletop microscope.

Table III: Physical properties of the micromirror in Design 2 with the air cavity of 2 μ m.

Layer	Length	Width	Height	Separation gap
Micromirror Reflective Surface	400 μ m	400 μ m	0.5 μ m	
Fixed Bottom Electrode	400 μ m	10 μ m	0.5 μ m	8 μ m
Subdivided Electrodes	150 μ m	150 μ m	0.5 μ m	100 μ m
L-shaped Arm	400 μ m	8 μ m	2.0 μ m	
Anchor	50 μ m	50 μ m	2.5 μ m	
Air Cavity			2.0 μ m	



(a)



(b)

Figure 4.2: (a) Top view of Design 2 with subdivided bottom electrodes designed and fabricated using the PolyMUMPs fabrication process. (b) Scanning Electron Microscope (SEM) image of Design 2 that is captured using a HITACHI TM3030 plus tabletop microscope.

As discussed in Section 4.1, the air cavity affects the stroke of the micromirror. As stated in Equation 2.2, with an increase of the air cavity, the electrostatic force responsible for the movement of the actuating plates decreases, which decreases the stroke level of the micromirror. However, the increased air cavity allows more space for the micromirror surface to move. As a result, the stroke level of the micromirror will increase. One of the major disadvantages of this approach is that the input voltage required to operate the device

will increase. However, for automotive applications, the high input voltage is not identified as a major concern.

Therefore, In Design 3 and Design 4, the air cavity is increased to $2.75\mu\text{m}$ from $2\mu\text{m}$. This is achieved by an unconventional approach, by combining the available two oxide layers and by etching away the second polysilicon layer beneath the micromirror surface in the PolyMUMPs fabrication process. Fabrication steps are discussed in detail in Chapter 5. Figure 4.3(a) illustrates the top view of Design 3 and 4.3(b) illustrates the cross-sectional view of Design 3 with an air cavity of $2.75\mu\text{m}$ designed in MEMSPro using the standard PolyMUMPs fabrication layer sequence. Table IV illustrates the physical properties of Design 3.

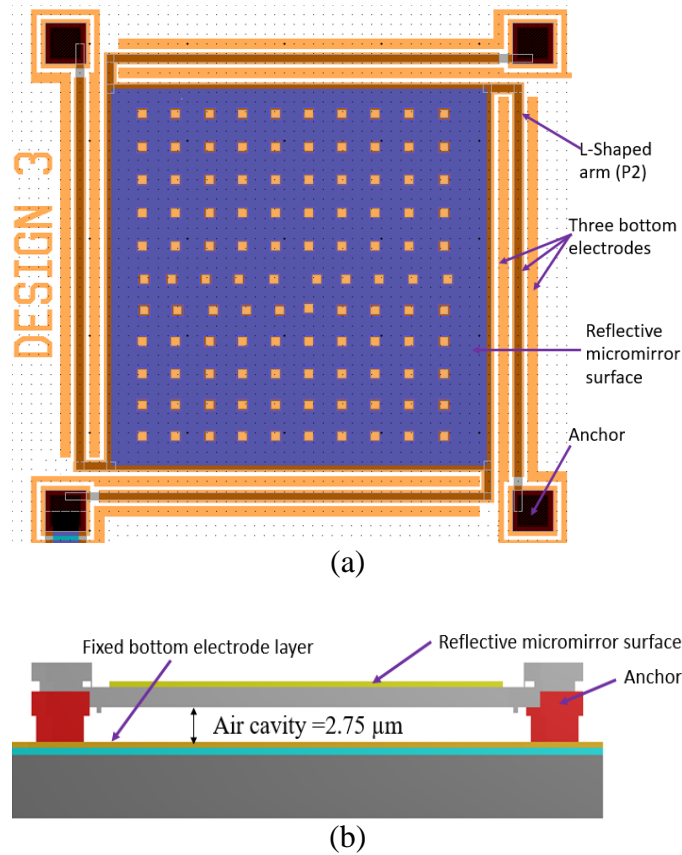


Figure 4.3: (a) Top view and (b) cross-sectional view of Design 3 in MEMSPro, fabricated using the PolyMUMPs fabrication process.

Table IV: Physical properties of the micromirror in Design 3 with the air cavity of 2.75 μm .

Layer	Length	Width	Height	Separation gap
Micromirror Reflective Surface	400 μm	400 μm	0.5 μm	
Fixed Bottom Electrode	400 μm	10 μm	0.5 μm	8 μm
L-shaped Arm	400 μm	8 μm	2.0 μm	
Anchor	50 μm	50 μm	2.5 μm	
Air Cavity			2.75 μm	

Similar to Design 2, in Design 4, the bottom electrode plate, which is directly beneath the reflective micromirror surface is subdivided into four individual electrodes. This is done in an attempt to selectively actuate the electrodes, which provides the ability to control the movement of the micromirror surface better compared to the conventional design. The air cavity, or the distance between the top and bottom actuator plates, is 2.75 μm . Each subdivided electrode is 150 μm wide and 150 μm long, with a thickness of 0.5 μm . These subdivided electrodes are separated by an equal distance of 100 μm . Table V illustrates the physical properties of Design 4. Figure 4.4 illustrates the top view of Design 4 designed in MEMSpro using the standard PolyMUMPs fabrication layer sequence.

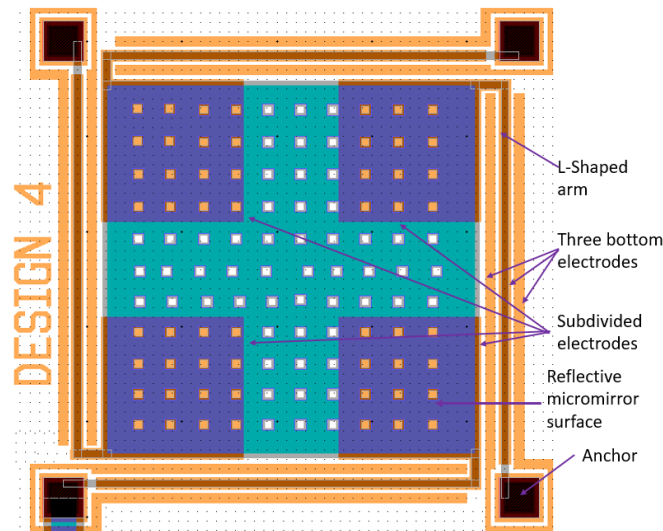


Figure 4.4: Top view of Design 4 micromirror in MEMSpro, developed using the PolyMUMPs fabrication process.

Table V: Physical properties of the micromirror in Design 4 with the air cavity of 2.75 μm .

Layer	Length	Width	Height	Separation gap
Micromirror Reflective Surface	400 μm	400 μm	0.5 μm	
Fixed Bottom Electrode	400 μm	10 μm	0.5 μm	8 μm
Subdivided Electrodes	150 μm	150 μm	0.5 μm	100 μm
L-Shaped Arm	400 μm	8 μm	2.0 μm	
Anchor	50 μm	50 μm	2.5 μm	
Air Cavity			2.75 μm	

4.3 Simulation Results and Design Evaluations

The proposed micromirrors are simulated using the MEMS module in COMSOL Multiphysics software. “Solid Mechanics” and “Electrostatics” studies are the two types of physics that the MEMS module uses to simulate the design. As discussed and investigated in Section 3.3.2, the “finer” mesh is chosen because the stroke becomes independent of the number of elements for meshes denser than “finer”; however, the simulation time increases significantly for meshes denser than “finer”. As the micromirror is anchored on all 4 sides, one end of each arm of the micromirror is fixed. This allows the free arm and micromirror surface to deflect upon actuation. The simulation time for the proposed designs in this thesis ranges between 4 hours and 30 hours, depending on the complexity of the design.

4.3.1 Tilting of Micromirror Surface

As discussed in Section 2.3.1, an electrostatically-actuated microstructure undergoes pull-in instability. Pull-in instability is defined as a phenomenon where when the micromirror is actuated, the micromirror surface moves downward. After reaching 1/3rd of the separation gap between the plates, the electrostatic force pulling the micromirror down becomes higher than the restoring force. As a result, the response of the micromirror

becomes unstable [43], [41] when it reaches $1/3^{\text{rd}}$ of the air cavity. As discussed in Section 2.3.1 and Section 3.3, these proposed micromirrors have three fixed bottom electrodes, which will push the micromirror surface upward rather than the traditional downward movement. When one end of the surface goes up, the other end of the surface goes down, thereby tilting the micromirror surface. However, the amplitude of deflection is not equal on both ends. This downward movement in one end of the micromirror surface again limits the stroke when the downward deflection of the micromirror surface reaches $1/3^{\text{rd}}$ of the air cavity. This upward and downward movement of the micromirror surface is illustrated in Figure 4.5. Details about the downward deflection of all four proposed designs and their effect on their stroke level are explained in Sections 4.3.3 to 4.4.

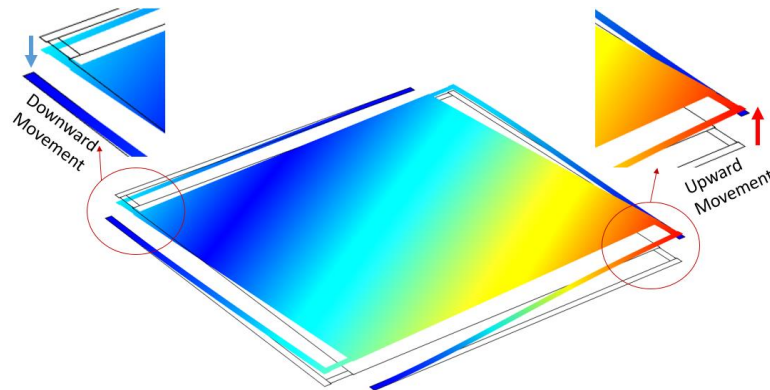


Figure 4.5: COMSOL simulation results of Design 1 showing the tilting of the micromirror surface for an applied bias voltage where one end of the micromirror surface moves upward and the other end deflects downward with an unequal amplitude of deflection.

4.3.2 Effect of Air Domain on the Level of Stroke

As discussed in Section 3.2.1, the electric flux lines that are inside the parallel plates are straight and uniform. However, at the edges, the electric flux lines are bending, as a point charge creates a spherical field [62]. In a parallel plate design, these generated electric flux lines influences the performance of the device. Since the proposed design principle benefits

from the generated fringing fields, the influencing flux lines at the edge of the structure need to be also considered in the simulations.

Therefore, in order to properly include the effect of the fringing fields, the air domain should be considered around the micromirror. The air domain needs to be large enough to contain all the influencing electric flux lines. However, adding a large air domain to the simulation drastically increases the simulation time. As a result, in order to optimize the size of the air domain around the micromirror to yield the maximum stroke, different size of air domain is investigated and analyzed. The stroke of the micromirror should be independent of the air domain around it.

First, the air domain is set equal to the size of micromirror so that it is large enough to contain the micromirror within it. Then, the air domain is enlarged from all the edges. In the proposed micromirror designs, the width of one fixed bottom electrode is $10\mu\text{m}$. Therefore, the size of the air domain is increased from $10\mu\text{m}$ across all the edges of the micromirror. From simulation results, it can be asserted that the stroke of the micromirror increases as the air domain increases. However, the stroke of the micromirror remains unchanged when the air domain is extended more than $50\mu\text{m}$ measured from all the edges. The simulation result is illustrated in Figure 4.6. Based on these findings, for the simulation of the proposed design of the micromirror, the air domain that is surrounding the micromirror extends $50\mu\text{m}$ from all the edges of the micromirror. This air domain is large enough to contain all the electric flux lines. The micromirror with an air cavity that extends $50\mu\text{m}$ from all the edges and is large enough to contain all the electric flux lines is illustrated in Figure 4.7.

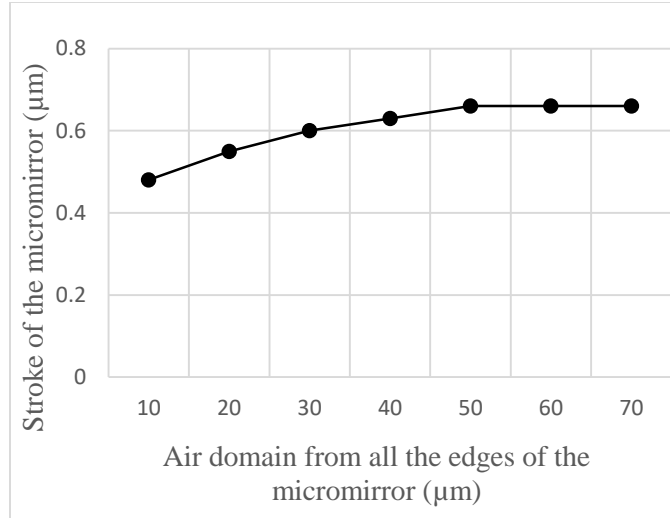


Figure 4.6: COMSOL simulation results presenting the effect of enlarging the outer air domain on the mirror's stroke.

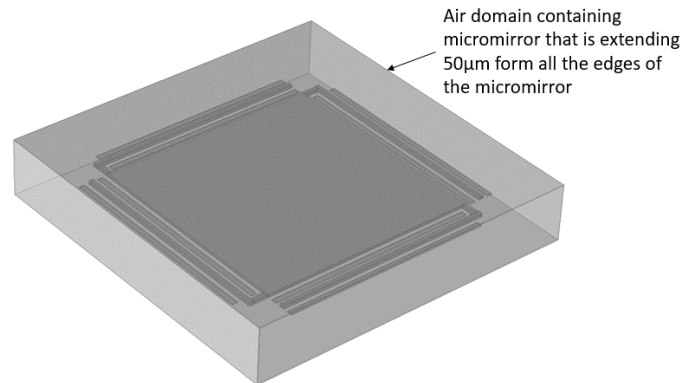


Figure 4.7: Micromirror geometry in COMSOL simulation software with an outer air domain that extends $50\mu\text{m}$ from all of the edges of the micromirror. This air domain is large enough to contain all the electric flux lines.

4.3.3 Micromirror Design 1 Evaluation

When an input DC bias voltage is supplied to the arms of the micromirror, its surface deflects. An input DC bias voltage is applied gradually, increasing from 10V with a step of 10V. For Design 1, gradually increasing the input DC bias voltage from 10V to 100V is performed in order to investigate its performance. The voltage is increased by a step of 10V. This range of input voltage is considered suitable for Design 1 not only because the air cavity is $2.0\mu\text{m}$ but also due to its pull-in voltage, as calculated by Equation 2.6. When

the air cavity is $2.0\mu\text{m}$, as discussed in Section 4.3.1, pull-in instability will limit the downward deflection of the micromirror to $0.6\mu\text{m}$, which is $1/3^{\text{rd}}$ of the air cavity

The stroke of the micromirror increases as the input voltage increases. This study enables the identification of the stroke of the proposed micromirror design and its appropriate operating input voltage range. Figure 4.8 illustrates the COMSOL simulation results presenting the effect of the input voltage on the stroke of the micromirror and Table VI presents the stroke of the micromirror for the corresponding input DC bias voltage.

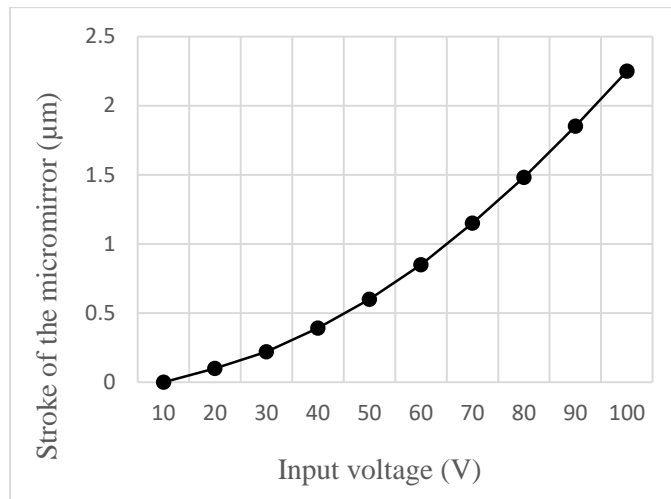


Figure 4.8: COMSOL simulation results presenting the effect of the input voltage on the stroke of the micromirror in Design 1.

Table VI: Level of the stroke and micromirror downward deflection in Design 1 versus input DC bias voltage.

Input DC Bias Voltage (V)	Stroke of the Micromirror (μm)	Maximum downward deflection of the Micromirror Surface (μm)
10	2E-6	0.003
20	0.1	0.02
30	0.22	0.042
40	0.39	0.078
50	0.6	0.12
60	0.85	0.17
70	1.15	0.24
80	1.48	0.3
90	1.85	0.39
100	2.25	0.51

Therefore, as illustrated in Figure 4.8 and as presented in Table VI, for Design 1, the stroke of the micromirror at 100V is 2.25 μ m and the maximum downward deflection is 0.51 μ m. Despite the amplitude of upward deflection and downward deflection not being equal, the uniformity of the micromirror surface is almost linear. Therefore, the micromirror may be unbalanced when operating this design beyond 100V, as the micromirror becomes unstable due to pull-in instability.

4.3.4 Micromirror Design 2 Evaluation

As discussed in Section 4.2, the bottom electrode plate, which is beneath the reflective micromirror surface, is subdivided into four individual electrodes in Design 2. This configuration allows the movement of different corners and sides of the micromirror to be controlled by selectively actuating individual subdivided electrodes. Each subdivided electrode is 150 μ m wide and 150 μ m long, with a thickness of 0.5 μ m. These subdivided electrodes are separated by an equal distance of 100 μ m. Since the bottom electrode is divided into four subdivided electrodes, it can be actuated in different ways. In this section, Design 2 is actuated in two ways. First, input DC bias voltage is applied to the arms and to one subdivided electrode. Second, input DC bias voltage is applied to the arms and two subdivided electrodes. In both cases, simulation results indicate that the stroke of the micromirror increases as the input voltage increases. An input DC bias voltage is applied gradually, increasing from 10V with a step of 10V. Figure 4.9 illustrates the COMSOL simulation results presenting the effect of the input voltage on the stroke of the micromirror and Table VII presents the stroke of the micromirror when input DC bias voltage is applied to one subdivided electrode and two subdivided electrodes.

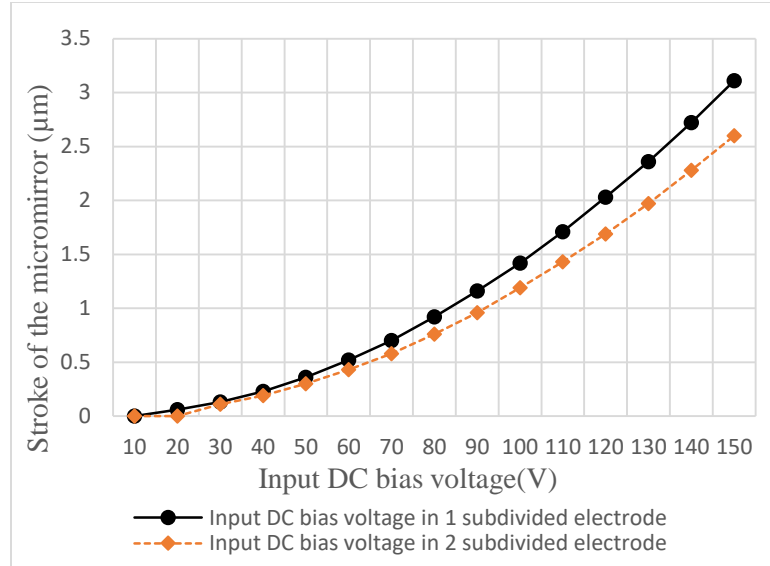


Figure 4.9: COMSOL simulation results presenting the effect of the input voltage on the stroke of the micromirror in Design 2 when an input DC bias voltage is applied to one of the subdivided electrodes as well as when it is applied to two of the subdivided electrodes.

Table VII: Level of the stroke in Design 2 when the input DC bias voltage is applied to one subdivided electrode as well as when it is applied to two subdivided electrodes.

Input DC Bias Voltage (V)	Stroke of Design 2 (µm) when input DC bias is applied to 1 subdivided electrode.	Stroke of Design 2 (µm) when input DC bias is applied to 2 subdivided electrodes.
10	0.00001	0.00001
20	0.06	0.00005
30	0.13	0.11
40	0.23	0.19
50	0.36	0.3
60	0.52	0.43
70	0.7	0.58
80	0.92	0.76
90	1.16	0.96
100	1.42	1.19
110	1.71	1.43
120	2.03	1.69

As discussed in Section 4.3.1, when Design 2 is actuated, one end of the surface goes up and the other surface goes down. Table VIII shows the value of the maximum downward deflection of the micromirror when an input voltage is applied to the micromirror. This study helps to identify the stroke and suitable operating voltage for micromirror Design 2.

Table VIII: Level of the downward deflection in Design 2 when the input DC bias voltage is applied to one subdivided electrode as well as when it is applied to two subdivided electrodes.

Input DC Bias Voltage (V)	Maximum downward deflection of Design 2 (μm) when input DC bias is applied to 1 subdivided electrode.	Maximum downward deflection of Design 2 (μm) when input DC bias is applied to 2 subdivided electrodes.
10	0.005	0.005
20	0.017	0.023
30	0.04	0.051
40	0.071	0.09
50	0.11	0.14
60	0.16	0.2
70	0.21	0.27
80	0.27	0.35
90	0.34	0.42
100	0.42	0.49
110	0.5	0.57
120	0.58	0.67

From Table VIII, it is observed that, for an input voltage of 120V, the maximum downward deflection of the micromirror surface is nearing $1/3^{\text{rd}}$ of the air cavity. Therefore, the appropriate operating voltage for Design 2 is below 120V. Compared to Design 1, the stroke level for Design 2 is less for the same input voltage. As seen from Tables VI and VII, for Design 1 and Design 2, the stroke levels at 100V are $2.25\mu\text{m}$ and $1.42\mu\text{m}$, respectively. From this comparison, the performance of Design 1 is better than Design 2, as the level of stroke is higher for the same input voltage.

4.3.5 Micromirror Design 3 Evaluation

As discussed in Section 4.2, in Design 3, the air cavity is increased from $2.0\mu\text{m}$ to $2.75\mu\text{m}$. This is achieved by an unconventional approach by combining the two oxide layers of the PolyMUMPs fabrication process. The air cavity has been increased from $2.0\mu\text{m}$ to $2.75\mu\text{m}$ because the increased air cavity provides more space for the micromirror surface to move. An increase in the air cavity also increases the distance of $1/3^{\text{rd}}$ of the air activity, as pull-

in instability occurs at $1/3^{\text{rd}}$ of this distance. Therefore, the stroke of the micromirror can increase when the air cavity increases. However, this also increases the operating voltage of the device.

When an input DC bias voltage is supplied to the arms of the micromirror, its stroke increases. Figure 4.10 shows the effect of the input voltage on the stroke of the micromirror in Design 3. Table IX shows the value of stroke and maximum downward deflection of Design 3 for the input DC bias voltage.

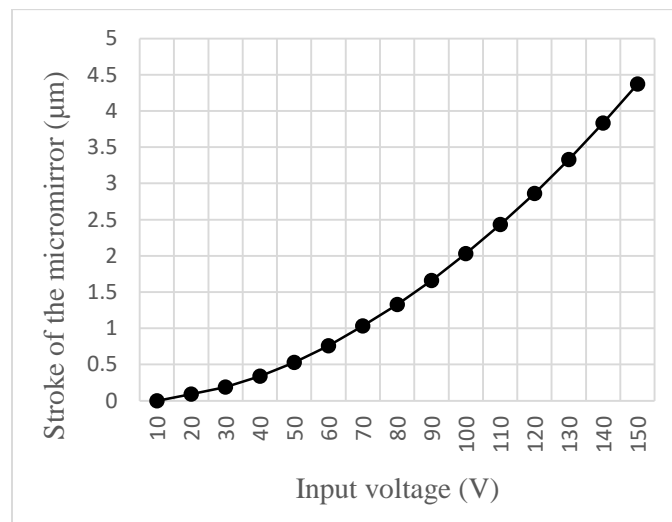


Figure 4.10: COMSOL simulation results presenting the effect of the input voltage on the stroke of the micromirror in Design 3.

Therefore, as illustrated in Figure 4.10 and as presented in Table IX, for Design 3, the maximum upward deflection and the maximum downward deflection of the micromirror at 150V are $4.37\mu\text{m}$ and $0.9\mu\text{m}$, respectively. For Design 3, the air cavity is $2.75\mu\text{m}$, therefore, pull-in instability will limit the maximum downward deflection to $0.9\mu\text{m}$, which is $1/3^{\text{rd}}$ of the air cavity. Thus, the maximum bias voltage will be 150V, as the micromirror becomes unstable after this point due to pull-in instability. Compared to Design 1 and Design 2, Design 3 yields the maximum stroke.

Table IX: Levels of stroke and downward deflection in Design 3 versus the input DC bias voltage.

Input DC Bias Voltage (V)	Stroke of the Micromirror (μm)	Maximum downward deflection of the Micromirror Surface (μm)
10	2E-6	0.004
20	0.09	0.02
30	0.19	0.044
40	0.34	0.08
50	0.53	0.14
60	0.76	0.18
70	1.03	0.25
80	1.33	0.33
90	1.66	0.4
100	2.03	0.49
110	2.43	0.59
120	2.86	0.62
130	3.33	0.78
140	3.83	0.84
150	4.37	0.9

4.3.6 Micromirror Design 4 Evaluation

Similar to Design 2, the bottom electrode of Design 4 is divided into four subdivided electrodes. Therefore, the bottom electrode can be actuated in different ways. In this section, Design 4 is actuated in two ways. First, input DC bias voltage is applied to the arms and to one subdivided electrode. Second, input DC bias voltage is applied to the arms and two subdivided electrodes. In both cases, the stroke of the micromirror increases with increasing input voltage. The input DC bias voltage is applied gradually, increasing from 10V with a step of 10V. Figure 4.11 illustrates the COMSOL simulation results presenting the effect of the input voltage on the stroke of Design 4. Table X tabulates the input voltage and the corresponding stroke for Design 4. Similar to Design 3, for Design 4, the air cavity is also $2.75\mu\text{m}$, therefore, pull-in instability will limit the maximum downward deflection

to $0.9\mu\text{m}$, which is $1/3^{\text{rd}}$ of the air cavity. Table XI presents the maximum downward deflection for the corresponding input voltage.

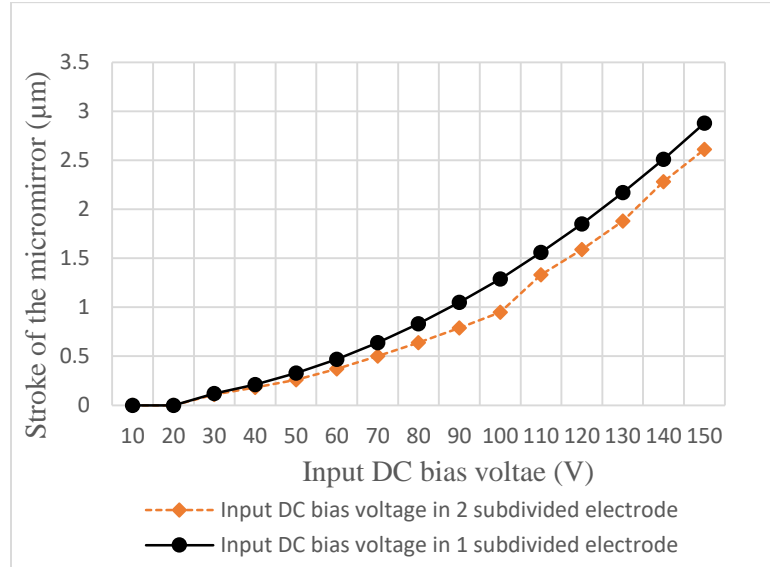


Figure 4.11: COMSOL simulation results presenting the effect of the input voltage on the stroke of the micromirror in Design 4 when an input DC bias voltage is applied to one of the subdivided electrodes as well as when it is applied to two of the subdivided electrodes.

Table X: Level of stroke in Design 4 when the input DC bias voltage is applied to one subdivided electrode as well as when it is applied to two subdivided electrodes.

Input DC Bias Voltage (V)	Stroke of Design 4 (μm) when input DC bias is applied to 1 subdivided electrode.	Stroke of Design 4 (μm) when input DC bias is applied to 2 subdivided electrodes.
10	0.00001	0.00001
20	0.00005	0.00006
30	0.12	0.11
40	0.21	0.18
50	0.33	0.26
60	0.47	0.37
70	0.64	0.5
80	0.83	0.64
90	1.05	0.79
100	1.29	0.95
110	1.56	1.33
120	1.85	1.59
130	2.17	1.88
140	2.51	2.28
150	2.88	2.61

Table XI: Level of the downward deflection in Design 4 when the input DC bias voltage is applied to one subdivided electrode as well as when it is applied to two subdivided electrodes.

Input DC Bias Voltage (V)	Maximum downward deflection of Design 4 (μm) when input DC bias is applied to 1 subdivided electrode.	Maximum downward deflection of Design 4 (μm) when input DC bias is applied to 2 subdivided electrodes.
10	0.004	0.004
20	0.015	0.014
30	0.035	0.031
40	0.062	0.055
50	0.1	0.08
60	0.14	0.12
70	0.19	0.17
80	0.24	0.22
90	0.3	0.27
100	0.37	0.34
110	0.45	0.4
120	0.52	0.47
130	0.61	0.54
140	0.7	0.62
150	0.8	0.7

From Table XI, it can be seen that the maximum downward deflection of Design 4 is $0.9\mu\text{m}$ at 150V. Therefore, the maximum operating voltage in Design 4 is 150V, as the micromirror becomes unstable above this point due to the pull-in instability. When compared to Design 3, the stroke level for Design 4 is lower than Design 3, however, it is higher than Design 1 and 2 for the same input voltage. As seen from Table IX and X, the stroke levels at 150V for Design 3 and Design 4 are $4.37\mu\text{m}$ and $2.88\mu\text{m}$, respectively. Furthermore, it is also important to analyze the uniformity of the micromirror surface in order to identify that the micromirror surface is tilting and there is no bending of the micromirror surface. This study will also allow measuring the effective stroke of the micromirror surface measuring it from one end of the micromirror surface that is deflecting downward to the other end that is deflecting upward. It is discussed in Section 4.4.

4.4 Design Comparison and Conclusion

In this chapter, four different designs of a micromirror are presented and developed. These four designs are named Design 1, Design 2, Design 3 and Design 4. All proposed micromirrors are a parallel-plate design with a central reflective micromirror surface of $400\mu\text{m}$ by $400\mu\text{m}$ and an L-shaped arm. In this configuration, the micromirror is supported by four L-shaped arms, which are anchored on all sides of the micromirror. In addition, three fixed bottom electrodes are employed beneath the L-shaped arms on all four sides of the micromirror to enforce an upward movement instead of traditional downward deflection. Across all four designs, the width of the L-shaped arm is $8\mu\text{m}$ and the separation gap between the fixed bottom electrodes is $8\mu\text{m}$. However, the air cavity and the design configuration of the bottom electrodes are different amongst the designs.

In Design 1, the air cavity between the top and bottom electrodes is $2\mu\text{m}$. In Design 2, the bottom electrode plate, which is beneath the reflective micromirror surface, is subdivided into four individual electrodes. This configuration allows the movement of different corners and sides of the micromirror to be controlled by selectively actuating individual subdivided electrodes. In Design 3 and Design 4, the air cavity is $2.75\mu\text{m}$. This is achieved by an unconventional approach, by combining two oxide layers. Fabrication steps are discussed in Chapter 5. In Design 4, the actuating electrode plate, which is directly beneath the reflective micromirror surface, is subdivided into four individual electrodes.

As discussed in Section 4.3.1, the electric flux lines bend at the edge of the parallel plates. This is called the fringing field effect. Electrostatically-actuated microstructures benefit from the fringing field. Similarly, the proposed micromirror design principle relies

on the generated fringing fields and the flux lines at the edge need to be considered in the simulations. Therefore, an air domain around the micromirror should be large enough to contain all the influencing electric flux lines. Ensuring that all the influencing electric flux lines are contained inside the air domain eliminates the dependency of the simulation results on the number of simulated elements and mesh density. Therefore, from the simulation results presented in Section 4.3.2, the air domain surrounding the micromirror extends 50 μm from all the edges of the micromirror. This air domain is large enough to contain all the influencing electric flux lines.

COMSOL simulation results are analyzed to identify the performance of each proposed micromirror design. It is important to consider and investigate both upward as well as the downward deflection of the micromirror surface because, as discussed earlier, downward deflection of the micromirror surface will limit the stroke level. Figure 4.12 illustrates the COMSOL simulation results presenting the effect of the input voltage on the stroke of all four designs of the micromirror.

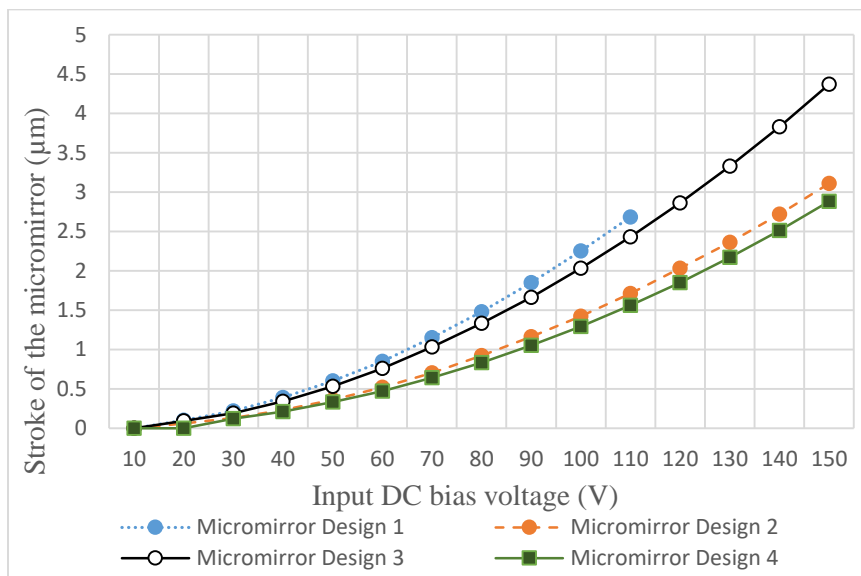


Figure 4.12: COMSOL simulation results comparing the effect of the input voltage on the stroke of all four proposed micromirror designs.

For Design 1, the stroke of the micromirror at 100V is 2.25 μm and the maximum downward deflection is 0.51 μm . Therefore, the maximum operating voltage for this design is 100V as beyond this point the micromirror becomes unstable due to pull-in instability. For Design 2, an out-of-plane stroke of 2.03 μm and maximum downward deflection of 0.58 μm is achieved when an input DC bias voltage of 120V is applied to one subdivided electrode whereas an out-of-plane stroke of 1.69 μm and maximum downward deflection of 0.67 μm are achieved when an input DC bias voltage of 120V is applied to two subdivided electrodes. For Design 3, the stroke of the micromirror at 150V is significantly enhanced and reaches a maximum of 4.37 μm with an acceptable maximum downward deflection of 0.9 μm . For Design 4, an out-of-plane stroke of 2.88 μm and maximum downward deflection of 0.8 μm is achieved when an input DC bias voltage of 150V is applied to one subdivided electrode whereas an out-of-plane stroke of 2.61 μm and maximum downward deflection of 0.7 μm are achieved when an input DC bias voltage of 150V is applied to two subdivided electrodes.

Furthermore, it is important to identify the uniformity of the micromirror surface upon deflection. It is important to make sure that the micromirror surface tilts rather than buckles or bends. The uniformity of the micromirror surface is identified by investigating the amplitude of the deflection level along the diagonal cut-line on the micromirror surface, as shown in Figure 4.13. This study also helps to identify the total effective stroke of the micromirror when measuring from one end of the micromirror surface that deflects down to the other end that deflects upward. Figure 4.14 shows the tilting surface plane of the surface of Design 1 at 100V.

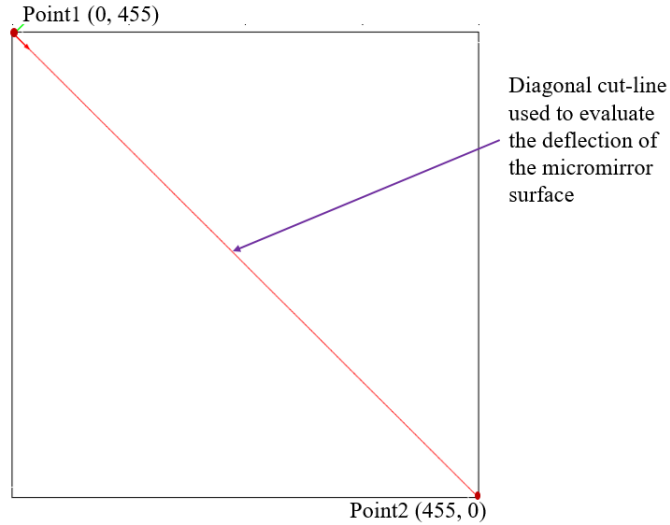


Figure 4.13: Top view of the surface of Design 1 with a diagonal cut line from point1(0,455) to point2(455,0). The amplitude of the deflection level along this cut-line shows the uniformity of the micromirror surface, which is illustrated in Figures 4.15 and 4.16.

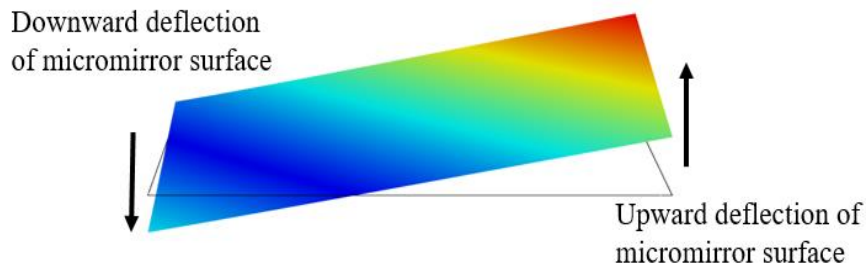


Figure 4.14: Schematic view of COMSOL simulation result, scaled up 25 times, showing the tilting of the micromirror surface of Design 1. When one arm is actuated at 100V, one end of the micromirror surface moves upward and the other end deflects downward, however, the amplitude of level of deflection is not equal.

As discussed in Section 4.3, the downward deflection of the micromirror surface limits the performance and stroke level of the micromirror. When a micromirror is actuated, one end of the micromirror surface moves upward but the other end moves downward. The amplitude of the level of deflection is not equal in both ends, which may generate non-uniformity in the micromirror surface. Therefore, in order to investigate the uniformity of the micromirror surface across all four micromirror designs, the deflection curve along the diagonal cut-line is plotted, as shown in Figure 4.15 and 4.16.

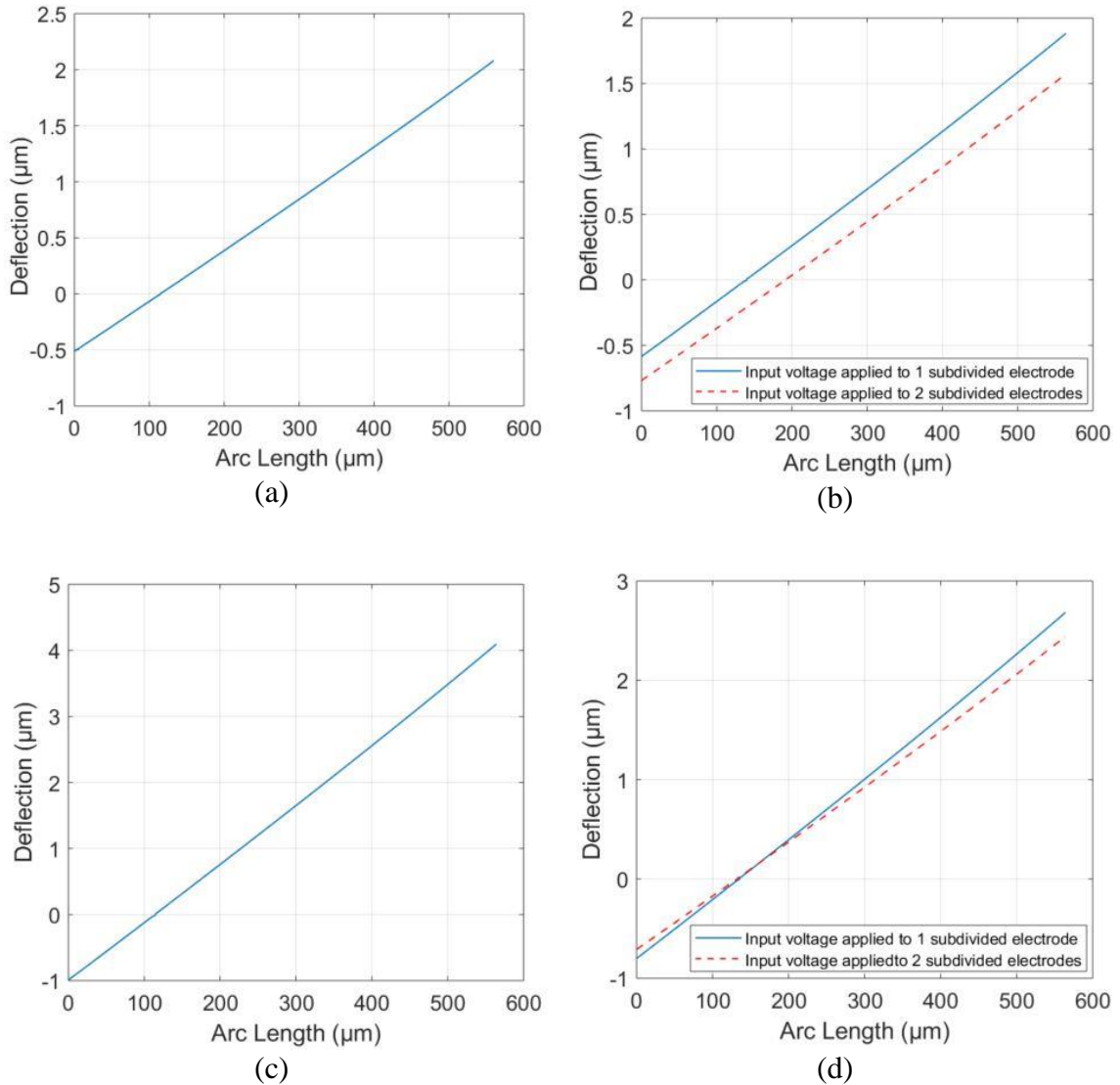


Figure 4.15: COMSOL simulation results showing the deflection of the micromirror surface along the diagonal cut-line for (a) Design 1 at 100V (b) Design 2 at 120V (c) Design 3 at 150V (d) Design 4 at 150V. These results show that the micromirror surface is tilting and there is no bending.

It can be observed from Figure 4.15 and 4.16, that the deflection of the micromirror surface is uniform for all four proposed designs. When the micromirror is actuated within a suitable operating voltage range, the surface tilts without buckling or distorting the surface. The maximum downward deflection of the micromirror occurs at Point1 (0,455) and the maximum upward deflection occurs at Point2 (455,0). These points lie at the two ends of the diagonal cut-line, as shown in Figure 4.13. The maximum downward and the maximum

upward movement for all four proposed micromirror designs and their biasing condition is shown in Table XII.

Table XII: Table illustrating maximum downward and upward deflection for all four proposed micromirror designs and their biasing conditions.

Micromirror Design and Biasing Condition	Maximum Downward Deflection (μm)	Maximum Upward Deflection (μm)
Design 1 at 100V	0.51	2.09
Design 2 at 120V, when an input voltage is applied to 1 subdivided electrode	0.58	1.88
Design 2 at 120V, when an input voltage is applied to 2 subdivided electrodes	0.76	1.57
Design 3 at 150V	0.98	4.09
Design 4 at 150V, when an input voltage is applied to 1 subdivided electrode	0.8	2.67
Design 4 at 150V, when an input voltage is applied to 2 subdivided electrodes	0.7	2.42

From Figure 4.15 and Table XII, the total level of deflection measured from the end that moves down to the end that is pushed upward can be calculated. For Design 1, at 100V, the maximum downward deflection is $0.51\mu\text{m}$ and the maximum upward deflection is $2.09\mu\text{m}$. Therefore, the total deflection from one end to the other is $2.60\mu\text{m}$. Similarly, for Design 2, at 120V, the total amount of deflection measured from one end to the other is $2.46\mu\text{m}$ when an input voltage is applied to one subdivided electrode and $2.33\mu\text{m}$ when an input voltage is applied to two subdivided electrodes. Likewise, for Design 3, at 150V, the total downward deflection is measured to be $5.07\mu\text{m}$. For Design 4, at 150V, the total amount of deflection from one end to the other is $3.47\mu\text{m}$ when an input voltage is applied to one subdivided electrode and $2.49\mu\text{m}$ when an input voltage is applied to two subdivided electrodes.

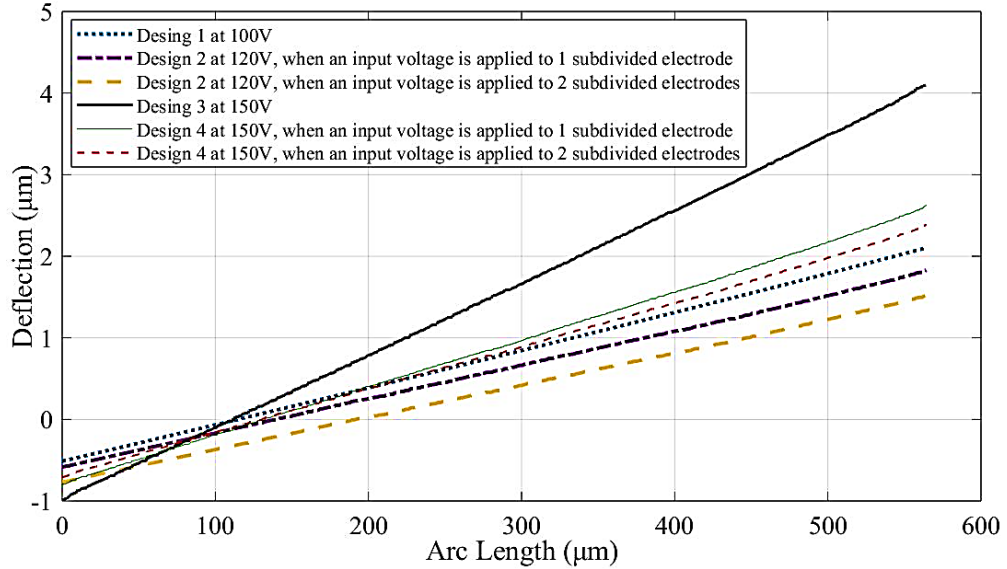


Figure 4.16: COMSOL simulation results showing the deflection of the micromirror surface along the diagonal cut-line for all four proposed micromirror designs. This illustrates that the micromirror surface is tilting and there is no bending. The negative deflection is for downward deflection whereas the positive deflection represents upward movement.

Therefore, by comparing Designs 3 and 4 with Designs 1 and 2, it can be observed that by increasing the cavity height of the micromirror by combining the two available sacrificial layers in the PolyMUMPs fabrication process, a significantly larger level of stroke is achieved. This study identifies the performance as well as the maximum operating voltage for each design. From the simulation results presented in Section 4.3 and from the comparison shown in Table XII, it is observed that out of the four proposed micromirror designs, Design 3 yields the maximum stroke, which is $4.37\mu\text{m}$ at 150V. Furthermore, the total amount of deflection measured from one end of the micromirror surface to the other is $5.07\mu\text{m}$. One of the main disadvantages of Design 3 is that it increases the input operating voltage; however, the operating voltage is not identified as a limiting factor for LIDAR systems used in autonomous vehicles. Details about the fabrication of the micromirror are explained in Chapter 5.

5 CHAPTER V: FABRICATION OF PROPOSED MICROMIRROR

5.1 Introduction

Advanced micromachining fabrication technology can be employed to develop the proposed micromirrors. In this work, the designed and investigated micromirrors are fabricated using the PolyMUMPs fabrication technique from MEMSCAP [63]. This surface micromachining fabrication technique is utilized as it provides a cost-effective proof-of-concept to fabricate the proposed MEMS devices explored in this research. In this chapter, details of the PolyMUMPs fabrication techniques are provided and the designed micromirror process steps are discussed in detail.

5.2 PolyMUMPs Fabrication Technique

PolyMUMPs [64] is one of the standard fabrication processes that are offered by MEMSCAP [63]. It is a Multi-User MEMS Process (MUMPs) commercial program that provides cost-effective proof-of-concept to fabricate MEMS devices. PolyMUMPs is a three-layered polysilicon surface micromachining process. In the PolyMUMPs fabrication technique, polysilicon layers are used as the structural materials and the sacrificial layers are deposited silicon oxide layers. However, a disadvantage of this fabrication technique is that the fabrication process cannot be customized, as it is designed to be capable of supporting several different designs on a single silicon wafer. Therefore, the thicknesses of the structural and sacrificial layers are fixed and the structural material properties cannot be altered.

The PolyMUMPs fabrication process includes 7 mask layers with a predefined layer sequence where each layer has a fixed thickness and material properties. The first layer in

the PolyMUMPs fabrication technique is a silicon nitride insulating layer that is deposited over the silicon substrate. The second layer is the first polysilicon (P0) layer with a thickness of 2.0 μm . It is followed by the deposition of the first oxide layer (O1). The thickness of the first oxide layer (O1) is 2 μm . The fourth layer is the second polysilicon layer (P1) and the fifth layer is the second oxide layer (O2). The thicknesses of P1 and O2 are 2 μm and 0.75 μm , respectively. The sixth layer is the third polysilicon layer (P2) followed by a layer of gold metal. The thicknesses of P2 and the metal layers are 1.5 μm and 0.5 μm , respectively. As discussed previously, in this thesis, a micromirror air cavity of 2.75 μm is achieved through combining the two available oxide sacrificial layers, O1 and O2. The physical properties of each fabrication layer sequence are presented in Table XII.

Table XIII: Microfabrication process sequence and layers' thicknesses in the PolyMUMPs fabrication technique.

Layer Name	Thickness (μm)
Nitride	0.6
P0	0.5
O1	2.0
P1	2.0
O2	0.75
P2	1.5
Metal	0.5

As discussed in Section 4.2, four different designs of micromirrors are proposed: Design 1, Design 2, Design 3 and Design 4. For a fair comparison, the air cavity of Design 1 and Design 2 is kept constant and equal to 2.0 μm . However, in Design 3 and Design 4, in order to enhance and optimize the performance of the micromirror, the P1 layer is patterned and etched away from everywhere except the anchors. As discussed in Section 3.3 and as shown in Figures 5.7 and 5.8, the anchor is a supporting post that is connected to the arm and holds of the micromirror. There are four arms in the proposed micromirror design and

they are connected to four anchors. In this thesis, the two oxide layers are combined to achieve an air cavity of $2.75\mu\text{m}$. This increase in the air cavity height provides more space for the micromirror surface to deflect, which allows the stroke of the micromirror to increase. The fabrication steps the four designed and developed micromirrors are explained in Section 5.3.

5.3 Fabrication Steps of the Proposed Micromirrors

The fabrication process starts with a heavily doped 150mm diameter n-type (100) silicon wafer with 1-2 $\Omega\text{-cm}$ resistivity. The surface of the silicon wafer is heavily doped using phosphorous in a standard diffusion furnace using a sacrificial layer of phosphosilicate glass (PSG). The phosphosilicate glass layer in the diffusion furnace is used as a source of dopant. The surface of the wafer is doped to prevent the feedthrough of charge from the substrate to the micromirror surface. Next, the silicon nitride layer is deposited on the wafer as an electrical isolation layer. The insulating layer of silicon nitride, which is $0.6\mu\text{m}$ thick, is deposited using a low-pressure chemical vapor deposition (LPCVD) technique. The deposition of silicon nitride is illustrated in Figure 5.1.

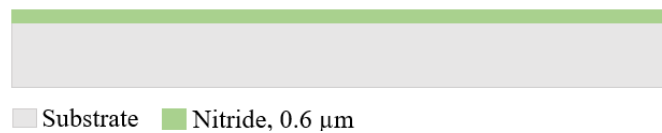


Figure 5.1: Deposition of a $0.6\mu\text{m}$ -thick silicon nitride layer for electrical isolation using a low-pressure chemical vapor deposition (LPCVD) technique.

Next, a layer of $0.5\mu\text{m}$ -thick LPCVD polysilicon film is directly deposited on the silicon nitride. This is the first layer of polysilicon (P0) that is then doped using the PSG layer followed by an annealing process to achieve the desired conductivity level. This is illustrated in Figure 5.2.

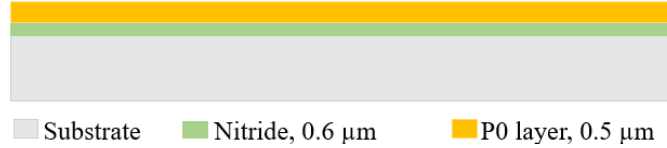


Figure 5.2: Deposition of the first 0.5 μm-thick polysilicon layer (P0) directly on the nitride layer using a low-pressure chemical vapor deposition (LPCVD) technique.

The P0 layer is used as a fixed bottom electrode in the proposed micromirror designs in this thesis. P0 is then patterned using the photolithography technique. Photolithography is the process of transferring geometric shapes from a mask to a photo resistive layer by exposing it to a UV light source. Exposure of the photoresist layer to UV light creates an etch for subsequent pattern transfer to the layer beneath it. The mask is placed between the photoresist coating and UV light source. Etch masks used in fabrication processes and their purpose is listed in Table XIII.

Table XIV: Employed mask layers and their purposes in the PolyMUMPs fabrication technique.

Mask layer name	Purpose of the mask layer
POLY0	Patterns P0 layer
ANCHOR1	Provides opening for P1 to nitride layer or P0 layer connection
DIMPLE	Creates bushing or dimples for the P1 layer
POLY1	Patterns P1 layer
POLY1_POLY2_VIA	Provides opening for P1 to P2 connection
ANCHOR2	Provides opening for P2 to nitride layer or P0 layer connection
POLY2	Patterns P2 layer
METAL	Patterns the metal layer
HOLE0	Creates a hole for P0 layer
HOLE1	Creates release hole for P1 layer
HOLE2	Creates release hole for P2 layer
HOLEM	Creates release hole for the metal layer

As discussed earlier, the mask layer is used to transfer the pattern to the subsequent layer. POLY1 is the mask used to pattern the P0 layer. After patterning the photoresist, the P0 layer is then etched away in the plasma etch system. Etching of the P0 layer after patterning the photoresist is illustrated in Figure 5.3.



Substrate Nitride, 0.6 μm P0 layer, 0.5 μm

Figure 5.3: Etching away the P0 layer after patterning the photoresist in the plasma etch system.

As discussed in Section 4.2, in Design 2 and Design 4, the central bottom electrode, which is below the micromirror surface is subdivided into four individual electrodes. Figure 5.4(a) illustrates the top view of the bottom electrodes for Design 1 and Design 3. Figure 5.4(b) illustrates the top view of the bottom electrodes for Design 2 and Design 4, showing the subdivided electrodes.

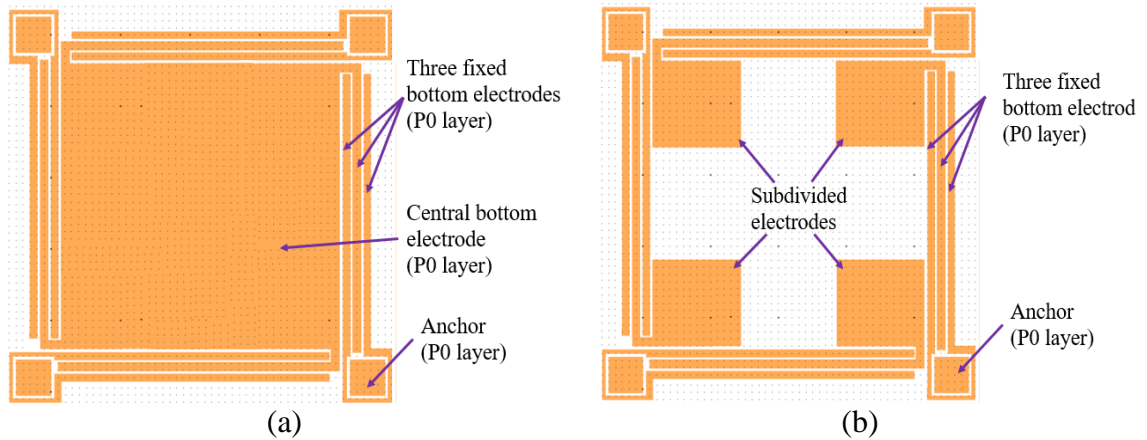
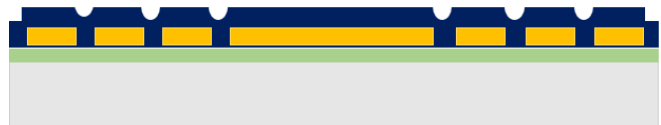


Figure 5.4: (a) top view of the P0 layer of Design 1 and Design 3, (b) top view of the P0 layer of Design 2 and Design 4 in MEMSPro fabricated using the PolyMUMPs fabrication process. Designs 1 and 3 include one central bottom electrode and Designs 2 and 4 each contains four subdivided bottom electrodes.

Then, the first oxide sacrificial layer of phosphosilicate glass (PSG) is deposited over P0. This deposition is performed by LPCVD and annealed in an Argon chamber at a temperature of 1500°C for an hour. The thickness of the first oxide layer (O1) is 2μm. The deposition step of O1 is illustrated in Figure 5.5.



Substrate Nitride, 0.6 μm P0 layer, 0.5 μm O1 layer, 2.0 μm

Figure 5.5: Deposition of the first 2.0μm thick oxide layer (O1) using low-pressure chemical vapor deposition (LPCVD) technique. O1 is the first sacrificial layer.

DIMPLE mask is used to pattern the sacrificial layer lithographically using Reactive Ion Etching (RIE). Reactive ion etching (RIE) is an etching technology where chemically reactive plasma is used to etch away the material deposited on the wafers. The O1 layer is removed at the end of the process, which frees the first structural layer of polysilicon. The O1 layer provides the air cavity between the micromirror plates. The wafer is then patterned using a third mask layer, ANCHOR1, and reactive ion etching is performed. This step is performed in order to provide an opening for the P1 layer to the P0 layer. After etching ANCHOR1, the second layer of polysilicon (P1) is deposited. The thickness of the P1 layer is 2.0 μm . Figure 5.6 illustrates the deposition of the second polysilicon layer (P1) using a low-pressure chemical vapor deposition (LPCVD) technique.

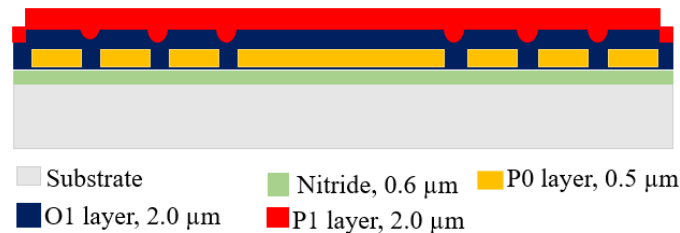


Figure 5.6: Deposition of the 2.0 μm thick second polysilicon layer (P1) using a low-pressure chemical vapor deposition (LPCVD) technique. P1 is then annealed at 1500 $^{\circ}\text{C}$ for an hour in an Argon chamber.

In Design 1 and Design 2, the air cavity is 2.0 μm ; however, in Design 3 and Design 4, the air cavity is 2.75 μm . This is achieved by combining the O1 and O2 layers. The thickness of O1 is 2.0 μm and O2 is 0.75 μm . In order to increase the air cavity, the P1 layer beneath the micromirror surface is etched away such that the layer of O1 and O2 are combined. As a result, the air cavity is increased from 2.0 μm to 2.75 μm in Design 3 and Design 4. Figure 5.7(b) illustrates the fabrication process whereby the P1 layer is etched away from all the areas except the anchors, which increases the air cavity. Figure 5.8(b) shows the top view of the micromirror, which illustrates that the P1 layer is deposited only at the anchor and is etched away from all the other areas.

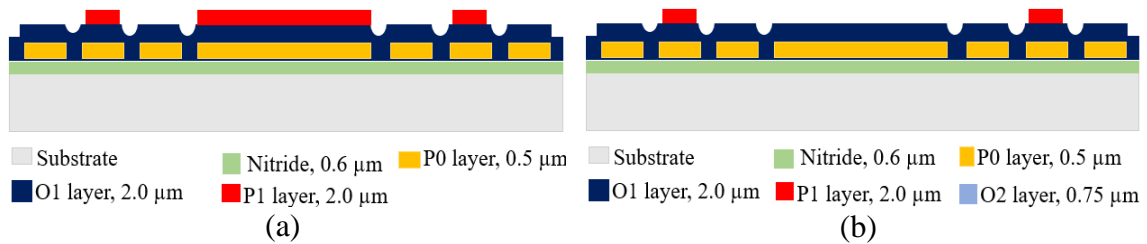


Figure 5.7: Etching away the P1 layer after patterning the photoresist in the plasma etch system for (a) Design 1 and Design 2, and (b) Design 3 and Design 4.

After depositing the P1 layer, the P1 layer along with the phosphosilicate layer is patterned lithographically using the POLY1 mask. After the pattern is transferred to the P1 layer, it is etched away, the photoresist is then stripped and the remaining mask is also removed by RIE.

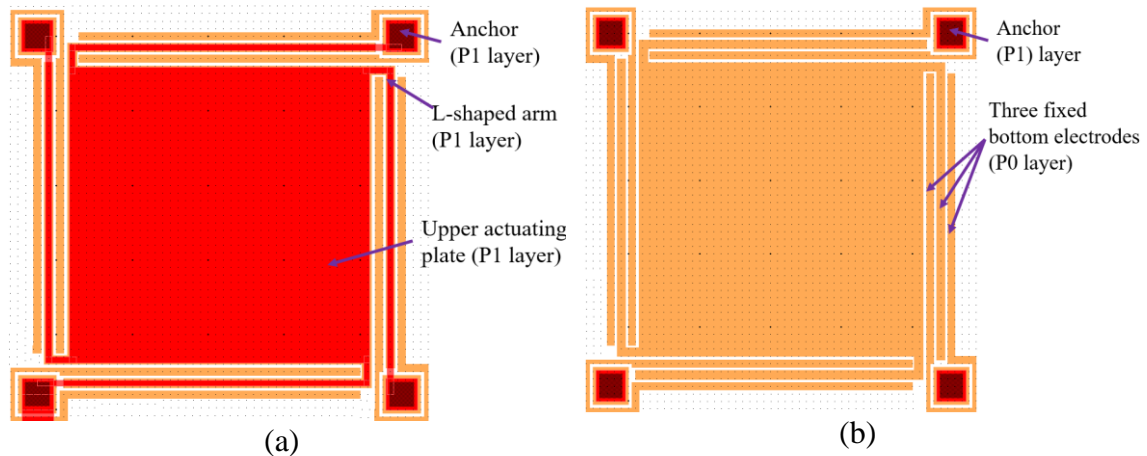


Figure 5.8: (a) top view of the micromirror showing P1 as the top actuating layer in Design 1 and Design 3, and (b) top view of the micromirror showing the P1 layer is deposited only at the anchor and is etched away from all the other areas in Design 2 and Design 4 in MEMSPRO using a standard PolyMUMPs fabrication layer sequence.

After etching the P1 layer, a second oxide layer (O2) is deposited and annealed. The thickness of the O2 layer is $0.75\mu\text{m}$. The wafer is annealed at 1050°C for an hour. This annealing process dopes the polysilicon with phosphorous and also reduces the net stress in the P1 layer. Figure 5.9 illustrates the deposition of the second oxide layer (O2). The O2 layer is then etched with an etch mask called POLY1_POLY2_VIA. This etch mask provides the opening between O2 and P1 and a mechanical and electrical connection

between P1 and the third polysilicon layer (P2). O2 is also patterned using an ANCHOR2 etch mask. The ANCHOR2 etch mask provides an opening for P2 to the P0 layer. Etch masks POLY1_POLY2_VIA and ANCHOR2 are lithographically patterned and etched by RIE.

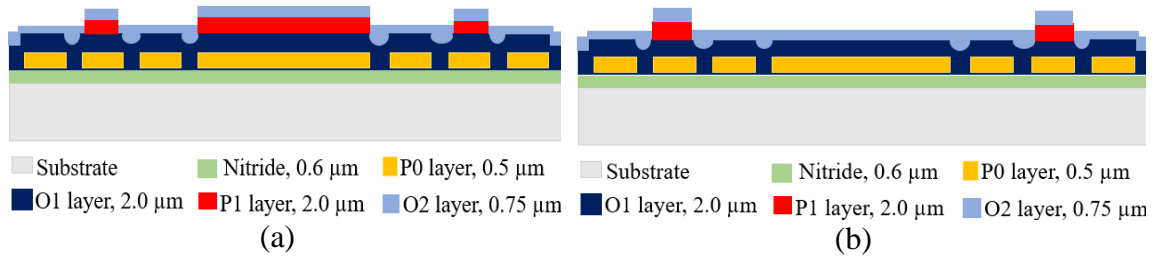


Figure 5.9: Deposition of the 0.75µm-thick second oxide layer (O2) for (a) Design 1 and Design 2, and (b) Design 3 and Design 4. The wafer is then annealed at 1050°C for an hour.

As in Design 3 and Design 4, the connection between P1 and P2 is only at the anchors. Therefore, the POLY1_POLY2_VIA mask is used to provide an opening for P1 and P2 only at the anchors. Figure 5.10 shows the etching of the O2 layer after patterning the photoresist in the plasma etch system for (a) Design 1 and Design 2, and (b) Design 3 and Design 4 of the proposed micromirror.

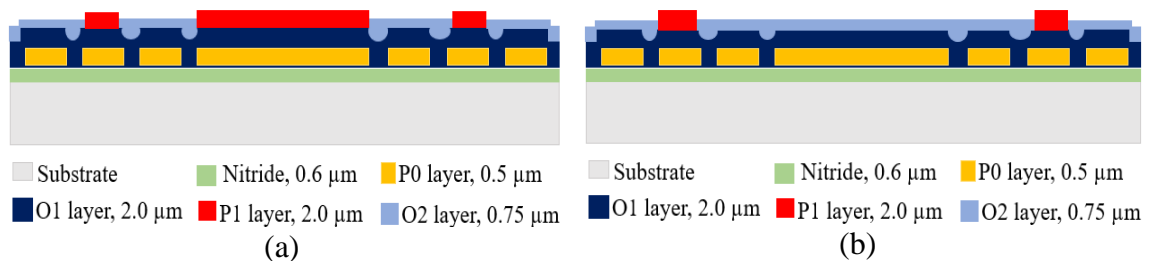


Figure 5.10: Etching away the O2 layer after patterning the photoresist in the plasma etch system for (a) Design 1 and Design 2, and (b) Design 3 and Design 4.

Then, another structural layer of polysilicon, the third polysilicon layer (P2) is deposited, which is followed by the disposition of a 0.2 µm-thick PSG layer. This PSG layer acts as both a dopant source as well as an etching mask for P2. In order to dope the polysilicon, the wafer is annealed for an hour at 1050°C. The P2 layer is lithographically patterned using a POLY2 mask. The PSG layer and the P2 layer are then etched by plasma RIE.

Then, the photoresist is stripped and the masking oxide is also removed. The deposition and etching of the P2 layer are illustrated in Figures 5.11 and 5.12.

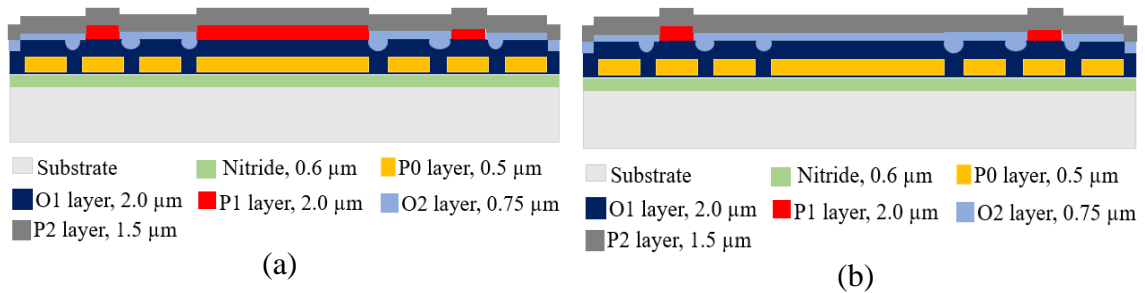


Figure 5.11: Deposition of 1.5μm-thick third polysilicon layer (P2) for (a) Design 1 and Design 2, and (b) Design 3 and Design 4. The wafer is then annealed for an hour at 1050°C.

Finally, the last deposition layer in this fabrication technique is the deposition of a 0.5 μm metal layer. This metal layer is for probing, bonding, providing electrical connectivity and acting as a reflective surface for the micromirror. The wafer is patterned lithographically with the METAL mask. The metal is deposited and patterned using the lift-off process. The deposition of the metal layer is illustrated in Figure 5.13.

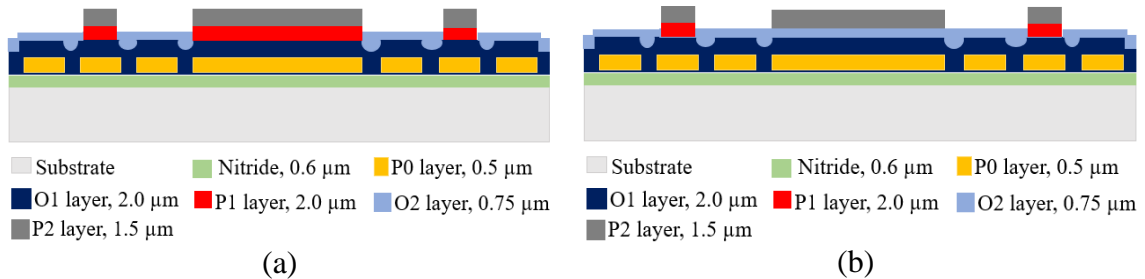


Figure 5.12: Etching away the P2 layer after patterning the POLY2 in the plasma etch system for (a) Design 1 and Design 2, and (b) Design 3 and Design 4.

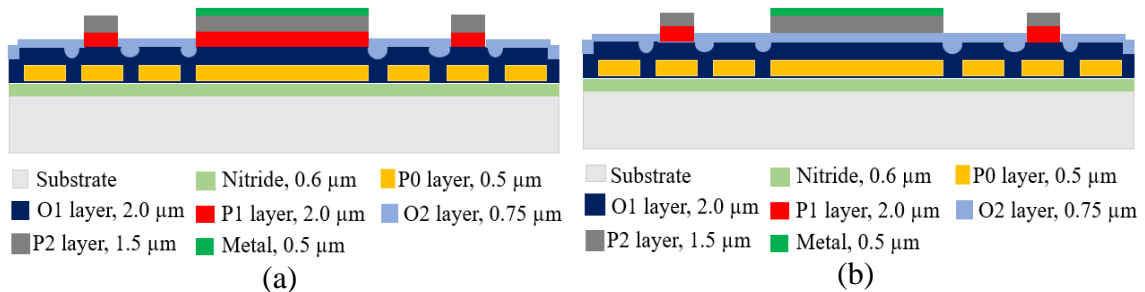


Figure 5.13: Deposition of the 0.5μm-thick metal layer for (a) Design 1 and Design 2, and (b) Design 3 and Design 4. First, the wafer is coated with METAL on the lithographically patterned wafer. The extra gold layer is then removed by the lift-off process in an Acetone bath.

The final released structure is shown in Figure 5.14. The chip is dipped in a 49% HF solution at room temperature for 1.5-2 minutes, which releases the structure. To avoid stiction, the chip is then immersed in DI water and alcohol for several minutes, placed in an oven at 110°C for at least 10 minutes, dried in CO₂.

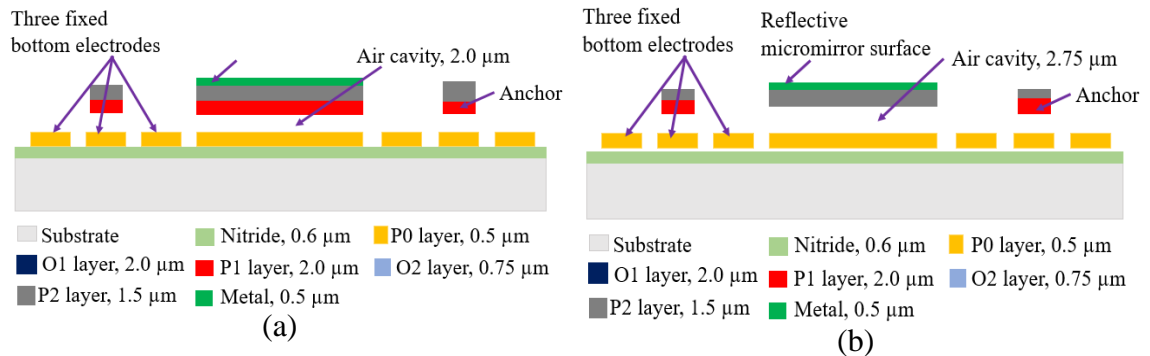


Figure 5.14: The chip dipped in a 49% HF solution, which releases the structure, followed by CO₂ drying to avoid stiction. Image illustrating released layer and structure of polysilicon layer for (a) Design 1 and Design 2, and (b) Design 3 and Design 4.

As discussed earlier, the air cavity in Design 1 and Design 2 is 2.0μm. In both Design 1 and Design 2, the anchors and L-shaped arms are made of the P1 layer. However, in Design 2, the bottom electrode beneath the micromirror surface is subdivided into four individual electrodes. Figures 5.15 and 5.16 illustrate the oblique view of Design 1 and Design 2 respectively. These are designed in MEMSPro using a standard PolyMUMPs fabrication layer sequence.

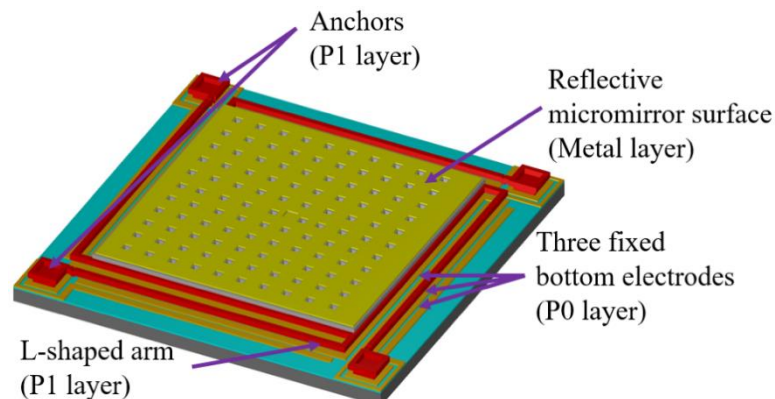


Figure 5.15: Design 1 micromirror designed in MEMSPro and developed using a standard PolyMUMPs fabrication sequence. In Design 1, the L-shaped arm is made of the P1 layer and the air cavity is 2.0μm.

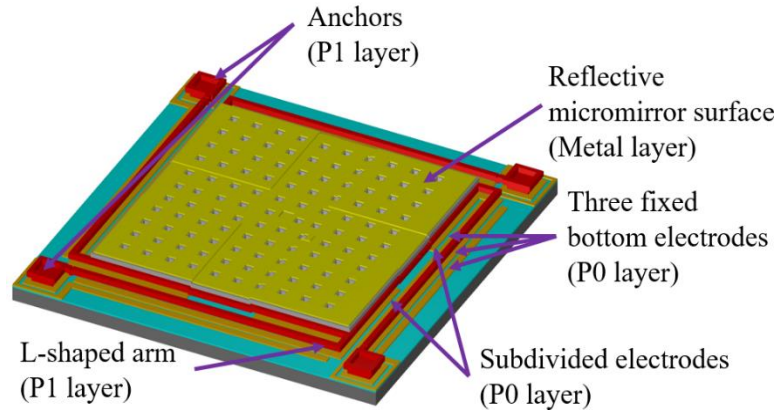


Figure 5.16: Design 2 micromirror designed in MEMSPro and fabricated using a standard PolyMUMPs fabrication sequence. In Design 2, the bottom electrode beneath the micromirror surface is subdivided into four individual electrodes. The L-shaped arm is made of the P1 layer and the air cavity is $2.0\mu\text{m}$.

In Design 3 and Design 4, the air cavity is $2.75\mu\text{m}$. This is achieved by combining two oxide layers, O1 and O2. Unlike Design 1 and Design 2, the L-shaped arms are made of the P2 layer. The thickness of the P2 layer is less than the P1 layer, as a result, the arm in Design 3 and Design 4 are thinner than Design 1 and 2. The anchors are made of both the P1 and P2 layer. Furthermore, in Design 4, the bottom electrode beneath the micromirror surface is subdivided into four individual electrodes. Figures 5.17 and 5.18 illustrate the oblique views of Design 3 and Design 4, respectively. These are designed in MEMSPro using a standard PolyMUMPs fabrication layer sequence.

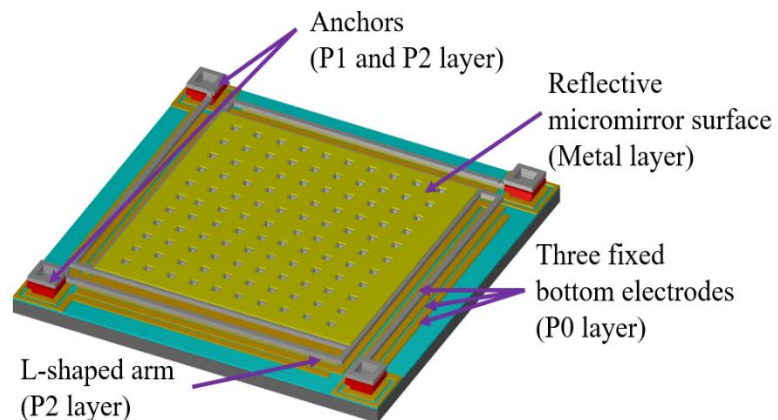


Figure 5.17: Design 3 micromirror designed in MEMSPro and fabricated using a standard PolyMUMPs fabrication sequence. In Design 3, the L-shaped arm is made of the P2 layer and the air cavity is $2.75\mu\text{m}$.

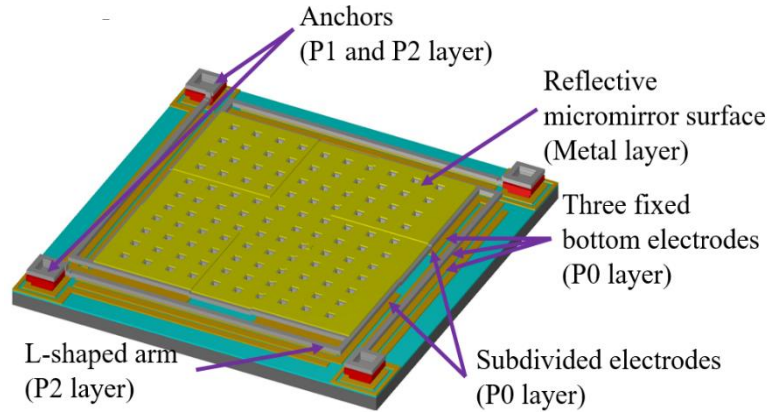


Figure 5.18: Design 4 micromirror designed in MEMSPro and developed using a standard PolyMUMPs fabrication sequence. In Design 4, the bottom electrode beneath the micromirror surface is subdivided into four individual electrodes. The L-shaped arm is made of the P1 layer and the air cavity is $2.75\mu\text{m}$.

5.4 Summary and Conclusion

In this chapter, the four proposed micromirror designs are developed using the PolyMUMPs fabrication technique. The fabrication steps of the proposed and developed micromirrors are discussed in detail. The micromirrors are fabricated using the PolyMUMPs technique for a proof-of-concept. In this research, the PolyMUMPs fabrication technique is chosen to fabricate the micromirror because it is a commercial program that provides a cost-effective proof-of-concept to fabricate MEMS devices. Without any modification in the fabrication process, the maximum air cavity that can be achieved between the plates is $2\mu\text{m}$. However, in this thesis, an air cavity of $2.75\mu\text{m}$ is achieved through employing a combination of the two available sacrificial layers, O1 and O2. As discussed earlier, this increase in the air cavity height will allow more space for the micromirror surface to deflect, consequently increasing the stroke of the micromirror. The fabrication steps to fabricate all four proposed designs are illustrated in Figures 5.1 to 5.14. The fabricated mirrors are then inspected on the Scanning Electron Microscope (SEM) and optical microscope. Figure 5.19 shows the Scanning Electron Microscope (SEM) image of a Design 1 micromirror that is captured using a HITACHI TM3030 plus tabletop

microscope. Figure 5.20 shows the Optical microscope image of a Design 3 micromirror that is captured using a SEMIPROBE SZMCTV1/2 microscope.

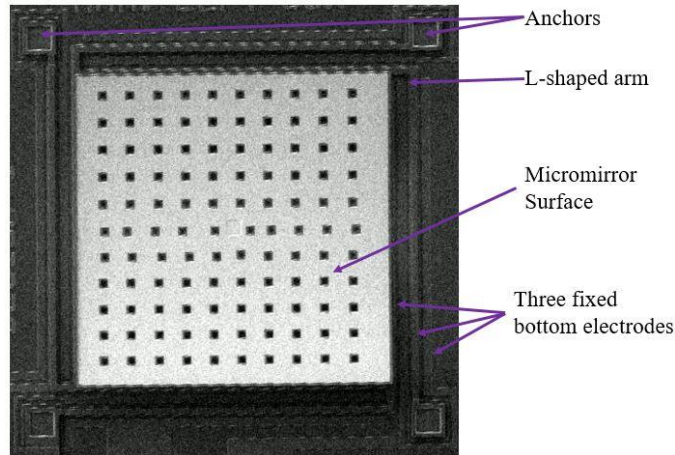


Figure 5.19: Scanning Electron Microscope (SEM) image of a Design 1 micromirror that is captured using a HITACHI TM3030 plus tabletop microscope.

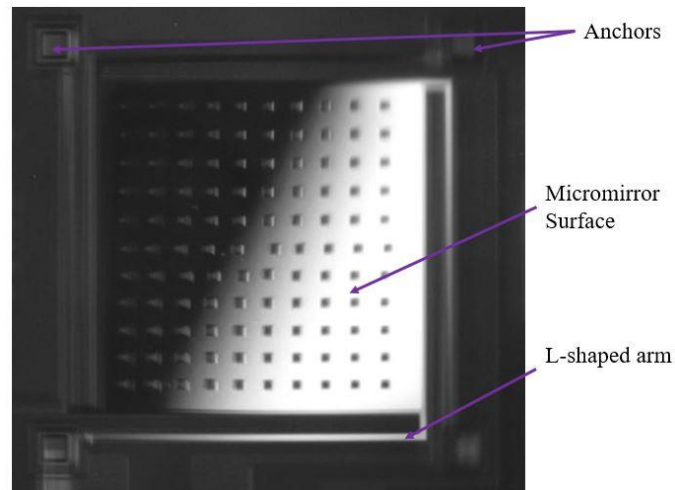


Figure 5.20: Optical microscope image of a Design 3 micromirror that is captured using the SEMIPROBE SZMCTV1/2 microscope.

Upon inspecting the fabricated micromirrors under the microscope, it is observed that they are curved, which can be seen in Figure 5.20. This bending or curving of the micromirror surface may be due to several reasons such as the size of the micromirror, stress-induced at the arm, or improper release of the layer during the fabrication process. During the fabrication process, there are several factors such as deposition rate, deposition process, the temperature, and the overlapping of different layers will induce stress on the

micromirror. Therefore, as part of future work, electrical and optical measurements can be carried out to identify the reasons for the observed bending of the micromirror and to address it. Potential future work is discussed in Chapter 6.

6 CHAPTER VI: CONCLUSION AND FUTURE WORK

6.1 Summary and Conclusion

In this thesis and in an effort to enhance the performance of micromirrors, four MEMS micromirror designs are proposed and developed that have enhanced stroke levels. In order to propose the micromirror designs, conventional and advanced micromirrors and their principle of operations, as well as their actuation mechanisms, are investigated and analyzed. Micromirrors can be actuated using several actuation mechanisms such as electrostatic, electromagnetic, and piezoelectric actuation. However, electrostatic actuation is chosen for the proposed micromirrors because of its advantages such as low power consumption, fast response time, high optical scan angle, simple design structure, and ease of fabrication. Therefore, the proposed micromirrors in this work are electrostatically-actuated parallel-plate micromirrors. However, one of the major disadvantages of electrostatic actuation is that the micromirror undergoes pull-in instability. Pull-in instability is a phenomenon that affects the stroke of the micromirror. Due to the pull-in instability effect, the micromirror becomes unstable when the micromirror surface reaches $1/3^{\text{rd}}$ of its air cavity gap. When the micromirror surface reaches $1/3^{\text{rd}}$ of the air cavity gap, the electrostatic force that is responsible for the movement of the micromirror surface is more than the mechanical restoring force, consequently making the micromirror unstable. However, in order to reduce the effect of pull-in instability, the proposed micromirror employs a unique configuration of the bottom electrodes. Instead of the conventional single bottom electrode, the proposed micromirror employs three bottom electrodes that push the micromirror upward, rather than traditional downward deflection. As discussed in Chapters 2 and 3, in this three-bottom-electrode configuration, the net electrostatic force that is

responsible for the movement of the micromirror surface is upward, as a result, the micromirror surface is moved upward. When one end of the micromirror surface moves upward, the other end moves downward. However, the amplitude of deflection is not equal on both ends. This downward deflection of the micromirror limits the stroke as it again makes the micromirror unstable when it reaches $1/3^{\text{rd}}$ of the air cavity gap. Since the upward movement of the micromirror surface is higher than the downward deflection of the surface, the effect of pull-in instability is reduced in the proposed micromirror designs.

There are several critical design parameters of the micromirror, including the width of the arm, input voltage, separation gap between the fixed bottom electrodes, and the air cavity, that affect the stroke of the micromirror. The MEMS Module in COMSOL Multiphysics software is used to investigate and analyze these critical design parameters. Simulation results identify the physical properties of the critical design parameters that will increase the stroke of the micromirror. In this thesis, four different micromirror design configurations are proposed and developed by varying the critical design parameters and the air cavity. These designs are named Design 1, Design 2, Design 3, and Design 4. The physical properties of these Designs are explained in Chapter 4. For all four proposed micromirror designs, the width of the L-shaped arm, the separation gap between the bottom electrodes, and the reflection micromirror surface are kept constant. The width of the L-shaped arm is $8\mu\text{m}$ and the separation gap between the fixed bottom electrodes is $8\mu\text{m}$. The L-shaped arm is chosen as it provides more flexibility to move the micromirror surface upward. The configuration of the bottom electrode that is beneath the micromirror and the air cavity is varied amongst the designs. PolyMUMPs fabrication technology is used to fabricate the proposed micromirrors. The maximum air cavity, without any modifications

in the fabrication step that can be achieved in the PolyMUMPs fabrication technique, is $2.0\mu\text{m}$. However, in this thesis, for Design 3 and Design 4, the air cavity is $2.75\mu\text{m}$. This is achieved by an unconventional approach, by combining two oxide layers. This increased air cavity will allow more space for the micromirror surface to move, consequently, increasing the stroke of the micromirror. However, one of the major disadvantages of the increased air cavity is that it increases the operating voltage. Details about the fabrication steps to fabricate all four proposed micromirror designs are presented in Chapter 5. COMSOL Multiphysics software, under the MEMS module, Solid mechanics and electrostatics studies are used in this work to simulate and investigate the performance of the proposed micromirrors.

In Design 1, the air cavity between the top and bottom electrodes is $2\mu\text{m}$. The stroke of the Design 1 of the micromirror at 100V is $2.25\mu\text{m}$ and the maximum downward deflection is $0.51\mu\text{m}$. In Design 2, the bottom electrode plate, which is beneath the reflective micromirror surface, is subdivided into four individual electrodes. This configuration of the bottom electrode allows the movement of different corners and sides of the micromirror to be controlled by selectively actuating subdivided electrodes. Since the bottom electrode is subdivided into individual electrodes, Design 2 is actuated in two ways. First, input DC bias voltage is applied to the arms and to one subdivided electrode. Second, input DC bias voltage is applied to the arms and two subdivided electrodes. For Design 2, an out-of-plane stroke of $2.03\mu\text{m}$ and maximum downward deflection of $0.58\mu\text{m}$ are achieved when an input DC bias voltage of 120V is applied to one subdivided electrode whereas an out-of-plane stroke of $1.69\mu\text{m}$ and a maximum downward deflection of $0.67\mu\text{m}$ are achieved when input DC bias voltage of 120V is applied to two subdivided electrodes.

In Design 3 and Design 4, the air cavity is $2.75\mu\text{m}$. For Design 3, the stroke and the maximum downward deflection of the micromirror at 150V are $4.37\mu\text{m}$ and $0.9\mu\text{m}$, respectively. Similar to Design 2, Design 4 is also actuated in 2 different ways. For Design 4, an out-of-plane stroke of $2.88\mu\text{m}$ and maximum downward deflection of $0.8\mu\text{m}$ are achieved when an input DC bias voltage of 150V is applied to one subdivided electrode whereas an out-of-plane stroke of $2.61\mu\text{m}$ and maximum downward deflection of $0.7\mu\text{m}$ are achieved when an input DC bias voltage of 150V is applied to two subdivided electrodes. The COMSOL simulations and analyses enable us to analyze the performance of the micromirror and determine its maximum operating voltage range. Moreover, the uniformity of the micromirror surface is also analyzed by evaluating the deflection along the diagonal cut-line on the micromirror surface. When the micromirror is actuated, one end of the micromirror surface moves upward whereas the other end moves downward, thereby tilting the micromirror surface. The uniformity is similar across the four proposed micromirror designs and the surface does not bend or buckle. From the simulation results presented in Section 4.3 and from the comparison shown in Table XII, it is observed that Design 3 yields the maximum stroke, which is $4.37\mu\text{m}$ at 150V. Furthermore, the total amount of deflection measured from one end to the other the micromirror surface for Design 3 is $5.07\mu\text{m}$, which is significantly higher than other proposed designs.

6.2 Future Work

For future work, and after fabrication of the micromirrors using a more robust and reliable fabrication technique, electrical measurements to check whether the fabricated layers are properly released needs to be carried out. After the electrical measurements, optical measurements to measure the optical scanning angle of the micromirror can be carried out.

Upon inspection of the fabricated micromirrors under an optical microscope and Scanning Electron Microscope (SEM), it is seen that the arms and the micromirror surface are curved. This may be for several reasons such as the improper release of the fabricated layer in the employed PolyMUMPs fabrication process, and/or the size of the micromirror surface. Further study and analysis need to be carried out to determine the possible reasons that cause the bending of the micromirror and then to rectify it. Furthermore, another reason causing the bending of the micromirror can be the width of the L-shaped arms, which are thinner than other layers due to the fabrication limitations in the chosen PolyMUMPs technique. As the arm is thin, it, in return, induces stress at the arm causing it to bend. Therefore, as future work, it is also important to analyze the stress at the arm and employ structural materials other than Poly Silicon. The PolyMUMPs fabrication process is chosen to fabricate all four proposed micromirror designs as a proof-of-concept. The PolyMUMPs fabrication process is also chosen because it is a very cost-effective process to fabricate a proof-of-concept device. Therefore, after doing all the measurements, another possible custom fabrication technique to fabricate the micromirror, which will enhance the performance of the micromirror, can be considered.

REFERENCES

- [1] World Health Organization, "Violence and Injury Prevention," 2018. [Online]. Available:
https://www.who.int/violence_injury_prevention/road_safety_status/2018/infographicEN.pdf?ua=1. [Accessed 30 05 2019].
- [2] Transport Canada's National Collision Database, "Canadian Motor Vehicle Traffic Collision Statistics: 2017," 2019.
- [3] Information and Communication Technology Council (ICTC), "Autonomous Vehicle and the future work in Canada," ICTC-CTIC, Canada, 2019.
- [4] F. Shuja, "The Roadmap for Autonomous (Self-Driving) Vehicles in Ontario, Canada," Ontario Good Roads Association, Ontario, Canada, 2015.
- [5] N. Kalra and S. M. Paddock, "Driving to safety: How many miles of driving would it take to demonstrate autonomous vehicle reliability?" *Transportation Research Part A: Policy and Practice*, vol. 94, pp. 182-193, 2016.
- [6] K. Kritayakirana and J. C. Gerdes, "Autonomous Vehicle Control at the Limits of Handling," *International Journal of Vehicle Autonomous Systems*, vol. 10, no. 4, p. 271, 2012.
- [7] S. Taranovich, "Autonomous automotive sensors: How processor algorithms get their inputs," EDN Network, 5 July 2016. [Online]. Available:
<https://www.edn.com/design/analog/4442319/Autonomous-automotive-sensors--How-processor-algorithms-get-their-inputs>. [Accessed 12 June 2018].
- [8] B. Smith, B. Hellman, d. Gin, l. Espinoza and Y. Takashima, "Single chip lidar with discrete beam steering by digital micromirror device," *Optics Express*, vol. 25, no. 13, pp. 14732-14745, 2017.

- [9] Y. Wang and M. C. Wu, "Micromirror based optical phased array for wide-angle beam steering," *International Conference on Micro Electro Mechanical Systems (MEMS)*, Las Vegas, NV, USA, 2017.
- [10] Y. Takashima, B. Hellman, J. Rodriguez, G. Chen, B. Smith, A. Gin, A. Espinoza, P. Winkler, C. Perl, C. Luo, E. Kang, Y. Kim, H. Choi and D. Kim, "MEMS-based Imaging LIDAR," *Light, Energy and the Environment 2018 (E2, FTS, HISE, SOLAR, SSL)*, 2018.
- [11] X. Han, Z.-f. Deng, Y.-l. Xue, Y.-q. Wang, L.-q. Cao, L. Han, B.-y. Zhou and M.-g. Li, "Laser 3D imaging technology based on digital micromirror device and the performance analysis," *Optoelectronic Imaging and Multimedia Technology III*, vol. 9273, no. 10, 2014.
- [12] Y. Wang and M. C. Wu, "Micromirror based optical phased array for wide-angle beam steering," *International Conference on Micro Electro Mechanical Systems (MEMS)*, Las Vegas, NV, USA, 2017.
- [13] B. Schwarz, "LIDAR Mapping the world in 3D," *Nature Photonics*, vol. 4, 2010.
- [14] H. Wang, B. Wang, B. Liu, X. Meng and G. Yanga, "Pedestrian recognition and tracking using 3D LiDAR for autonomous vehicle," *Robotics and Autonomous Systems*, vol. 88, pp. 71-78, 2017.
- [15] Q. Zhu, L. Chen, Q. Li, M. Li, A. Nüchter and J. Wang, "3D LIDAR point cloud based intersection recognition for autonomous driving," *IEEE Intelligent Vehicles Symposium*, Alcalá de Henares, Spain, 2012.
- [16] W. Zhang, "LIDAR-based road and road-edge detection," *IEEE Intelligent Vehicles Symposium*, San Diego, CA, USA, 2010.
- [17] E. Shearman, E. Hoare and A. Hutton, "Trials of automotive radar and lidar performance in road spray," *IEEE Colloquium on Automotive Radar and Navigation Techniques*, London, UK, 2002.

- [18] S. Wu, Z. Liu and B. Liu, "Enhancement of lidar backscatters signal-to-noise ratio using empirical mode decomposition method," *Optics Communications*, vol. 1, no. 1, pp. 137-144, 2006.
- [19] C. V. Poulton, A. Yaacobi, D. B. Cole, M. J. Byrd, M. Raval, D. Vermeulen and M. R. Watts, "Coherent solid-state LIDAR with silicon photonic optical phased arrays," *Optics Letters*, vol. 42, no. 20, pp. 4091-4094, 2017.
- [20] Y. Bai and J. T. W. Yeow, "Design, Fabrication, and Characteristics of a MEMS Micromirror with Sidewall Electrodes," *Journal of Microelectromechanical Systems*, vol. 19, no. 3, pp. 619-631, 2010.
- [21] MEMSCAP, "PolyMUMPs Design Handbook," 2011.
- [22] H. v. Heeren and P. Salomon, "MEMS Recent Developments, Future Directions," *Electronics Enabled Products Knowledge Transfer Network, Wolfson School of Mechanical and Manufacturing Engineering, Loughborough University, Loughborough*, 2007.
- [23] H. T. Imam, "Electrostatically actuated 2D MEMS micro-mirror," *Dalhousie University, Halifax, Nova Scotia*, 2009.
- [24] D. S. Eddy and D. R. Sparks, "Application of MEMS technology in automotive sensors and actuators," *Proceedings of the IEEE*, vol. 86, no. 8, pp. 1747-1755, 1998.
- [25] The American Society of Mechanical Engineers, "#243 Digital Micromirror Device," The American Society of Mechanical Engineers, [Online]. Available: <https://www.asme.org/about-asme/engineering-history/landmarks/243-digital-micromirror-device>. [Accessed 29 08 2019].
- [26] S.-W. Chung, J.-W. Shin, Y.-K. Kim and B.-S. Han, "Design and fabrication of micromirror supported by electroplated nickel posts," *Sensors and Actuators A: Physical*, vol. 54, no. 1-3, pp. 464-467, 1996.

- [27] H. K. Lakner, P. Duerr, U. Dauderstaedt, W. Doleschal and J. Amelung, "Design and fabrication of micromirror arrays for UV lithography," *MOEMS and Miniaturized Systems II*, San Francisco, CA, United States, 2001.
- [28] S. Nayar, V. Branzoi and T. Boult, "Programmable imaging using a digital micromirror array," *Proceedings of the 2004 IEEE Computer Society Conference on Computer Vision and Pattern Recognition, CVPR 2004.*, Washington, DC, USA, 2004.
- [29] T. Tsuchiya, "MEMS mirrors for automotive applications," *2017 IEEE International Meeting for Future of Electron Devices*, Kansai, 2017.
- [30] T.-R. Hsu, "Microactuation," *MEMS and microsystems*, 2008, p. 53.
- [31] S. Büttgenbach, "Electromagnetic Micromotors—Design, Fabrication and Applications," *Micromachines*, vol. 5, no. 4, pp. 929-942, 2014.
- [32] D. H. S. Maithripala, B. D. Kawade, J. M. Berg and W. P. Dayawansa, "A general modelling and control framework for electrostatically actuated mechanical systems," *International Journal of Robust and Nonlinear Control*, vol. 15, no. 16, pp. 839-857, 2005.
- [33] H. Camon and F. Larnaudie, "Fabrication, simulation and experiment of a rotating electrostatic silicon mirror with large angular deflection," *Proceedings IEEE Thirteenth Annual International Conference on Micro Electro Mechanical Systems (Cat. No.00CH36308)*, Miyazaki, Japan, Japan, 2000.
- [34] S. Beeby, G. Ensell, M. Kraft and N. White, "Actuation Technique: Electrostatic," *MEMS mechanical Sensors, Boston, Artech House, Inc.*, 2004, pp. 104-106.
- [35] E. Pengwang, K. Rabenorosoa, M. Rakotondrabe and N. Andreff, "Scanning Micromirror Platform Based on MEMS Technology for Medical Application," *Micromachines*, vol. 7, no. 2, p. 24, 2016.

- [36] H.Camon and C.Ganibal, "Advantages of alternative actuating signal for MEMS actuators," *Sensors and Actuators A: Physical*, vol. 136, no. 1, pp. 299-303, 2007.
- [37] F. Hu, J. Yao, C. Qiu and H. Ren, "A MEMS micromirror driven by electrostatic force," *Journal of Electrostatics*, vol. 68, pp. 237-242, 2010.
- [38] A. Micheal and C. Y. Kwok, "Monolithically integrated out-of-plane micro-mirror," *Sensors and Actuators A: Physical*, vol. 179, pp. 263-276, 2011.
- [39] M. N. Horenstein, S. Pappasa, A. Fishova and T. G. Bifano, "Electrostatic micromirrors for subaperturing in an adaptive optics system," *Journal of Electrostatics*, vol. 54, pp. 321-332, 2002.
- [40] H. Sadeghian, G. Rezazadeh and P. M. Osterberg, "Application of the Generalized Differential Quadrature Method to the Study of Pull-In Phenomena of MEMS Switches," *Journal of Microelectromechanical Systems*, Vols. 16, NO. 6, DECEMBER 2007, no. 6, pp. 1334-1340, 2007.
- [41] O. Degani, E. Socher, A. Lipson, T. Leitner, D. J. Setter, S. Kaldor and Y. Nemirovsky, "Pull-In Study of an Electrostatic Torsion Microactuator," *Journal of microelectronic systems*, vol. 7, no. 4, pp. 373-379, 1998.
- [42] J. Seeger and B. Boser, "Charge control of parallel-plate, electrostatic actuators and the tip-in instability," *Journal of Microelectromechanical Systems*, vol. 12, no. 5, pp. 656 - 671, 2003.
- [43] K. Das and R. C. Batra, "Pull-in and snap-through instabilities in transient deformations of microelectromechanical systems," *Journal of Micromechanics and Microengineering*, vol. 19, 2009.
- [44] M. Z and M.T.Ahmadian, "Application of homotopy analysis method in studying dynamic pull-in instability of microsystems," *Mechanics Research Communications*, vol. 36, no. 7, pp. 851-858, 2009.

- [45] S. He, R. B. Mrad and J. Chong, "Repulsive-force out-of-plane large stroke translation micro electrostatic actuator," *Journal of Micromechanics and Microengineering*, vol. 21, no. 7, 2011.
- [46] F. Hu, Y. Tang and Y. Qian, "Design of a MEMS micromirror actuated by electrostatic repulsive force," *Optik*, vol. 123, no. 5, pp. 387-390, March 2012.
- [47] M. A. Helmbrecht, T. Juneau, M. Hart and N. Doble, "Segmented MEMS deformable-mirror technology for space applications," *Proc. of SPIE*, vol. 6223, no. 622305, 2006.
- [48] F. Pardo, R. A. Cirelli, E. J. Ferry, W. Y.-C. Lai, F. P. Klemens, J. F. Miner, C. S. Pai, J. E. Bower, W. M. Mansfield, A. Kornblit, T. W. Sorsch, J. A. Taylor, M. R. Baker, R. Fullowan, M. E. Simon, V. A. Aksyuk, R. Ryf, H. Dyson and S. Arney, "Flexible fabrication of large pixel count piston-tip-tilt mirror arrays for fast spatial light modulators," *Microelectronic Engineering*, vol. 84, no. 5-8, pp. 1157-1161, 2007.
- [49] P. Patterson, D. Hah, H. Nguyen, H. Toshiyoshi, R.-m. Chao and M. Wu, "A scanning micromirror with angular comb drive actuation," *Technical Digest. MEMS 2002 IEEE International Conference*, 2002.
- [50] J. A. Yeh, C.-N. Chen and Y.-S. Lui, "Large rotation actuated by in-plane rotary comb-drives with serpentine spring suspension," *Journal of Micromechanics and Microengineering*, vol. 15, no. 1, 2005.
- [51] C.-H. Ji, Y. Yee, J. Choi, S.-H. Kim and J.-U. Bu, "Electromagnetic 2/spl times/2 MEMS optical switch," *IEEE Journal of Selected Topics in Quantum Electronics*, vol. 10, no. 3, pp. 545 - 550, 2004.
- [52] Hamamatsu, "MEMS mirrors," 2016. [Online]. Available: <https://www.hamamatsu.com/us/en/product/optical-components/mems-mirror/index.html>. [Accessed 06 11 2018].

- [53] J. S. J. Kumar, E. A. Tetteh and E. P. Braineard, "A study of why electrostatic actuation is preferred and a simulation of an electrostatically actuated cantilever beam for mems applications," *International Journal of Engineering Sciences & Emerging Technologies*, vol. 6, no. 5, pp. 441-446, 2014.
- [54] K. H. Kim, B. H. Park, G. N. Maguluri, T. W. Lee, F. J. Rogomentich, M. G. Bancu, B. E. Bouma, J. F. d. Boer and J. J. Bernstein, "Two-axis magnetically-driven MEMS scanning catheter for endoscopic high-speed optical coherence tomography," *Optics Express*, vol. 15, no. 26, pp. 18130-18140, 2007.
- [55] T. Iseki, M. Okumura and T. Sugawara, "Two-Dimensionally Deflecting Mirror Using Electromagnetic Actuation," *Optical Review*, vol. 13, no. 4, p. 189–194, 2006.
- [56] J. Smits and W. Choi, "The constituent equations of piezoelectric heterogeneous bimorphs," *IEEE Transactions on Ultrasonics, Ferroelectrics, and Frequency Control*, vol. 38, no. 3, pp. 256 - 270, 1991.
- [57] M. Fukunaga, M. Takesada and A. Onodera, "Ferroelectricity in Layered Perovskites as a Model of Ultra-Thin Films," *World Journal of Condensed Matter Physics*, vol. 06, no. 03, 2012.
- [58] L. Lin and E. Keeler, "Progress of MEMS Scanning Micromirrors for Optical Bio-Imaging," *Micromachines*, vol. 6, no. 11, pp. 1675–1689, May 2015.
- [59] S. Beeby, A. Blackburn and N. White, "Processing of PZT piezoelectric thick-films on silicon for microelectromechanical systems," *Journal of Micromechanics and Microengineering*, vol. 9, no. 3, pp. 218-29, 1999.
- [60] J. G. Korvink and O. Paul, "7 Free-Space Optical MEMS," *MEMS: A Practical Guide to Design, Analysis, and Applications*, 2006, pp. 345-402.

- [61] R.C.Batra, M.Porfiri and D.Spinelloa, "Vibrations of narrow microbeams performed by an electric field," *Journal of Sound and Vibration*, vol. 309, no. 3-5, pp. 600-612, 2008.
- [62] V. Leus and D. Elata, "Fringing Field Effect in Electrostatic Actuators," *TECHNION-Israel Institute of Technology*, Faculty of Mechanical Engineering, 2004.
- [63] MEMSCAP, "MEMS Manufacturing Services," MEMSCAP, [Online]. Available: <http://www.memscap.com>. [Accessed 29 October 2019].
- [64] A. Cowen, B. Hardy, R. Mahadevan and S. Wilcenski, "PolyMUMPs Design Handbook," MEMSCAP Inc., 2011.

APPENDIX A

PERMISSION TO USE SPIE PUBLICATION



Katie Sinclair katies@spie.org via spieorg.on... Thu, Nov 7, 7:56 PM (4 days ago)
to me ▾



Dear Mr. Aryal,

Thank you for seeking permission from SPIE to reprint material from our publications. SPIE shares the copyright with you, so as author you retain the right to reproduce your paper in part or in whole.

Publisher's permission is hereby granted under the following conditions:

(1) the material to be used has appeared in our publication without credit or acknowledgment to another source; and

(2) you credit the original SPIE publication. Include the authors' names, title of paper, volume title, SPIE volume number, and year of publication in your credit statement.

Please let me know if I may be of any further assistance.

Best,
Katie Sinclair
Editorial Assistant, Publications
SPIE
+1 360 685 5436
katies@spie.org

SPIE is the international society for optics and photonics
<http://SPIE.org>

SPIE.



VITA AUCTORIS

Niwit Aryal was born in 1992 in Rajbiraj, Nepal. He graduated from his high school, Happy Land Higher Secondary School, Rajbiraj, Nepal. From there, he went on to Anna University, Chennai, India, where he obtained his Bachelor of Engineering in Electronics and Communication Engineering in 2015. He has 3 years of professional experience in the field of IT and Computer Science. He is currently a candidate for the Master's degree in Electrical and Computer Engineering at the University of Windsor and hopes to graduate in Fall 2019.